THE PREDICTION OF FLUX DECLINE IN CROSS-FLOW MICROFILTERS VIA THREE-DIMENSIONAL FLUID DYNAMIC MODELS OF TORTUOUS PORE STRUCTURE

BY

BINGYI YU

THESIS

Submitted in partial fulfillment of the requirements
for the degree of Master of Science in Mechanical Engineering
in the Graduate College of the
University of Illinois at Urbana-Champaign, 2011

Urbana, Illinois

Advisers:

Professor Shiv G. Kapoor
Professor Richard E. DeVor

Abstract

Cross-flow microfiltration is a viable method to increase the in-use lifetime of semi-synthetic metalworking fluids. However in operation, fouling of the microfilter has been shown to occur and bring about a reduction of microfilter flux. This research develops a fluid dynamic model of the tortuous pore geometry to simulate the progression of fouling and investigate the associated effect on flux decline.

A three-dimensional tortuous pore geometry was created to study the development of fouling mechanisms via a fluid dynamic model. The geometry was obtained by reconstructing a three-dimensional geometry from images of two-dimensional cross-sectional slices of a α-alumina microfilter obtained from a focused ion beam. A wall collision model and a particle trapping model were developed for the investigation of fouling mechanisms in three dimensions. Hydrodynamic, particle-particle electrostatic, and Brownian forces as well as the wall collision model and particle trapping model were used in the reconstructed geometry via computational fluid dynamics to simulate metalworking colloidal particles traveling through and becoming trapped in the tortuous pore paths of a microfilter. Results revealed sharp flux decline initiating from partial pore blocking and subdued flux decline transitioning to cake layer development with steady-state flow. This flux behavior was consistent with experimental flux data.

The fluid dynamic model was enhanced with particle-membrane electrostatic forces. The addition of such forces via Surface Element Integration was shown to affect particle trajectories in a tortuous three-dimensional microfilter membrane geometry. The model was validated by comparing experimental flux decline data with simulation flux decline data. A design of experiments was conducted to investigate the effects of transmembrane pressure, particle-membrane (PM) zeta potential, and particle-particle (PP) zeta potential on flux decline. The simulation experiments revealed that low flux decline was associated with relatively low transmembrane pressures and near-zero values of PP- and PM-zeta potential; and relatively high transmembrane pressures and more-negative values of PP- and PM-zeta potential. The amount of flux decline was shown to be correlated to the specific nature of partial and complete pore blocking in the pore structure.

To Dad, Mom, and Kelly

Acknowledgements

Thank you, Professor Kapoor and Professor DeVor, for your tough-love guidance and financial support. You are researchers, teachers, and leaders that I admire and respect. I have also learned much of successful technical writing that can be put simply: keep content logical, flowing, concise, and clear.

Thank you, Professor Johnson Samuel, for the encouragement in my graduate studies, my personal and professional relationships, and my life walk.

Thank you, tenants of 4426 MEL: Alex, Hari, Jimmy, Keith, Soham, Lingyun, and Runtao; for the conversations, advice, and friendship. You gave our office life!

Thank you, Xin Dong, as your constant support, kindness, and faith has encouraged me so greatly.

Table of Contents

Chapter 1

Introduction

1.1 Background and Motivation

Although microfiltration is used in industry with synthetic metalworking fluids (MWF), the knowledge of its viability and compatibility with semi-synthetic MWFs in cross-flow filtration is only beginning to emerge [1, 2]. Prior works have shown membrane fouling from semi-synthetic emulsions [3-8], thereby decreasing MWF flow rate and reducing the technological usefulness. To promote viability of microfilters with semi-synthetic MWFs in industry, the mechanisms giving rise to fouling and its associated flux decline must be better understood.

Skerlos et al. found substantial flux decline during the microfiltration of synthetic MWFs [6, 7]. His experimental cross-flow microfiltration testbed controlled transmembrane pressure and MWF flow rate and captured microfilter flux data. Different chemical compositions of the MWFs tested in the microfiltration testbed showed that the concentrations of additives affected microfiltration flux. The effects of these additives were found to be attributed to adsorption leading to pore constriction, pore blocking and cake layer development. Various authors [1, 9, 10] verified the Skerlos et al. [6] experimental results by designing MWFs that

incorporated formulation changes, tested in machining operations, and found reduced flux decline and similar performance versus commercial MWFs.

Semi-synthetic MWFs were first tested with microfilters by Rajagopalan et al. in his work in passing bacteria- and hydraulic oil-laden MWF through microfilters [2]. The oil was able to be separated from the MWF, and the concentration of bacteria decreased substantially after microfiltration. This showed success in the combination of the two technologies. Nonetheless, the authors found minor losses in MWF ingredients as the filtered MWF was reused, suggesting that such ingredients were being lost in the membrane. Wentz et al. experimentally investigated the losses that occurred in the membrane [4]. He utilized a cross-flow microfilter test fixture with controllable operating conditions and resulting flux measured to document the declining flux. His results showed that although the time to steady-state flux decline changed depending on the concentration of the MWF, the value of the steady-state did not change. He also attributed the flux decline to the fouling mechanisms adsorption leading to pore constriction, pore blocking, and cake layer development via SEM images. However, their empirical methods of predicting flux decline were not generalized.

Flux decline was predicted by Song [11] via mechanistic models of each fouling mechanism: partial and complete pore blocking, cake layer development, and concentration polarization. Fouling and the associated effect on flux decline were functions of the number of pores available to be blocked and the resistance of the pore membrane. He unified the flux decline models from each fouling mechanism to predict the total flux decline in cross-flow microfilters under different cross-flow microfiltration operating conditions. Zhao et al. [12] expanded the Song model by including the adsorption fouling mechanism via flux observations and SEM images. Their model was experimentally validated by predicting flux

decline in various operating transmembrane pressures and pore sizes. The fouling mechanisms predicted to be occurring during flux decline were also confirmed in SEM images of the fouled microfilter. However, the process by which fouling progressed and affected flux decline was not apparent in these two works.

Wentz et al. [13] studied the progression of fouling and correlated fouling to membrane flux decline. He created a verisimilar two-dimensional tortuous geometry fluid dynamic model, equipped with colloidal hydrodynamic forces, to examine the process by which a pore becomes blocked and flux is reduced. Through injection of particles with sizes from a time-varying distribution, the partial pore blocking fouling mechanism was discovered through pores becoming obstructed, but not completely sealing the system flux, a behavior verifying that which was predicted in mechanistic models by Song [11]. This trapping behavior and its associated flux decline were also affected by transmembrane pressure. However, all pores in two-dimensional simulations eventually became blocked and flux approached zero, a behavior which differed from actual microfilters, where not all pores will become completely blocked and flux does not trend to zero [4]. Kim et al. [8, 14] applied electrostatic and Brownian forces to particle movement in fluid dynamic models. Particles, under the effects of hydrodynamic, electrostatic, and Brownian forces, were introduced into an ideal pore geometry. Particles were judged to affect fouling and flux decline according to their disposition trapped at, or traveled through, a pore. In testing different combinations of each of the applied forces, results showed that hydrodynamic, electrostatic, and Brownian forces all have a significant impact on particle movement and its resulting disposition. However, their investigation on particle movement did not cover the means by which fouling progressed inside the microfilter membrane or in tortuous pore geometries.

Ham et al. [3, 15] expanded on the work of Kim et al. [8, 14] and Wentz et al. [13] by incorporating electrostatic forces and Brownian motion in two-dimensions [3] and three-dimensions [15]. Two-dimensional simulations with enhanced particle force models in a tortuous pore geometry revealed different manners by which the pore became blocked depending on whether only hydrodynamic forces were applied or hydrodynamic forces, electorstatic forces, and Brownian forces were applied. The simulations also showed how particles stacked upon one another internal to a pore, a behavior that ultimately shut off flux in a pore. Most importantly, it was recognized that each of the colloidal forces contributed greatly to particle trajectories. Three-dimensional simulations examined fouling and flux decline via two different pore geometries. An intersection of six pore passageways was developed to show how particles accumulate when they trap. Results showed that spherical particles introduced into the geometry were not able to completely block all pore passageways, but instead blocked in a manner that reduced flux substantially. Another geometry, composed of stacked disks with holes cut to imitate pore entrances, was created to discover how partial pore blocking developed at more than one pore intersections. Results of the simulation found complex flux decline behaviors in particles that trapped but did not affect flux decline. The three-dimensional simulations showed frequent occurrences of the partial pore blocking fouling mechanism and found non-zero flux decline to occur at steady-state, a behavior that was different versus two-dimensional simulations yet consistent with experimental flux data.

Understanding fouling and the associated flux decline has shown substantial progress in recent works, however, some gaps in knowledge remain to be filled. Simulated MWF colloids travel in idealized pore geometries and could only be trapped in single passageway

intersections or in specific locations purposely modeled to become blocked. Moreover, previous works [3, 8, 13] simulated particle movement with a point mass approximation, generating trajectories with unlikely particle movement. These two limitations are atypical of actual microfilter geometry and therefore do not give the best approximation to the progression of fouling and the associated flux decline. Particle-membrane electrostatic forces were not included in previous works due to the assumption that the point of zero charge precluded such forces from implementation. However, the assumption does not apply in general, and the absence of particle-membrane electrostatic forces in fact has a profound effect on fouling and flux decline. Lastly, trends can currently be predicted, but the lack of experimental validation makes prediction of flux decline in actual experiments difficult.

1.2 Research Objective, Scope, and Tasks

1.2.1 Research Objective and Scope

The objective of this research is to predict the flux decline of semi-synthetic MWFs in cross-flow microfiltration via a three-dimensional fluid dynamic model of the tortuous pore geometry.

To best predict flux decline in cross-flow microfiltration systems due to semi-synthetic MWFs, this research will focus on uncontaminated semi-synthetic MWFs to determine solely the effects of colloidal ingredients on microfilter fouling. α-alumina microfilters with 0.5 μm average pore diameters will be utilized in this work because of the non-reactivity of α-

alumina to MWF ingredients, and because of the relatively large pore size that allows smaller colloidal ingredients through.

The progression of fouling and the associated flux decline is difficult to model via conventional analytical means, therefore a three-dimensional fluid dynamic model will be utilized for analysis. The microfilter geometry in the model should be accurate to that in actuality, therefore a tortuous pore geometry will be utilized for simulation. MWF colloid sizes range from 10 nm to 500 nm, but only particles with sizes greater than 100 nm typically cause partial and complete pore blocking in microfilter membranes; here, only partial and complete pore blocking will be analyzed. Colloids are primarily affected by three interactions in actual microfilters, hence, the mimicked hydrodynamic, electrostatic, and Brownian forces will be implemented in the fluid dynamic model. Experimental validation will require duplication of operating conditions in the simulations and therefore will be completed via a cross-flow microfiltration testbed developed by Professor John E. Wentz at the University of St. Thomas in St. Paul, Minnesota.

1.2.2 Research Tasks

This research consists of these tasks:

Simulate fouling via a three-dimensional tortuous pore fluid dynamic model by:

- Obtaining cross-sectional images of the microfilter with the focused ion beam;
- Recreating a verisimilar three-dimensional tortuous pore geometry via image analysis and solid modeling;

- Adding hydrodynamic, electrostatic, and Brownian forces and particle dispositions schemes to the geometry in the fluid dynamic model;
- Analyzing the progression of fouling and its effect on flux decline via the fluid dynamic model;

Employ the created three-dimensional tortuous pore fluid dynamic model to investigate the variables governing fouling on flux decline by:

- Enhancing the fluid dynamic model with particle-membrane electrostatic forces;
- Experimentally validating the enhanced fluid dynamic model with the experimental cross-flow microfiltration testbed;
- Changing the variables governing the fouling phenomena: transmembrane pressure, particle-particle zeta potential, and particle-membrane zeta potential;
- Evaluating the effect of such variables on flux decline via a design of experiments;
- Interpreting the flux decline responses as a function of microfilter fouling.

1.3 Overview of Thesis

Chapter 2 reviews existing literature regarding MWFs and microfiltration fouling. It reviews evidence of fouling and experimental observations of flux decline. Mechanistic models and trends that are developed for the investigation and prediction of flux decline are then reviewed. The need to study the mechanisms by which fouling and flux decline occurs leads to the review of fluid dynamic models. A background of the physical and chemical forces acting upon foulants is first covered. Hydrodynamic force models that describe the drag

forces impacting colloids are visited. Next, electrostatic force models are covered to detail the electrostatic double-layer interactions between particles and particles (PP), and a particle and the membrane (PM). Molecular stochastic interactions called Brownian forces are discussed next. The implementation of these forces and the associated fouling and flux decline trends is captured by a review of literature regarding various fluid dynamic models.

Chapter 3 covers the creation of a verisimilar tortuous three-dimensional pore membrane from FIB images. This establishes the framework of three-dimensional fluid dynamic model. It details the geometry recreation process and the implementation of the hydrodynamic, PP-electrostatic, and Brownian forces. The particle collision model and particle trapping model are developed and implemented. This Chapter then runs simulations of MWFs of different in-use lifetimes and compares the observed fouling mechanisms and flux decline to trends seen from experiments. This completes the first part of the objective.

Chapter 4 examines the enhancement of the verisimilar tortuous three-dimensional model with a finite element electrostatic force model for determining PM-electrostatic forces. Experimental validation of the enhanced fluid dynamic model is discussed. This Chapter then details a design of experiments employed to investigate the effects of variables governing fouling phenomena on flux decline. The results of the design of experiments are presented and interpreted to reveal how such variables affect flux decline via mechanisms of fouling. This completes the second part of the objective.

Chapter 5 summarizes the accomplishments of Chapters 3 and 4, offers research improvements, and establishes the framework for future work.

Chapter 2

Literature Review

This chapter examines the available literature regarding fouling and flux decline during the microfiltration of metalworking fluids (MWF). There are four sections in this chapter. Section 2.1 first introduces metalworking fluids and microfiltration, and reviews the literature regarding the observed fouling and resultant flux decline that arises the two co-operate. Section 2.2 reviews the research to date on solutions to the fouling and flux decline in the form of experimental flux decline models. Section 2.3 reviews the literature to date on flux decline prediction via fluid dynamic modeling. Section 2.4 summarizes this literature review and examines the gaps in knowledge of this research.

2.1 Metalworking Fluid Microfiltration

Microfilters and metalworking fluids are detailed in Section 2.1.1. The fouling phenomena arising from the combined usage of these two technologies are discussed in Section 2.1.2. Section 2.1.3 discusses the consequences and observations of the phenomena in experiments.

2.1.1 Microfiltration and Metalworking Fluids

Microfiltration is a separation technology that utilizes a pressure differential across a porous media to remove contaminants from a dirty stream [5]. Microfiltration differs from alternatives like reverse osmosis, nanofiltration, ultrafiltration its particle size elimination capability. The scales of particle removal for these filtration technologies are 0.1 nm and larger, 1 nm and larger, 3 nm and larger, and 50 nm and larger, respectively [16]. Reverse osmosis and nanofiltration are typically used for the removal of minute organic substances for water purification [17]. Ultrafiltration is typically used for the removal of larger substances such as colloids or particulates in food process substances [16]. With the benefit of larger particle size removal capability, microfilters are used in various applications such as wastewater treatment [18, 19], sterile water production [20], and machining fluid recycling [21-23].

Microfilters operate via dead-end filtration or cross-flow filtration [16]. Dead-end filtration has one inlet and one outlet. Bulk fluid, or the *feed*, contaminated with tramp oils, bacteria, and waste metal via machining processes, is filtered by entering the inlet of the dead-end filter. A pressure differential separates the fluid, leaving contaminants on the surface and allowing cleansed liquid, called the *permeate*, through the porous structure of the filter. The permeate leaves the microfiltration structure and is reused in the machining process. Dead-end filtration is seen in Fig. 2.1.

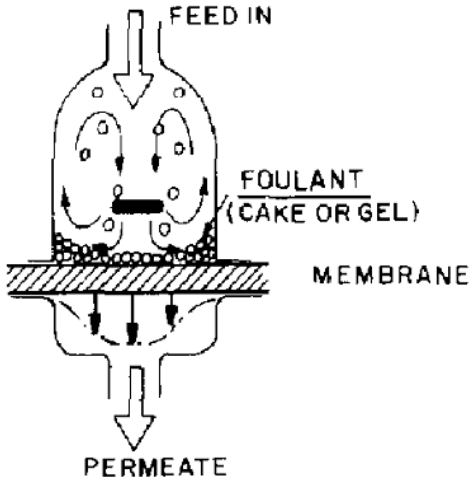

Figure 2.1 - Schematic of a Dead-end Microfilter [5]

Cross-flow filtration has one inlet and two outlets. The feed passes across the membrane, leaving contaminants on the surface of the microfilter. The permeate that passes through the microfilter is returned to be reused. The remaining feed, unfiltered contaminants, and debris on the microfilter surface are carried along out of the microfilter and deposited into a sump. This is called the *retentate*. Cross-flow filtration is seen in Fig. 2.2.

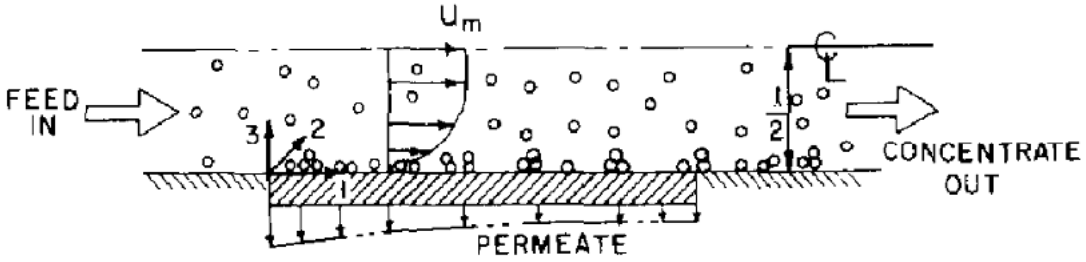

Figure 2.2 - Schematic of a Cross-flow Microfilter [5]

In the machining industry, ongoing machining processes require continuous availability of lubricant and scrap carrier and therefore prohibit stoppage of processes for maintenance and cleaning. The continuous recycling needs of these processes are quickly sighting crossflow microfiltration as accepted technology for the needs of metalworking fluids.

Metalworking fluids (MWF) are a mixture of oils and chemicals applied onto machining operations to cool, lubricate, and remove chips [24]. There are three different compositions of MWFs: soluble oil, semi-synthetics, and synthetics; which differ in chemical compositions, base fluid, and additives [25]. Soluble oil and synthetic MWFs have water-soluble ingredients that are distinctly differentiated from the colloidal or particulate contaminants, hence, these MWFs typically have worked well with microfiltration in various applications [1, 2, 9]. Semi-synthetic MWFs, on the other hand, have a complex ingredient composition that sometimes is not soluble and therefore still have had problems with microfiltration. However, the pace of semi-synthetic MWF research has been increasing due to both the control of 40% of the MWF market [26], developed over last two decades, and the upward trend of their control [2, 26, 27].

2.1.2 Fouling during Microfiltration of Metalworking Fluids

The passage of the metalworking fluid leaves ingredients on the surface of and within the microfilter membrane. This fouling of the membrane occurs through four distinct mechanisms: surface adsorption, partial pore blocking, pore blocking, cake layer development, and concentration polarization. Fig. 2.3 depicts each of the fouling mechanisms.

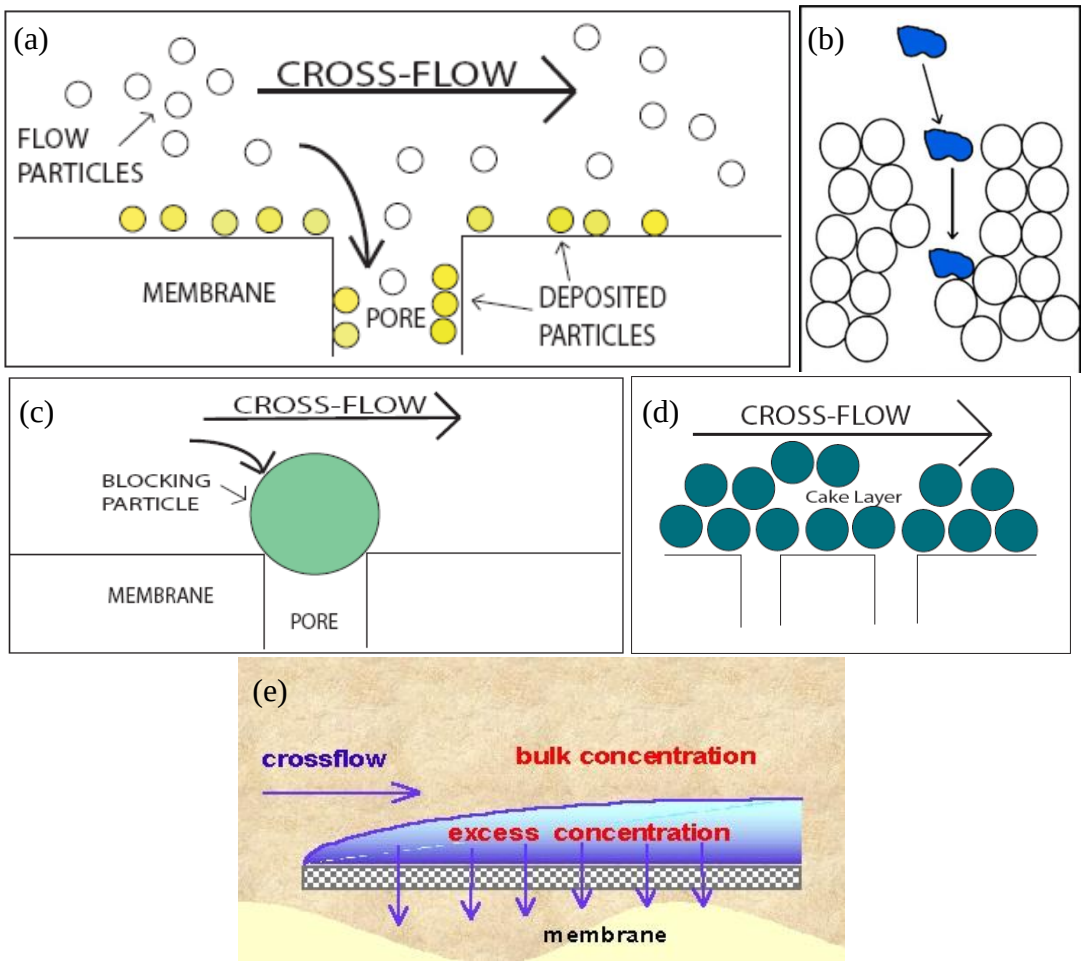

Figure 2.3 - Fouling Mechanisms Found in Microfiltration: (a) Adsorption, (b) Partial Pore Blocking, (c) Pore Blocking, (d) Cake Layer Development, and (e) Concentration Polarization [11, 21, 28]

Surface adsorption is the first fouling mechanism to appear during microfiltration. This fouling mechanism is caused by particles in the fluid adsorbing due to the concentration gradient between a clean membrane and the fluid [1]. These effects reduce the effective cross-sectional area of the pores and constrict flow through the pore [5]. Although the radial growth of the adsorbed layer in a pore is relatively slow and linear, the flux decline of the system due to this fouling mechanism is exponential [12]. Surface adsorption is typically

visualized via SEM images as slight uniform whitening of membrane pore edges [12] for all pores on the microfilter membrane.

Partial pore blocking occurs as the second fouling mechanism. This is typically realized as particles partially obstructing a pore entrance or the structures internal to a pore, due to the particle size being smaller than the pore diameter [11]. Particles then trap near the pore and cause particle obstruction and partial reduction of fluid flow through the pore. Almost all pores will see this effect due to a relative large number of particles in the fluid that are smaller than the pore size and become trapped in the membrane [13, 28].

Pore blocking occurs as the third fouling mechanism. This is typically occurring simultaneously with partial pore blocking when particles from the fluid are entering the membrane system. It is caused by size-exclusion or orientation-mismatch preventing particle entry into pore. Instead particles become lodged at the entrance of the pore. Not all pores become blocked due to the low probability of particles existing in the fluid that is larger than the pore. Flux is reduced exponentially [11]. This is visualized in SEM images as large scab- or scale-shaped plates overlaying one or multiple pore entrances.

Cake layer development, as the fourth fouling mechanism, is marked by a layer of MWF ingredients on the membrane surface. Due to blocked pore entrances, incoming colloids have difficulty entering the pores and stack on the membrane surface. The growth and the associated flux decline has a power law relationship [11, 12]. This fouling mechanism can be observed in SEM images as a thick coating of MWF ingredients on the surface; typically, the globular geometry of the microfilter is not visible.

Concentration polarization occurs during microfiltration equilibrium where the system flux tends to steady state. Balance of MWF ingredient mass transfer between the fluid and surface layer prevents change in the thickness of the cake layer [11].

2.1.3 Flux Decline as a Consequence of Microfilter Fouling

The flow reduction from the five fouling mechanisms was first identified as microfilter flux decline by Mahdi and Sköld during the microfiltration of synthetic MWFs [9]. In testing the capability of microfilters to recycle MWFs, they found reduction in flux during the filtration of three commercially available synthetic MWFs through a 0.2 to 0.8 μm pore diameter polypropylene microfilter. The reduction in flux is shown in Fig. 2.4.

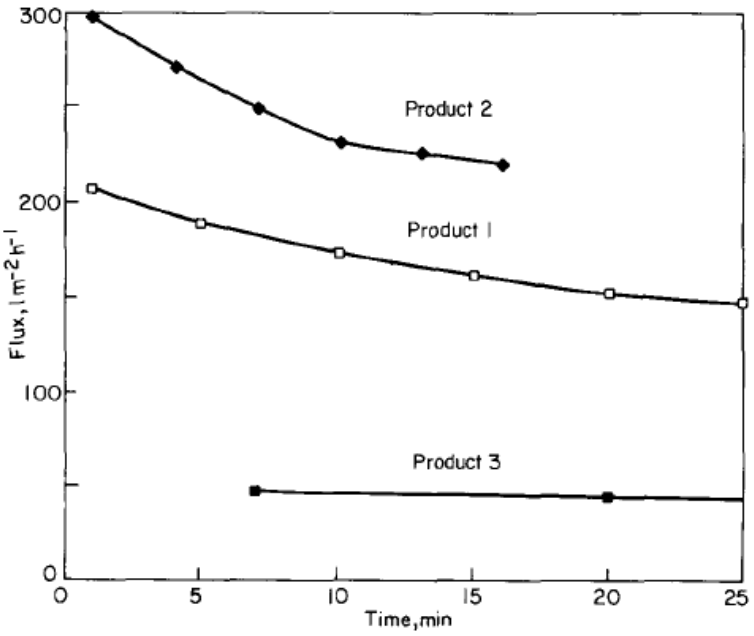

Figure 2.4 - Flux Decline during Microfiltration of Clean Synthetic MWF [9]

Although flux decline was found, the ability to remove contaminants and micro-organisms from the fluid via a careful selection of MWF and filter concluded that utilization of microfiltration can be used to extend the lifetime and sustainability of MWF systems.

Skerlos et al. [6, 7] performed experiments to understand the effect of different synthetic MWF chemical compositions on microfiltration productivity. Lubricants, defoamers, or biocides are important chemical components of the MWF constitution, however, they were identified as a burden to flux. Flux decline from experiments on different compositions of these additives can be seen in Fig. 2.5.

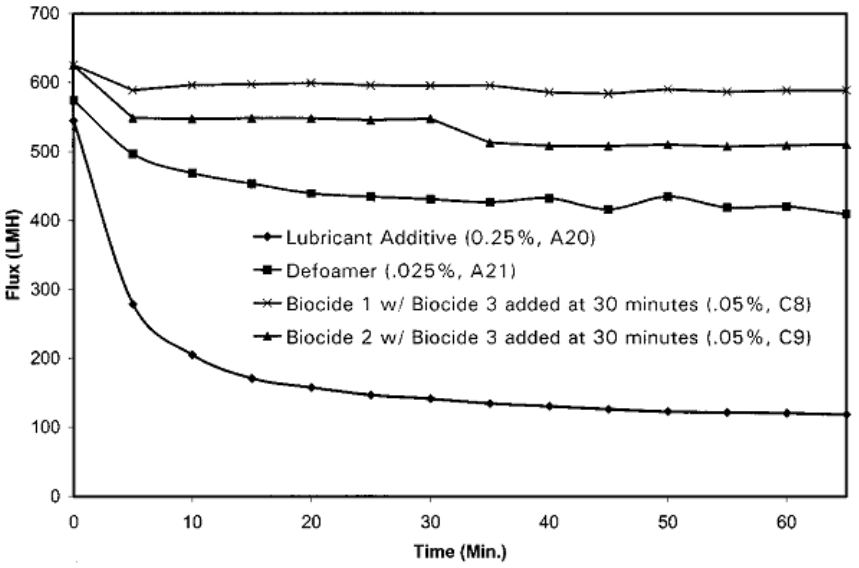

Figure 2.5 - Flux Decline from Included Additives [7]

His work was verified in works by [10] where designed MWFs with replaced or removed additives performed better than commercial fluids in flux decline. Moreover, empirical models of chemical constitutions, based on [6, 9, 10], were created and utilized for MWF

optimization that decreased flux decline by 300% to 800% without impacting machining performance [1]. The flux decline from the experiments in Fig. 2.5 was attributed to the adsorptive qualities of the additives. In fact, the adsorbed chemicals prevented the ability to regain original, pre-experiment, fluxes after typical microfilter cleansing. [22]. Nonetheless, their work correlated specific fouling mechanisms to flux decline.

For semi-synthetic MWFs, separation of contaminants, such as tramp oils, bacteria, and endotoxins, from the base fluid without major losses in the functionality of permeate was first successfully done by Rajagopalan et al. [2]. In passing hydraulic oil-laden MWF through microfilters, they obtained a 7 log reduction in bacteria-laden MWF and achieved fluid-contaminant oil separation.

The effect of altered MWF concentration and system operation variables on flux decline was experimentally investigated by Wentz et al. [4]. His tests with varying concentrations of MWF in crossflow microfiltration revealed similar non-zero steady-state flux after three days of operation (Fig. 2.6).

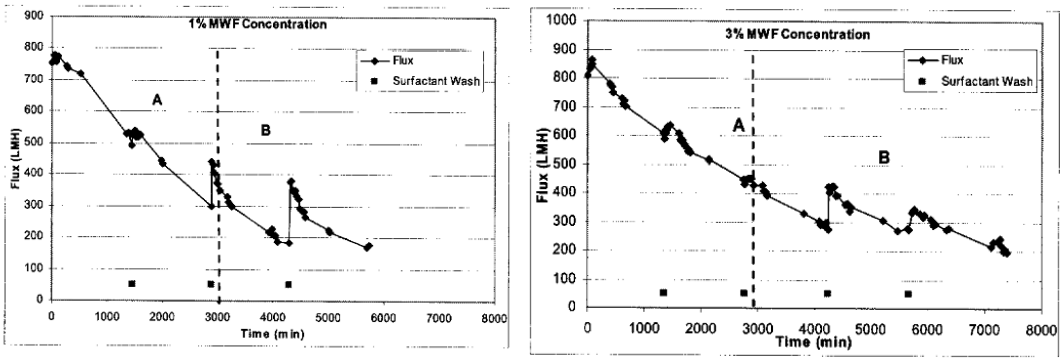

Figure 2.6 - Effect of MWF Concentration on Flux Decline [4]

From SEM images, he attributed the flux decline to particle deposition leading to pore restriction and then cake layer development. He was able to conclude that these fouling mechanisms affected flux decline, and their effect on flux decline can be reduced via altered microfiltration operation variables such as transmembrane pressure.

Wentz et al. went further to design semi-synthetic MWFs based on the findings of the fouling mechanisms prevalent in microfiltration as well as the operating parameters effective in increasing microfiltration efficacy [21]. He designed six semi-synthetic MWFs that differed in ingredient composition of chemicals that affected fouling. SEM images verified the non-fouling capabilities of the designed fluid, and the comparability of designed fluids to commercial fluids in flux decline and machining performance. Their work concluded that changes in composition affecting fouling were in fact effective in reducing fouling and maintaining flux, as shown in Figs. 2.7 and 2.8.

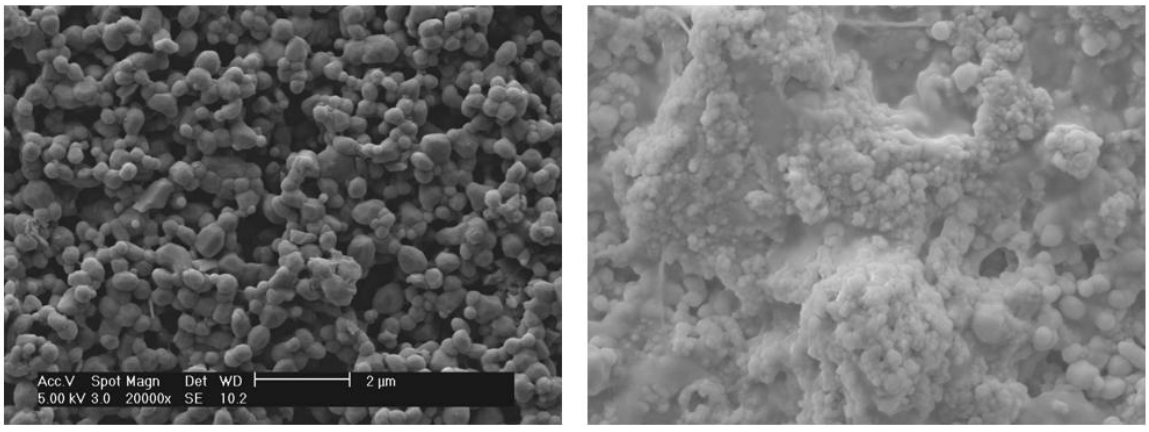

Figure 2.7 - New Microfilter and Used Microfilter after Operating with Commercial Semi-synthetic MWF [21]

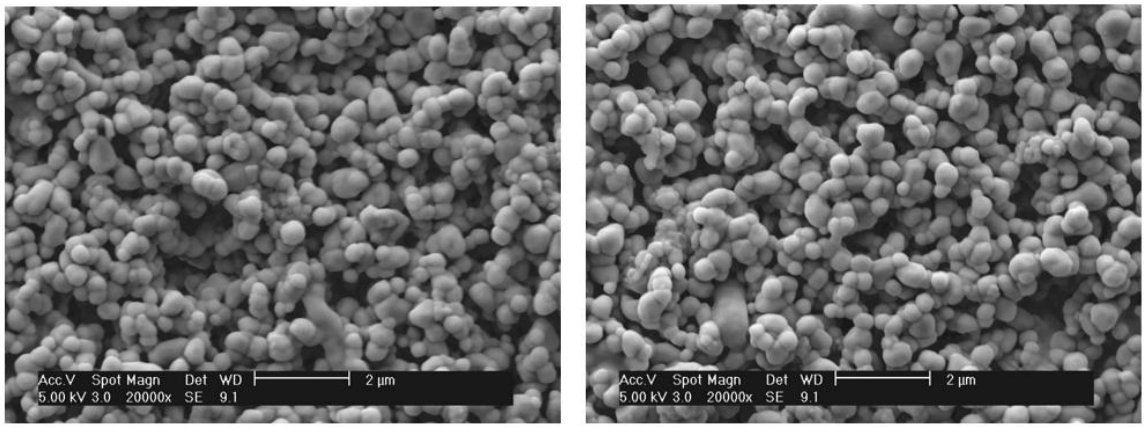

Figure 2.8 - Used Microfilter after Operating with Designed Semi-synthetic MWFs [21]

2.2 Predicting Flux Decline via Mechanistic Models

Although it has been verified via experiments and SEM images that interactions exist between fouling and flux decline, the mechanisms by which fouling lead to flux decline was not known. Section 2.2.l examines a mechanistic model of flux decline via pore blocking and cake layer development. Section 2.2.2 details the enhancement of the mechanistic model with the adsorption fouling mechanism.

2.2.1 Flux Decline Model of Pore Blocking and Cake Layer Development

A flux decline model based on mass concentration transport laws has been created by Song for pore blocking, cake layer development, and concentration polarization in infinite cross-flow microfiltration [11]. Since each of these mechanisms has a specific behavior to flux

decline, it was correlated to three stages of the flux decline curve: initial sharp flux decline, gradual flux decline, and finally steady state flux decline [11] (Fig. 2.9).

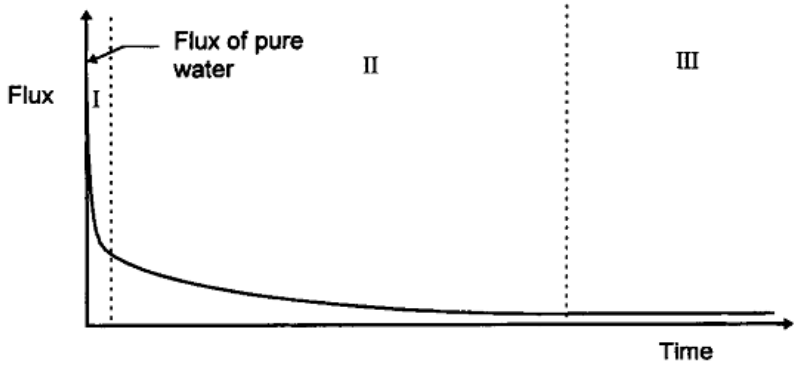

Figure 2.9 - Flux Decline from Fouling [11]

Typically these mechanisms occur in the stated order, however, two or more of these mechanisms may occur simultaneously in a combination of microfiltration stages. Flux, V, is linearly related to the transmembrane pressure, ΔP, and inversely related to the flow resistances of the fouling mechanisms in series,

$$V = \frac{\Delta P}{R_{pl}+R_m+R_c}, \tag{2.1}$$

where the flow resistances are the concentration polarization layer resistance, R_{pl}, membrane resistance, R_m, cake layer resistance, R_c.

The concentration polarization layer resistance depends on the critical pressure drop, ΔP_c, which is determined from foulant and fluid properties. Flux can therefore be simplified to be

a ratio of the net transmembrane pressure less the pressure drop of the concentration polarization layer and the resistances of the membrane and cake layer:

$$V = \frac{\Delta P - \Delta P_c}{R_m + R_c}, \tag{2.2}$$

Flux contributed from pore blocking is determined by considering that the relationship of the particle-to-membrane deposition rate is dependent on the number of particles pre-existing on the surface. This differential equation relating the pore blocking rate and number of pores currently open, *n*, may be solved to attain a function for the number of open pores at a given time. The initial condition is that there are no blocked pores on a clean membrane. The result of the differential equation is [12]:

$$n = n_0 e^{-\alpha t}, \tag{2.3}$$

where n_0 is the initial number of pores, α is the pore blocking time constant, and t is the independent variable time.

The number of open pores can be related to the initial flux, V_0, via the pore-specific flux for a given transmembrane pressure. The number of partially blocked pores also contribute to flux, V_{b0}, since not all pores are blocked. The sum of these two fluxes produces a function for the flux, $V(t)$, over time, *t*:

$$V(t) = V_0 e^{-\alpha t} + V_{b0}(1 - e^{-\alpha t}), \tag{2.4}$$

Since we know that the membrane resistance is no longer clean but instead has a new resistance to flow, R_m is substituted with R_{bm}, defined as the blocked membrane resistance.

$$V(t) = \frac{\Delta P - \Delta P_c}{R_{bm} + R_c}, \tag{2.5}$$

A cake layer develops after many pores have been blocked, and particles begin stacking in a compressed layer on the membrane surface. A function for the layer thickness growth can be used for determining the cake layer resistance, R_c:

$$R_c = r_c \delta(t)\ , \tag{2.6}$$

where r_c is the specific resistance of the cake layer. The term, $\delta(t)$, is the time-dependent thickness of the cake layer:

$$\delta(t) = \frac{1}{c_g} \int_0^t V c_0 dt, \tag{2.7}$$

which is an integral of the function defining the rate of particle deposition to the surface. c_g is the contaminant concentration on the cake layer, c_0 is the contaminant concentration in the bulk fluid, and *V* is the permeate flux.

Substitution of Eqn. 2.6 into Eqn. 2.5 and rearrangement gives the flux contribution due to cake layer development:

$$V(t) = \frac{\Delta P - \Delta P_c}{R_{bm}} \left(1 + \frac{2 r_c (\Delta P - \Delta P_c)}{R_{bm}^2} \frac{c_0}{c_g} t\right)^{-1/2}. \tag{2.8}$$

The three fouling mechanisms can now be unified with the substitution of Eqn. 2.8 into Eqn. 2.4, revealing the Song model:

$$V(t) = e^{-\alpha t} \frac{\Delta P}{R_m} + (1 - e^{-\alpha t}) \frac{(\Delta P - \Delta P_c)}{R_{bm}} \left(1 + \frac{2 r_c (\Delta P - \Delta P_c)}{R_{bm}^2} \frac{c_0}{c_g} t\right)^{-1/2}. \tag{2.9}$$

In summary, the Song model predicts the flux decline due to partial pore blocking, and cake layer development, and concentration polarization. His model however, does not capture the contribution of adsorption, which is deemed significant in flux decline [1, 7].

2.2.2 Flux Decline Model Including Adsorption

The partial pore blocking, cake layer development, concentration polarization, and adsorption fouling mechanisms were unified into one flux model by Zhao et al. [12]. Through the analysis of adsorption in microfilter SEM images, a similar flux model was developed for the flux contribution due adsorption in one pore, $v_{ads}(t)$:

$$v_{ads}(t) = \frac{\Delta P}{n_0 R_m}[e^{-\alpha_c t} + (1 - R^*)^4(1 - e^{-\alpha_c t})], \tag{2.10}$$

where R^* is the maximum fraction of radius reduction after flux has progressed to steady-state, i.e., the steady-state effective internal resistance.

The flux contribution from one fouled pore (Eqn. 2.10) was expanded to the flux contribution from all fouled pores on the microfilter via the time-dependent number of pores available to be fouled from Eqn. 2.3. The flux contribution from adsorption and pore blocking is therefore, $V_{ads,poreblock}(t)$:

$$V_{ads,poreblock}(t) = \frac{\Delta P e^{-\alpha_b t}}{n_0 R_m}[e^{-\alpha_c t} + (1 - R^*)^4(1 - e^{-\alpha_c t})], \tag{2.11}$$

Flux contribution from cake layer development is determined using Darcy's Law with flow resistance due to a time-varying cake layer thickness. This contribution is:

$$V_{cake\ layer}(t) = \frac{\Delta P}{R_{bm}}\left(1 + \frac{2*\Delta P*\psi*c_0*t}{R_{bm}^2}\right)^{-0.5}. \quad (2.12)$$

The flux decline due to these fouling mechanisms are expressed as a function of four governing variables that are used to characterize the flux contribution for fouling mechanism: the rate constant for internal restriction, α_c, rate constant for pore blocking, α_c, steady-state effective internal restriction, R^*, and specific surface film resistance, ψ. The Zhao et al. model is:

$$V(t) = \frac{\Delta P e^{(-\alpha_b*t)}}{R_m} \cdot \left(e^{(-\alpha_c*t)} + (1-R^*)^4 \cdot \left(1 - e^{(-\alpha_c*t)}\right)\right) + \frac{\Delta P}{R_m} \cdot \left(1 - e^{(-\alpha_b*t)}\right) \cdot$$

$$(1-R^*)^4 \cdot \left(1 - \frac{\sqrt{2}}{2}\right) \cdot \left(1 + \frac{2*\Delta P*\psi*c_0*t}{R_m^2} \cdot (1-R^*)^8 \cdot \left(1 - \frac{\sqrt{2}}{2}\right)^2\right)^{-0.5}$$

(2.13)

This model was experimentally validated; the results of which can be seen in Fig. 2.10 [12]. Additionally, multiple points of the curve, given a certain time of microfiltration, was independently observed via SEM images to have a given the flux predicted by the model (Fig. 2.10).

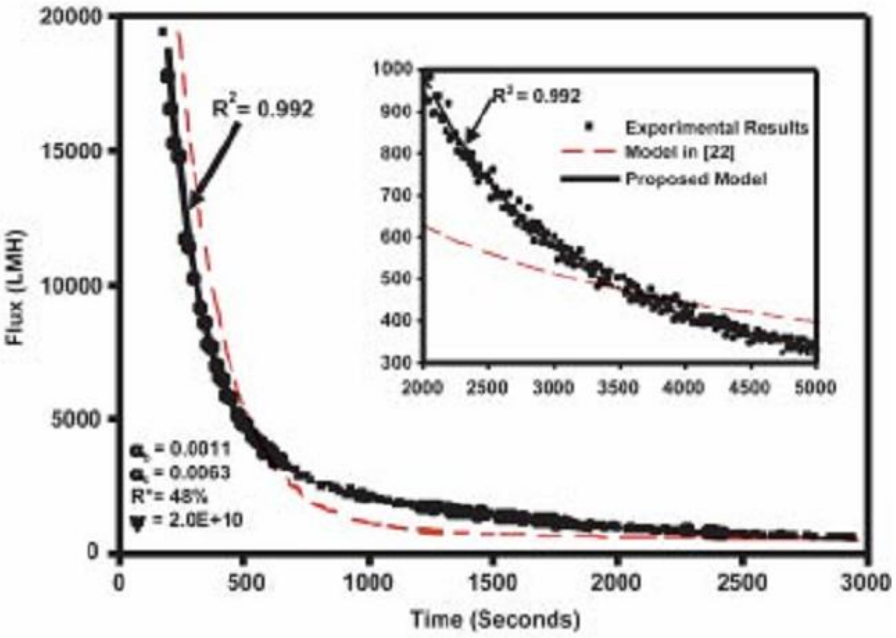

Figure 2.10 - Goodness of Fit of the Zhao et al. Model versus Experimental Results [12]

2.3 Predicting Flux Decline via Fluid Dynamic Models

Past authors [1, 2, 4, 5, 18, 19, 22] confirmed that fouling exists and affects flux decline, however, the physics behind what causes fouling was unknown. Fluid dynamic models were used to address this gap in knowledge by linking microfilter operating conditions, MWF physical properties, and geometry to fouling and flux decline [3, 8, 13]. Section 2.3.1 introduces the basic physics of fluid and particle dynamics within the fluid dynamic model that are applied in the following sections. Section 2.3.2 reviews the literature associated with the application of the physics to a fluid dynamic model in two-dimensional membrane geometries. Section 2.3.3 examines previous works that enhance the model to three dimensions.

2.3.1 Fluid and Particle Dynamics

Fouling behavior can be imitated and flux decline can be predicted via simulating physical conditions of experimental applications in a fluid dynamic model [3, 8, 13]. Governing forces of the fluid in the model are covered first. The interaction between the fluid and a colloidal particle are the hydrodynamic forces are then detailed. Electrostatic forces, caused by non-neutral bodies in the membrane, are examined in theory and in application. Stochastic movement in the form of Brownian motion is examined last in this subsection.

Fluid Dynamic Modeling Methodology

Fluid dynamic models utilized by various authors [3, 8, 13], implemented via FLUENT [29], are an aggregation of fluidic finite elements that make up a two- or three-dimensional space. Each of the finite elements hold physical property values, such as fluid velocity, density, and temperature, at its location, and is related to neighboring elements by models that govern the system. The fluid flow through a volume is modeled by solving the Navier-Stokes equations with steady-state incompressible flow in the absence of gravity terms [15]. The energy equations are also solved to establish cell temperatures for the stochastic temperature-dependent particle movement. The volume is a meshed geometry of a microfilter obtained via focused ion beam images of consecutive slices of a microfilter. The Navier-Stokes flow and energy equations are applied to all finite element cells via the commercial software FLUENT (ANSYS, Inc., Canonsburg, PA). Additionally, no-slip boundary conditions are established at boundaries of the geometry. Lastly, fluid inlet and outlets are established with

a given pressure, velocity, and temperature. All finite elements in the geometry are solved simultaneously to a set system residual error.

Hydrodynamic Forces

Hydrodynamic forces are forces imparted by the fluid motion onto a particle traveling through the pore geometry and form the underlying force applied to fluid dynamic models to simulate particle movement and disposition [3, 8, 13]. The particle movement is determined by numerical integration of the Langevin equation [29].

$$m_P \frac{du_P}{dt} = 6\pi\mu a[K_P u_P - K_f u_f], \tag{2.14}$$

where m_P is the mass of the particle, u_P is the velocity vector of the particle, u_f is the velocity vector of the neighboring fluid, μ is the dynamic viscosity, a is the particle radius, and K_P and K_f are the hydrodynamic hindrances, in matrix form, between the particle and the fluid and the particle and the system boundary. This equation was used in its current form in two-dimensional simulations [13] as well as in its enhanced form, including electrostatic, F_E, and Brownian forces, F_B [3, 8]:

$$m_P \frac{du_P}{dt} = 6\pi\mu a\left[K_P u_P - K_f u_f\right] + F_B + F_E. \tag{2.15}$$

The enhanced Langevin equation was also utilized in three-dimensions [15]. This equation, in conjunction with particle disposition-determination schemes enable the simulation of trapped particles in the fluid dynamic model representing fouling of the microfilter membrane.

Double Layer Electrostatic Forces

Double layer electrostatic forces are intermolecular attraction or repulsion between two charged particle surfaces in an electrolyte [30]. In colloidal systems such as MWFs, the extent of electrostatic forces applied can affect the compatibility of semi-synthetic MWFs with microfiltration, and therefore such forces have been implemented in fluid dynamic models [3, 8]. However, due to the non-intuitive nature of this phenomenon, the theory by which electrostatic forces arise is reviewed.

These interactions define the stability of solutes in solutions; in MWFs, stability ensures lubricating capabilities and non-fouling compatibility with microfilters. Colloids in MWFs typically have a charge dependent on the pH of the fluid [31]. The magnitude and sign of the charges causes two particles to attract or repel, and changes in electrostatic forces may cause the colloids to coagulate, reducing the effectiveness of the MWF [26]. Understanding the physics behind colloid charges can have an effect on MWF stability and compatibility with microfilters.

Colloidal electrostatics was first recognized by Helmholtz, whom modeled surface electrostatics as a capacitor: charge decreased linearly versus the distance away from the surface. The model was viewed differently by Louis Georges Gouy and David Chapman, whom found that the electric potential of the surface decreased exponentially away from the surface of the particle or colloid. Stern later combined the two surface electrostatic models into a double layer: the Helmholtz layer consisting of a linearly decreasing charged layer and the Gouy-Chapman layer consisting of an exponentially decreasing charged layer external to

the Helmholtz layer. This model is known as the Gouy-Chapman-Stern electrostatic model and can be seen in Fig. 2.11.

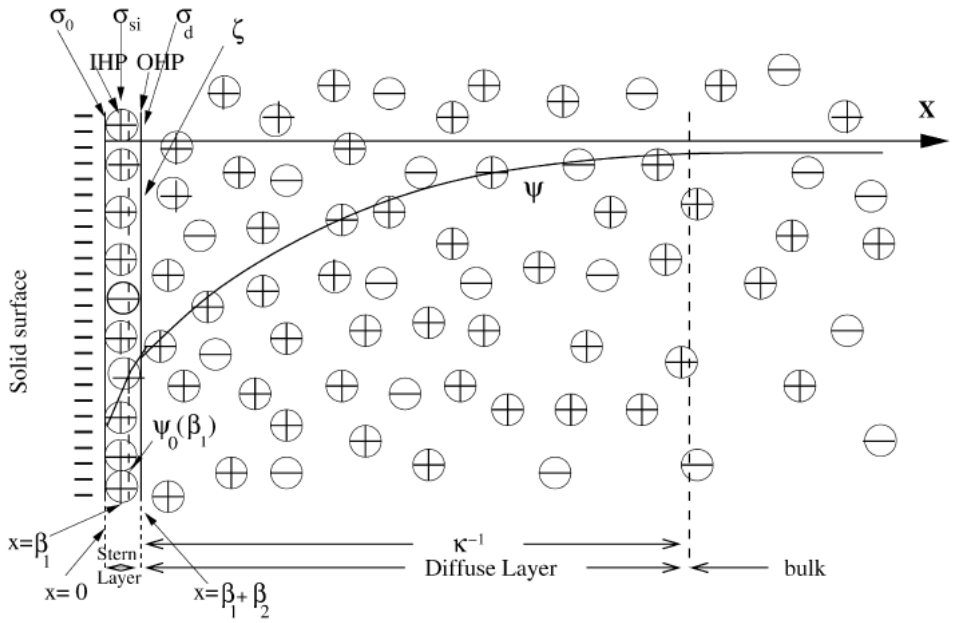

Figure 2.11 - Gouy-Chapman-Stern Electrostatic Model [32]

At the surface of the particle, the surface electric potential (versus the potential of the bulk flow) is established by the chemical makeup of the colloid. The charge of the surface potential attracts ions of different charges from the bulk fluid towards the surface of the colloid, forming two layers: the Stern layer and the Gouy-Chapman (diffuse) layer.

The Stern layer consists of counter-ions (ions of opposite charge to the colloid surface), which are rigidly attracted to the surface of the colloid and do not move when external forces are applied. The Stern layer thickness is on the magnitude of 0.2 nm but can change according to the ion size and surface and fluid parameters. [32]. At the distance away from

the surface where the surface electrostatic charge no longer holds counter-ions as rigidly, a slipping plane is developed. Here, counter-ion charges can easily move with external fluid dynamic or electric forces. Due to this mobility, the movement of this layer against an externally applied electric potential can be experimentally measured and correlated to the zeta potential.

Beyond the slipping plane, non-static counter-ions form the diffuse layer. Here, electric potential decreases exponentially according to the Gouy-Chapman model. At the outer regions of the diffuse layer, the counter-ions become the more potent charge in the volume around the colloid, hence, co-ions (ions of like charge to the colloid surface) are attracted to the colloid. The co-ion layer develops on the outside of the diffuse layer until the counter-ion and co-ion charges equilibrate with the ions in the bulk fluid solution. This equilibrium point to the colloid surface is a distance called the Debye length or Debye screening length which can be shortened or lengthened according to the ionic charge of the system. This metric also governs the ability to screen out charge effects of another colloid when the surface-to-surface distance is greater than the Debye length [30, 31].

The electrostatic double layer is modeled with the Poisson Boltzmann equation:

$$\nabla^2\Psi = \kappa^2 \sinh(\Psi), \tag{2.16}$$

where $\Psi = ve\psi/kT$ is the reduced surface potential, v is the charge number, e is the charge of an electron, k is the Boltzmann constant, T is the absolute temperature of the system, and κ is the inverse Debye screening length. Due to difficulties in obtaining analytical solutions for this nonlinear differential equation, it was linearized by Peter Debye and Erich Hückel through consideration of the first-order Taylor series expansion on the hyperbolic sine, and

an assumption that the electric potentials in colloidal MWF systems are small. The linearization additionally infers that the electrostatic potential for the system is not large compared to *kT*. The resulting Debye-Hückel equation, or the Helmholtz equation, is:

$$\nabla^2\Psi = \kappa^2\Psi, \tag{2.17}$$

The potential field from the Helmholtz equation can then be approximated through the Derjaguin approximation [33, 34] or solved numerically through the Surface Element Integration technique [35-37].

Derjaguin Approximation of Double Layer Electrostatic Forces

The Derjaguin approximation finds the double layer electrostatic force between two surfaces. As mentioned in the previous subsection, electrostatic forces are important in fluid dynamic models due their added accuracy in comparison to actual microfiltration applications. Therefore, the electrostatic force models have been implemented in current fluid dynamic models [3, 8, 14, 15] in the form of the Derjaguin approximation.

The Derjaguin approximation establishes the interaction energy of curved surfaces from flat plates, there we start the derivation with a flat plate. The total interaction energy of two flat plates, $U(h)$, is an area integral of the interaction energy per unit area, $E(h)$, of the flat plates, given a distance between the plates, *h*:

$$U(h) = \int E(h)dA. \tag{2.18}$$

Contrary to two parallel flat plates where h is constant, curved surfaces change how $E(h)$ is derived. Assuming two interacting, symmetric, constant curvature, surfaces, the integral need only be evaluated from the point of closest contact, *D*, to infinity. The resulting equation for curved surfaces is:

$$U(h) = f(a_1, a_2) \int_D^{\infty} E(h) dh, \tag{2.19}$$

where f is the function of the curvatures, dependent on the two mating surfaces curvatures a_1 and a_2, and describes how the distance between two surfaces change over the intervals of integration. The function of the curvatures has been solved for certain pairs of geometries such as a sphere-flat plate and sphere-sphere. These are called steric factors. The steric factor frequently referenced in simulations [8, 14, 15] is that of a sphere-sphere interaction, typically between a traveling spherical particle and the spherical particles trapped in the pore membrane. This steric factor is:

$$f(a_1, a_2) = \frac{1}{a_1} + \frac{1}{a_2}. \tag{2.20}$$

We know $E(h)$ from DLVO (Derjaguin and Landau, and Verwey and Overbeek) theory to include electrostatic repulsion from overlapping electrical double layers and van der Waals molecular attraction. However, we ignore van der Waals forces because the surface-to-surface distance of these electrostatic forces are much larger than the effective applicability distance of approximately 10 nm [30, 38]. The electrostatic interaction energy per unit area is [33]:

$$E(h) = \kappa \varepsilon_r \varepsilon_0 \left[\frac{2\psi_1 \psi_2 \exp(\kappa h) - (\psi_1^2 + \psi_2^2)}{\exp(2\kappa h) - 1} \right], \tag{2.21}$$

where ε_r is the dielectric constant, ε_0 is the permittivity of free space, and ψ_1 and ψ_2 are the surface potentials of the two surfaces. We substitute the electrostatic interaction energy per unit area, Eqn. 2.21, into the Derjaguin approximation, Eqn. 2.18, and integrate to obtain the electrostatic interaction energy [33]:

$$U(h) = \frac{\pi\varepsilon_r\varepsilon_0}{f(a_1,a_2)}((\psi_1^2 + \psi_2^2)^2\ln(1 + \exp(-\kappa h)) + (\psi_1^2 - \psi_2^2)^2\ln(1 + \exp(-\kappa h))). \quad (2.22)$$

This electrostatic interaction energy is then differentiated in respect to the distance between surfaces to obtain the electrostatic force on a spherical particle, F_E [8, 33]:

$$F_E(h) = \frac{2\pi\kappa\varepsilon_r\varepsilon_0}{f(a_1,a_2)}\left[\frac{2\psi_1\psi_2\exp(\kappa h) - (\psi_1^2+\psi_2^2)}{\exp(2\kappa h)-1}\right]. \quad (2.23)$$

The electrostatic force is then utilized in the Langevin equation, Eqn. 2.15, for determination of its effect on particle movement.

Brownian Motion Forces

At macro-scales, Brownian motion causes a particle to deviate from its prescribed pathline due to random walk. At sub-micron scales, Brownian motion can be seen as a "jiggling" motion of the particle in space, caused by the impacts of fluid molecules surrounding a particle. Although it is a seemingly small force versus hydrodynamic or electrostatic forces, its impact has been shown to cause significant diversions to particle trajectories and effects on particle dispositions [8, 14]. Therefore, it has been therefore has been implemented in various fluid dynamic models to date [3, 8]. The theory is first discussed prior to its implementation.

The impact of Brownian motion, as the breakdown of the continuum assumption for particle movement, is evident in the many works where its inclusion has changed the outcomes of fluid dynamic models [8, 15].

This impact is only applicable, however, if the Knudsen number is near or greater than unity. In these conditions, the continuum assumption of particle movement does not hold as a good approximation—discrete particle effects exist [39]. The Knudsen number is a non-dimensional number defined as the ratio of the fluid mean free path and the particle characteristic length,

$$Kn = \frac{\lambda}{D}, \tag{2.24}$$

where λ is the mean-free path and D is the particle diameter. Diameters of the injected particles range from 25 nm to 500 nm causing the Knudsen number to range between 0.5 and 5. The magnitudes of these Knudsen numbers therefore allow particles to be affected by discrete effects, nullifying the continuum approximation of particle movement. The discrete effects are modeled by Brownian motion, the random walk of the bulk particle caused by forces from fluid particles. The amplitude of the Brownian force components are:

$$F_B(t^+) = G_i\sqrt{\frac{\pi S_0}{\Delta t^+}}, \tag{2.25}$$

where G_i are the three zero-mean, unit variance independent Gaussian random numbers for the components of the Brownian force [40], and Δt^+ is the time increment at time t^+ of the simulation. The spectral intensity, S_0:

$$S_0 = \frac{2}{\pi S_c \tau_p^{+2}}, \tag{2.26}$$

is a function of different fluid parameters, S_c, the Schmidt number of the fluid and, τ_p^+, the Stokes number [29, 40]. The Stokes number is defined as:

$$\tau_p^+ = \frac{1}{18} C_c S d^{+2}, \tag{2.27}$$

where C_c is the Cunningham correction factor. S is the density ratio and d^+ is the dimensionless particle diameter, both of which are given here:

$$S = \frac{\rho^p}{\rho^f}, \qquad d^+ = \frac{du^*}{v}, \tag{2.28}$$

where ρ^p and ρ^f is the particle and fluid density, respectively, u^* is the shear velocity in the viscous sublayer, and v is the kinematic viscosity.

The numerical determination of these variables within FLUENT allows stochastic forces to be determined for the traveling particle [29]. This force is an integral part of the simulations as it has been shown by various authors [3, 8] that the existence of stochastic forces can cause changes in the disposition of a particle. Moreover, through validation, it was found that the steady-state flux was different between models with and without Brownian forces. Due to the difference that Brownian motion can make on these simulations, these forces are included in the fluid dynamic models.

2.3.2 Simulation in Two-dimensional Pore Geometries

Kim et al. [8] simulated particle movement at an ideal pore geometry entrance (Fig. 2.12).

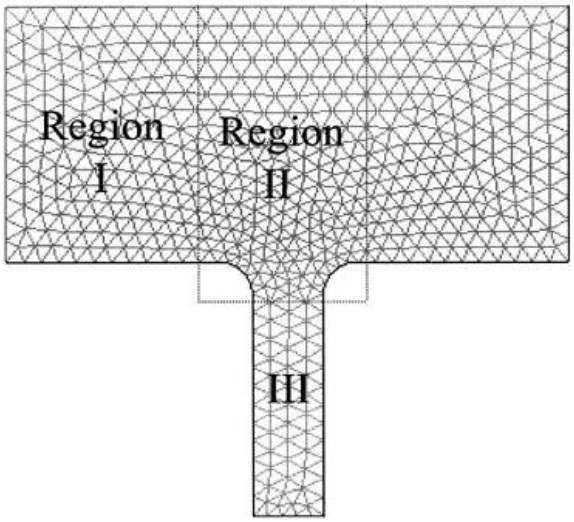

Figure 2.12 - Ideal Pore Geometry [8, 14]

They utilized the Derjaguin approximation for pair-wise electrostatic forces, such as the particle-particle and particle-membrane electrostatic forces, and the Ounis et al. [40] model for Brownian forces. The effect of these forces on particle trajectories are found in Fig. 2.13.

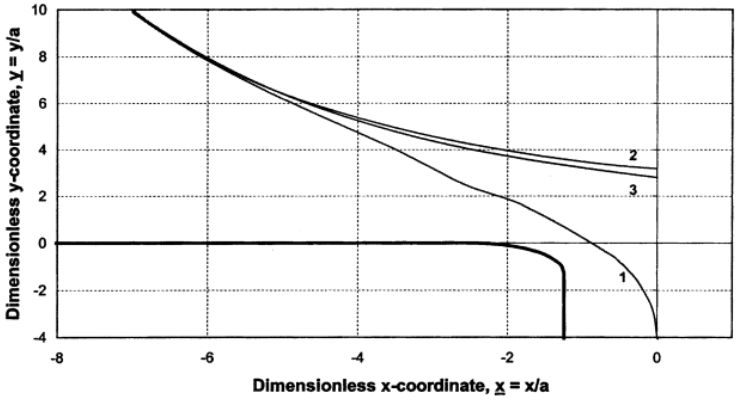

Figure 2.13 - Differences in Particle Trajectory due to (1) No Enhanced Drag or Electrostatics; (2) No Enhanced Drag and Electrostatics; (3) Enhanced Drag and Electrostatics [8]

They varied these forces to determine the impacts of enhanced hydrodynamic drag, electrostatic, and Brownian motion forces on particle pore entry. Their basis of quantification on whether a change affected a particle was the critical filtration velocity, which governs the minimum fluid velocity that allowed a particle to enter the pore, e.g., a high critical filtration velocity allows fewer particles to enter a pore. This velocity decreased with decreased electrostatic forces and increased with increased electrostatic forces. Furthermore, the inclusion of Brownian forces reduced the critical filtration velocity. They concluded that electrostatic forces and Brownian motion were significant in fluid dynamic models because of their effect on particle disposition.

Wentz et al. [13] applied the work completed in ideal two-dimensional pores to tortuous pores via a fluid dynamic model accurate to actual microfilter geometry. He recreated particles similar to MWF colloidal ingredients via SEM images of the trapped particles on a fouled membrane surface. The particles are seen in Fig. 2.14.

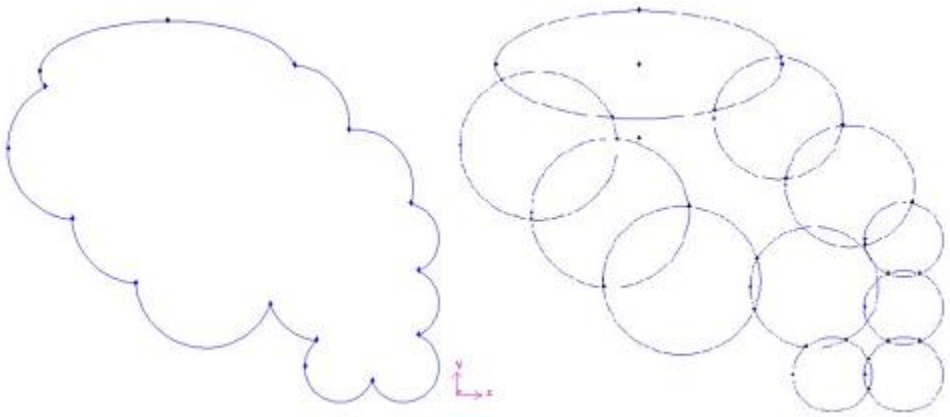

Figure 2.14 - Creation Methodology of Verisimilar MWF Particles [13]

He obtained particle size distributions of the MWF after different in-use times via dynamic light scattering techniques. Table 2.1 shows the particle size distribution. The two-dimensional tortuous pore geometry was recreated via SEM images of the microfilter, as shown in Fig. 2.15.

Table 2.1 - MWF Particle Size Distribution [13]

Size (nm)	0 min (%)	60 min (%)	180 min (%)	300 min (%)	480 min (%)	1000 min (%)	1620 min (%)	2000 min (%)
25–30	78.19	75.96	61.3499	63.8945	72.9304	78.2314	74.293	71.7668
30–35	20.66	22.52	33.8286	28.1476	22.2375	18.7148	22.7676	27.5344
35–40	1.153	1.525	4.82108	7.0245	4.26086	2.79628	2.86832	0.69687
40–50	0.555	0	0.48964	0.01779	0.03484	0.78015	0.05485	0.77152
50–60	0.458	0.677	0.14081	0.04934	0.04222	0	0	0
60–80	0	0	0.09109	0.00046	0.00712	0.02045	0.00793	0.00177
80–100	0	0	0.00016	0	0.00339	0.00377	0.00578	0.00553
100–125	0	0	0.00019	0	0.00058	0	0.00197	0.00593
126–150	0	0	6.1×10^{-5}	0	0.00011	0.00103	0.0005	0.00245
151–200	0	0	9.3×10^{-6}	6.2×10^{-6}	1.6×10^{-5}	0.00026	0.00025	0.00067
200–250	0	0	3.1×10^{-7}	5.6×10^{-6}	2.3×10^{-6}	6.8×10^{-5}	9.6×10^{-5}	0.00015
250–300	0	0	0	3.7×10^{-7}	1.7×10^{-6}	2.7×10^{-5}	4.5×10^{-5}	1.4×10^{-5}
300–350	0	0	0	6.7×10^{-8}	0	5×10^{-6}	9×10^{-6}	3.3×10^{-7}
350–400	0	0	0	0	1×10^{-6}	7.8×10^{-7}	3.7×10^{-7}	1.6×10^{-6}
400–450	0	0	0	0	0	1.8×10^{-7}	0	0
450–500	0	0	0	0	0	0	2.3×10^{-7}	9.3×10^{-8}
500–550	0	0	0	0	0	0	0	7.3×10^{-8}

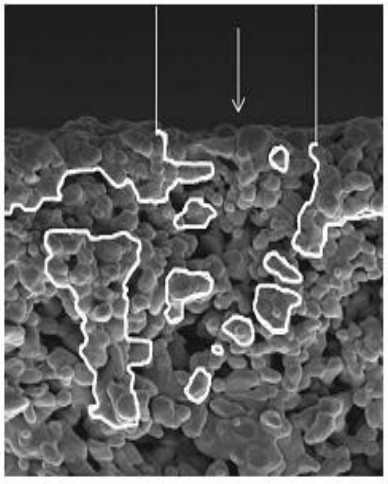

Figure 2.15 - Pore Structure via SEM Images [13]

The actual structure was meshed in GAMBIT, established with inlet and outlet boundary conditions, and exported into FLUENT for fluid simulation and particle trajectory simulation via the Langevin equation. The simulation process for the fluid dynamic models is:

1. Randomly select a particle shape;
2. Randomly select a particle size according to size distributions;
3. Randomly select an initial particle location;
4. Randomly select an initial particle orientation;
5. Simulate the particle trajectory through the pore area;
6. Evaluate the particle path. If the particle:
    a. escaped, continue from step 2;
    b. becomes trapped, continue to step 8;
7. Remesh pore area with the inclusion of the stuck particle;
8. Restart the simulation at step 1;

This process was repeated until the flux decreased to zero. A zero flux meant that all available pores are blocked and no fluid is able to flow from the inlet to the pressure outlet. A sample trajectory through the fluid dynamic model is seen in Fig. 2.16.

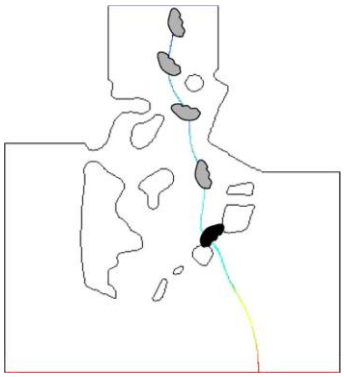

Figure 2.16 - Blocking of a Tortuous Pore [13]

The effect of inlet pressure on fouling and flux decline was investigated via the fluid dynamic model. Simulations were run according to the simulation process and flux data was recorded for each particle that trapped. He found that low shear (low crossflow velocities via low transmembrane pressures) caused flux to be maintained for twice as long as that in the high shear simulation. Additionally, reduced cross-flow velocity reduced the flow rate through the pore area. Lastly, as particles partially blocked the pore inlets or exits, other particles injected afterwards would stack on previously stuck particles. The continued stacking effect reduces flux continuously until all exits are blocked and flux is zero. From this work, they concluded a successful implementation of operating conditions in a geometry that is accurate to the pore structure, while predicting flux decline from inter-pore fouling. Furthermore, partial pore blocking was visualized as a fouling mechanism.

Ham et al. [3] extended the work of Wentz et al. with particle-particle electrostatic and Brownian forces in the same tortuous two-dimensional pore geometry. The PP-electrostatic forces were implemented via the Derjaguin approximation. The PM-electrostatics, however, were ignored by assuming that the pH of the MWF matched the point of zero charge of the alumina microfilter membrane [41]. Zeta potentials for the PP-electrostatic forces were

determined by electrophoresis via the Malvern Zetasizer. Brownian forces utilized the Ounis et al. [40] model.

Ham et al. obtained particle trajectories using the same simulation methodology as Wentz et al. [13]. The effect of the inclusion of hydrodynamics, PP-electrostatic forces, and Brownian forces can be seen in Fig. 2.17.

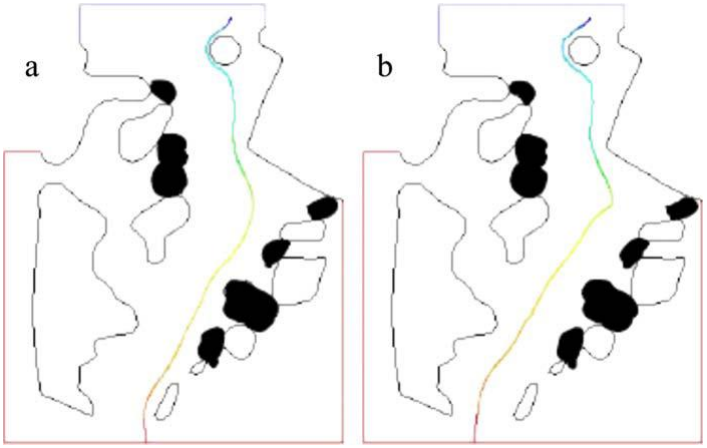

Figure 2.17 - Particle Trajectories from Only Hydrodynamics (Left) and a Combination of Hydrodynamics, PP-Electrostatic Forces, and Brownian Forces (right) [3]

Existence of stochastic forces in the simulations changed the disposition of certain particles, similar to the work of Kim et al. [8]. Their work revealed the necessity to include Brownian and PP-electrostatic forces in fluid dynamic models.

Their work also simulated a separate model under the effects of PM-electrostatic forces. The authors also determined the effect of the PM-electrostatic forces on particle movement via a combination of finite element analysis in MATLAB and FLUENT. To highlight the effect of PM-electrostatic forces sole on particle disposition, a new tortuous geometry was created.

Due to non-ideal geometries, the Derjaguin approximation could not be used to calculate the electrostatic force. Thus, a finite element model was utilized in MATLAB for the non-realtime determination of the electric potential around the pores. The potential strength and location data was exported from MATLAB and incorporated in compiled code in FLUENT electrostatic models. The prepared fluid dynamic model can be seen in Fig. 2.18.

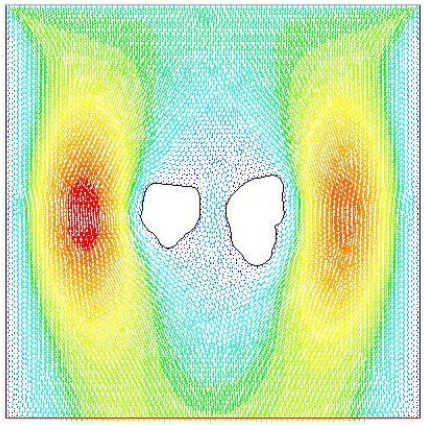

Figure 2.18 - Geometry and Flow for Investigation of Electrostatic Forces [3]

The electrostatic force, Brownian motion, and hydrodynamic forces were applied to injected particles. Particle disposition was found to finalize in three manners, shown in Fig. 2.19.

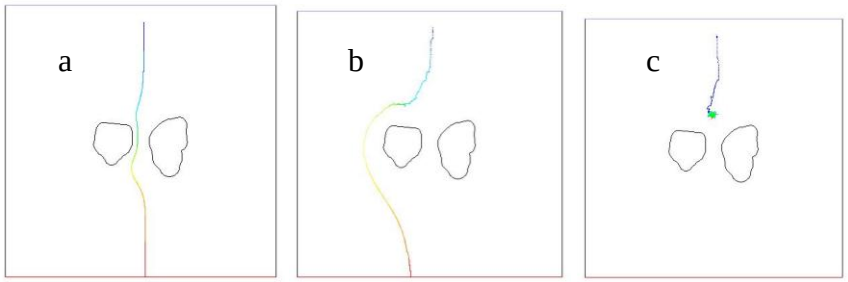

Figure 2.19 - Particle Dispositions: (a) Pass Between; b) Pass Around; c) Become Trapped [3]

Fouling took place in Fig. 2.20(c) and the number of particles becoming trapped was shown to vary depending on the extent of applied electrostatic and hydrodynamic forces. This in turn was conceptualized as an increased flux decline. Furthermore, their work showed that PM-electrostatic forces were important in the mechanisms by which fouling occurs.

Flux decline in experiments typically do not trend to zero steady-state in cross-flow microfiltration, however, that in fluid dynamic models showed otherwise. Geometries were expanded to three-dimensions to capture additional effects that were otherwise unable to be captured in the limited degrees of freedom for particle movement in two dimensions.

2.3.3 Simulation in Three-dimensional Pore Geometries

Ham et al. [15] simulated flow through a three-dimensional approximation of the tortuous pore paths of the microfilter. This was done because two-dimensional fluid dynamic models did not accurately model partial pore blocking, and models simulating one pore are not equivalent to the porous membranes in actuality [8, 13, 14]. Ham simulated flow through a six-pronged juncture with one fluid inlet and five fluid outlets (Fig. 2.20). Different sized

particles were injected into the system and its disposition was determined. The geometry of the trapped particles was removed from the geometry for each particle that became trapped. The flux decline profile was created through the reduction of the effective flow area as particles became trapped.

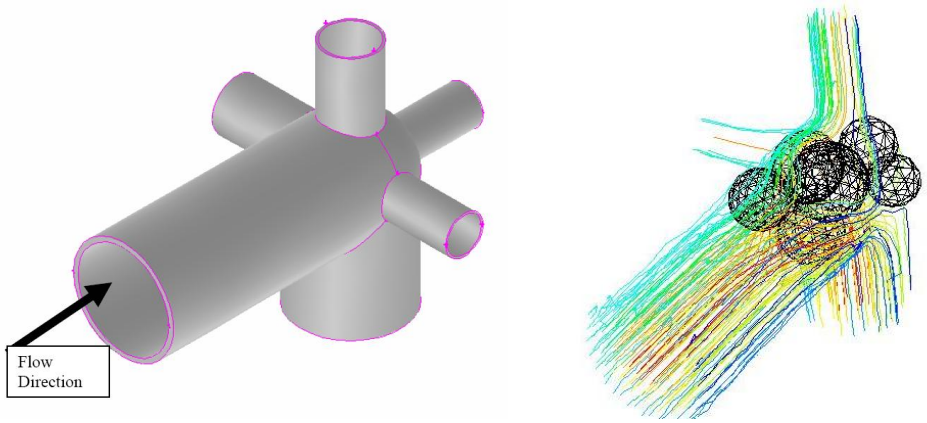

Figure 2.20 - Simulation Image of Six-pronged Juncture (left) and Flow Profile after Pore is Partially Blocked (right) [15]

Pore flow areas in these three-dimensional fluid dynamic models did not become completely blocked like it did in two-dimensional simulations [3, 13]. Instead, partial pore blocking occurred, reducing the effective cross-sectional area of the system in simulations to 42% of its original value. Flux decline was able to be digitally determined from the system and showed values that were non-zero.

Ham also simulated three-dimensional flow through an ideal geometry pore membrane composed of layers of cylinders with holes cut into each cylinder. Each layer of cylinder was rotated 45° from one another such that the overall four-cylinder layer imitated the tortuous nature of the actual microfilter membrane. Two sets of cylinders with different hole sizes

were created to determine the effect of pore sizes on flux decline via pore blocking; they can be seen in Fig. 2.21.

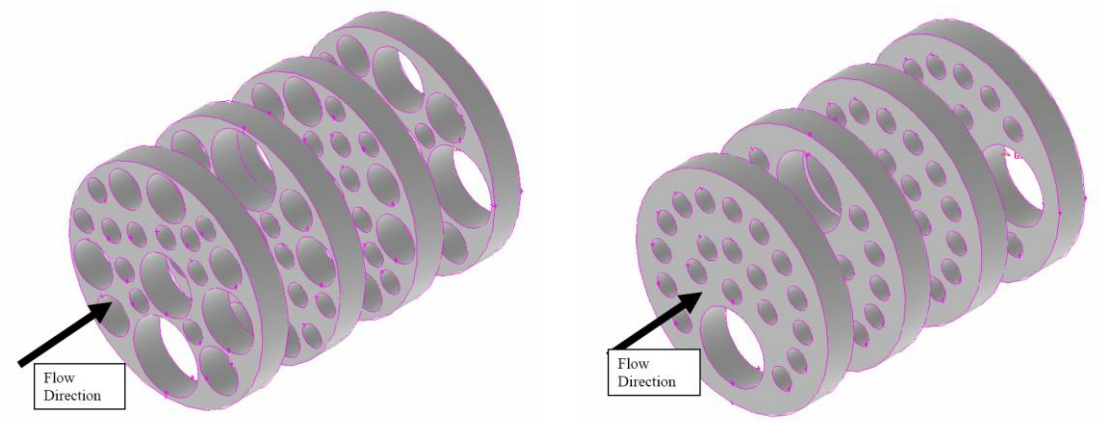

Figure 2.21 - Stacked Cylinder Pore Geometries with (Left) Varied-sized Pores and (right) Uniform-sized Pores [15]

Particles were sent through the geometry with a size based on the particle size distribution of Wentz et al. [13]. Particles that became stuck rested on the surface of the membrane and its geometry was removed from the geometry mesh, as shown in Fig. 2.22. This continued until flux obtained steady state or injected particles were not able to significantly alter flux decline. The simulation flux decline results were obtained for each particle for each of the cylinder and shown in Fig. 2.23.

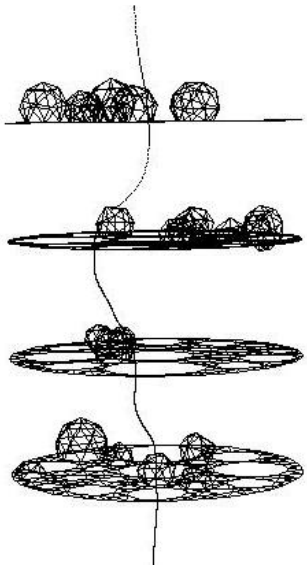

Figure 2.22 - Trapped Particles with Particle Trajectory [15]

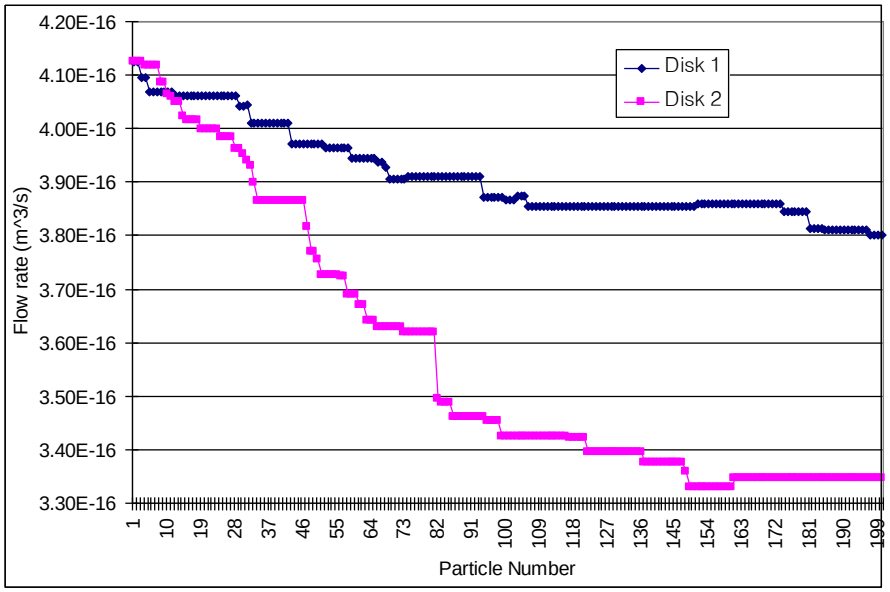

Figure 2.23 - Simulated Flux Decline of Two Disc Microfilters [15]

Flux flow in simulations decreased linearly and reached steady state after a certain amount of filtration time. This behavior was similar to what was shown in experiments. His conclusions

visually confirmed the partial pore blocking fouling mechanism and the viability of three-dimensional simulations to predict flux decline.

2.4 Summary and Gaps in Knowledge

The first steps taken to understand microfilter flux decline due to MWF fouling were experiments. Different chemical compositions of MWFs and additives were tested to find their effect on flux decline. Empirical models were created to understand and predict the effects of MWF ingredient compositions on flux decline. Throughout these experiments, four stages of fouling were detected via microscopy and, in turn, were studied to understand how they develop.

Fouling was simulated via fluid dynamic models to understand their inception and their effect on flux decline. Tortuous two-dimensional fluid dynamic models found particles trapped in pores, revealing partial pore blocking as another fouling mechanism and one of the drivers for cake layer development. Models increased in accuracy with the inclusion of particle-particle electrostatic forces and Brownian motion, leading to the inter-pore blocking. Lastly, particle-membrane electrostatic forces were found to be significant in determining whether a pore becomes blocked.

Simulations expanded to ideal three-dimensional pore geometries, and force models also scaled to three dimensions. One intersection of six pore passageways was modeled to show how particles accumulate at the intersection. Results showed that although partial pore blocking occurred, flux was not reduced to zero as predicted in all previous fluid dynamic

models operating in two dimensions. Instead, gaps in the fluid system remained and allowed flux to trend to a non-zero steady state. More complex pore geometries were developed to imitate the tortuous geometry of microfilter membranes. Results from simulations in these geometries showed that flux decline was being affected by system and fluid parameters, resulting in varying flux decline that showed similarity to experimental flux decline data.

However, some gaps in knowledge remain to be filled. Simulated MWF colloids travel in idealized pore geometries and could only be trapped in single passageway intersections or in specific locations purposely modeled to become blocked. Moreover, previous works [3, 8, 13] simulated particle movement with a point mass approximation, generating trajectories with unlikely particle movement. These two limitations are atypical of actual microfilter geometry and therefore do not give the best approximation to the progression of fouling and the associated flux decline. Particle-membrane electrostatic forces were not included in previous works due to the assumption that the point of zero charge precluded such forces from implementation. However, the assumption does not apply in general, and the absence of particle-membrane electrostatic forces in fact has a profound effect on fouling and flux decline. Lastly, trends in flux decline can currently be predicted, but the lack of experimental validation makes prediction of flux decline in actual experiments difficult.

The following chapter details the three-dimensional tortuous pore geometry recreation process, the particle disposition scheme development and application, and the simulation process employed by the fluid dynamic model to simulate the progression of fouling and the associated flux decline. The next chapter details the enhanced fluid dynamic model, its validation process, and the investigation of variables governing fouling phenomena on flux decline. Conclusions from this thesis are then presented.

Chapter 3

Simulation of Fouling in a Three-dimensional Tortuous Pore Geometry via a Fluid Dynamic Model

3.1 Overview

In this chapter, a three-dimensional verisimilar model of a microfilter is developed for the simulation of fouling and the associated flux decline in cross-flow microfiltration. The model shows how MWF colloids block tortuous, non-idealized, pores. The model incorporates hydrodynamic, electrostatic, and stochastic forces and particle-membrane collision models. Moreover, the simulation offers a flux decline profile similar to experimental results and reveals how the particle trapping model promotes cake layer development as a primary fouling mechanism.

This chapter commences with the presentation of tortuous membrane feature capture and the creation of the three-dimensional geometry. Next, the theory for the forces acting on the

fluid and particle within the geometry is discussed. The simulation methodology is then examined. The chapter finally examines simulation results and closes with conclusions.

3.2 Pore Geometry Recreation

In this section, the two steps used to recreate the pore geometry are discussed: (1) the material removal and microscale imaging process for imaging consecutive slices of a microfilter; and (2) the tortuous geometry recreation for converting said slices into a three-dimensional volume.

3.2.1 Microscale Material Removal and Imaging

The microstructure of the filter in Fig. 3.1 consists of two components: large-scale support structure, and small-scale sintered α-alumina (Al_2O_3) filter. The support structure has particles in the tens of microns, whereas the filter has particles in the tenths of microns. The material under investigation is the latter. This material forms the pores (average effective diameter of 0.5 μm) through which fluid flows.

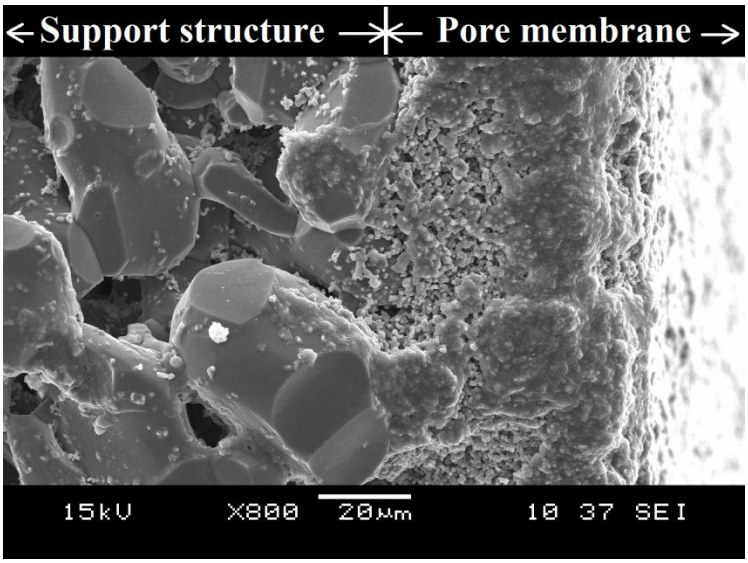

Figure 3.1 - Microfilter Support and Pore Membrane

Wentz, et al. [28] revealed membrane pore and surface structure by destructively impacting the material with a hammer. This resulted in detailed images of the microstructure, as shown in Fig. 3.2(a), but consecutive layers beneath a location of interest were unobtainable using this approach.

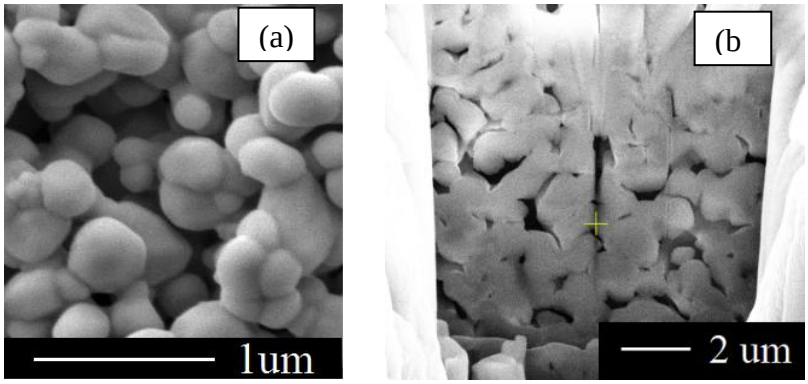

Figure 3.2 - Alumina Microfilter Prepared by Hammer Impact (a); and FIB (b)

Here, a focused ion beam (FIB) (*Strata DB 235*, FEI Company, Hillsboro, OR) was utilized to obtain detailed pore features. The FIB removes material by ionizing the substrate, much like a grinding process. However alumina, as a non-conductive material, does not dissipate charge buildup well during the material removal process. This hinders the viewing and cutting process. However, Inkson, et al. [42] imaged bulk alumina successfully with the FIB after applications of metallic coatings. Gold was coated on the alumina microfilter surface to enable charge transference from the ion impact site. Samples were pumped to vacuum pressure less than 8.8e-6 mbar and viewed upon with a 15 kV electron beam. An alumina layer revealed with the FIB is shown in Fig. 3.2(b). Material layers were removed in the amount of 0.5 µm in a direction deeper into the membrane to attain consecutive layers—see Fig. 3.3—for imaging. Layer dimensions were width 10.00 µm, length 0.60 µm, and depth 10.00 µm.

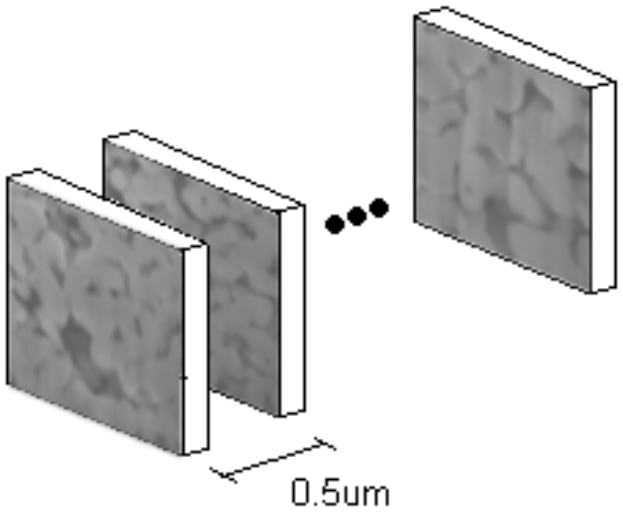

Figure 3.3 - Successive Membrane Slices

3.2.2 Tortuous Geometry Recreation

Images of successive FIB-sliced layers were adjusted to match features extant on multiple layers upon layer stacking. Matched features ensured that upon three-dimensional reconstruction, pores existing in one layer passed smoothly to adjacent layers. In this section, the reconstruction of a three-dimensional geometry from FIB slices and its advantages over geometries from previous works are discussed.

Feature and Edge Matching

There are two types of features that dictate how the layers stack and in what position and orientation: (1) a pore with a distinct geometry in two layers signifies that the pore started or continued from the present layer and continued or ended on the next layer; (2) a distinct membrane geometry in only found on certain layers signifies that the membrane material had not emerged on the present layer but became extant in the next layer. Identifier 1 is seen in Figs. 3.4a-b and Identifier 2 in Figs. 3.4c-d.

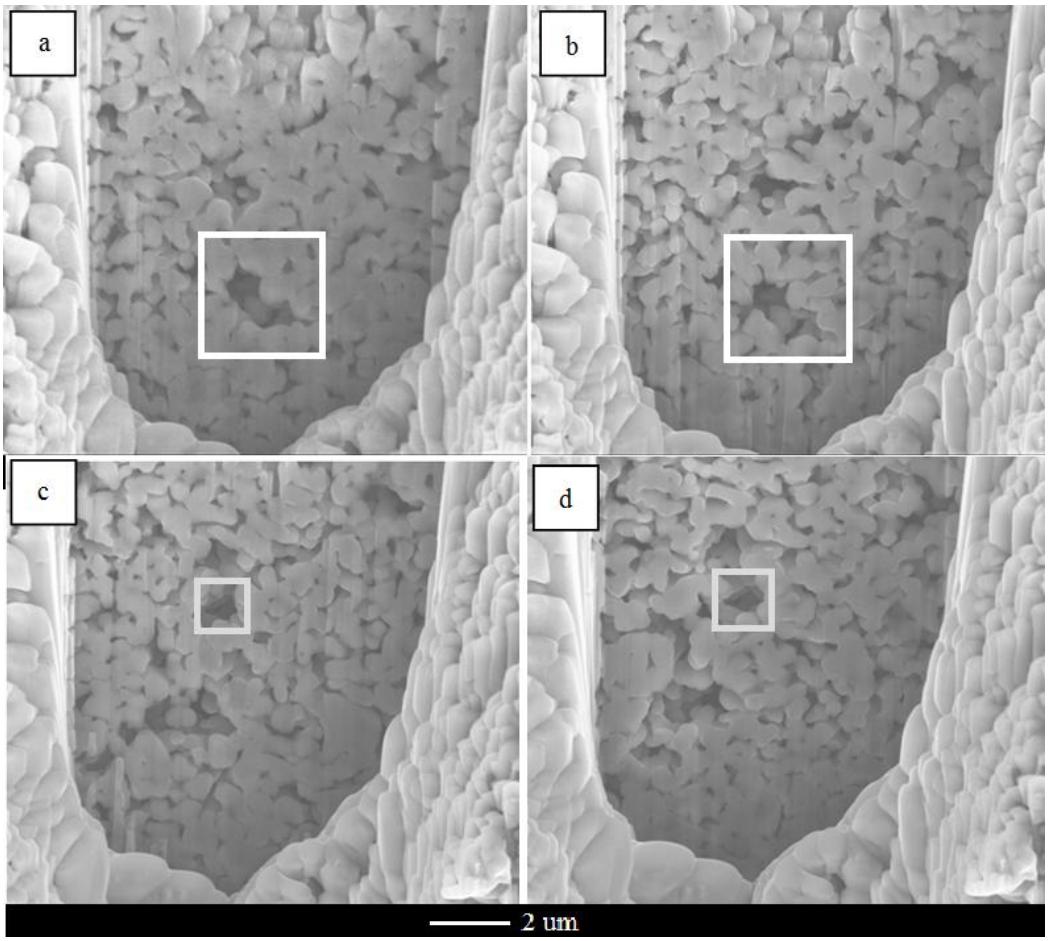

Figure 3.4 - Layer Images and Similar Geometric Features Extant Amongst Each (Shaded Rectangles)

The alumina membrane is approximated by spheres, as this membrane initially consisted of microscale alumina spheres that are superheated and sintered together. For one layer, the membrane surface area is approximated by circles as this geometry grasps the most flexibility in edge curvature to match the FIB-obtained geometry of the material. Intersecting circles approximate the fused mating surfaces and their x-, y-, z-locations, and the radii of the circles were recorded. Figure 3.5 shows the similarity of a circle-approximated layer (a) compared to its FIB image complement (b).

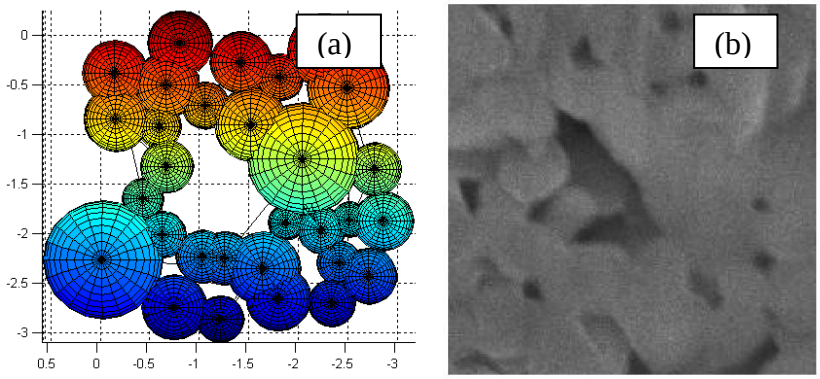

Figure 3.5 - Comparison of a Layer Recreated with Spheres (a) and Image from the FIB (b)

The circle-approximation procedure is applied to each consecutive layer. With the circle positions of each layer and the distance between layers known, reconstruction can begin. Circles on each layer were replaced with spheres and each layer was then combined 0.5 µm apart to form a three-dimensional representation of the tortuous pore and membrane material. Single and multiple layer combinations can be seen in Fig. 3.6. A material transition exists between layers because membrane particle sizes are large enough to intersect spheres from other layers and bridge the 0.5 µm layer-layer gap.

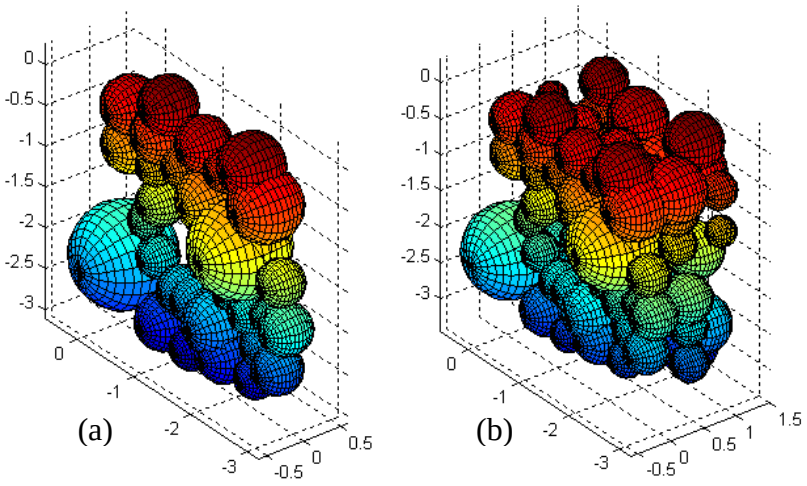

Figure 3.6 - (a) One Layer and (B) Three Layers of Spherical Structure; units in µm

Volume Recreation

The microfilter membrane geometry in Fig. 3.6(c) is subtracted from a rectangular prism to form a negative of the volume. This generated a space that represented the flowable volume for the fluid. This space is a faithful representation of the actual microfilter membrane and therefore has many advantages over geometries employed in previous works. These advantages are: (1) the geometry is three-dimensional enabling more degrees of freedom in particle movement than two-dimensional simulation; (2) the ability to show partial blocking since complex geometry pores are difficult to be completely blocked by spherical particles that become trapped; (3) the pores are tortuous and their cross-sectional areas change in shape and size throughout their paths allowing particles to be trapped in many locations instead of just in pre-determined locations; (4) the ability to visualize and predict particles agglomerating on the membrane surface.

Concerns for unsteady-state particle flow and scarcity in starting locations were alleviated by adding flow volume (referred to later as the *bulk flow region*) above the surface leading into

the pores. The added volume and the tortuous negative volume are then meshed in the software GAMBIT (ANSYS, Inc., Canonsburg, PA). Compared to a standard geometry, the tortuosity of this volume creates locations where features are small and difficult to mesh. Size functions, which alter volume element size as a function of distance from a location of interest, are implemented to alleviate this issue. The final mesh, seen in Fig. 3.7, is imported into FLUENT (ANSYS, Inc.) for fluid flow and particle simulation. The top (blue) areas represent velocity inlets and the bottom (red) areas represent pressure outlets.

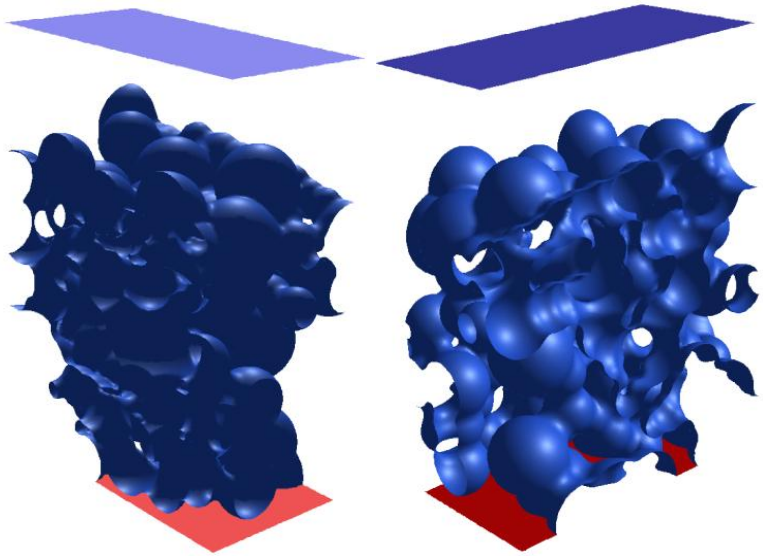

Figure 3.7 - Isometric Views of the Three-Dimensional Mesh

3.3 Fluid Dynamic Model Development

The fluid flow through a tortuous three-dimensional volume is modeled, as in [15, 28], by solving the Navier-Stokes equations with steady-state incompressible flow in the absence of gravity terms. Fouling of the tortuous geometry is modeled though injected particles

becoming trapped in the membrane. The particle movement is calculated by numerical integration of the Langevin equation [29] with applied electrostatic forces and Brownian motion. Particle trajectories are also affected by collision with walls and other particles. The electrostatic and Brownian motion forces, and the collision models are discussed in the following subsections.

3.3.1 Electrostatic and Brownian Motion Forces

The electrostatics imposed on the injected particles significantly change the trajectory when a particle is injected into the flow and nears other trapped particles. Kim et al. [8] showed that particles may or may not enter a pore depending on its electrostatic force. Ham et al. [3] furthered this research and found that trajectories significantly change with the onset of electrostatic forces. This force causes particles to deviate from their paths and can be a deciding factor whether a particle traps in or escapes a pore.

If the Knudsen number is near or greater than unity, the continuum assumption of particle movement does not hold as a good approximation—discrete particle effects exist [39]. The Knudsen number is a non-dimensional number defined as the ratio of the fluid mean free path and the particle characteristic length,

$$Kn = \frac{\lambda}{D}, \tag{3.1}$$

where λ is the mean-free path and D is the particle diameter. Diameters of the injected particles range from 25 nm to 500 nm causing the Knudsen number to range between 0.5 and

5. The magnitudes of these Knudsen numbers therefore allow particles to be affected by discrete effects, nullifying the continuum approximation of particle movement. The discrete effects are modeled by Brownian motion, the random walk of the bulk particle caused by forces from fluid particles.

Brownian motion, in sub-micron-scales, can be seen as a "jiggling" motion in space. At macro-scales, the bulk particle deviates slightly from its prescribed pathline due to the random walk and may slightly or significantly move off course. More importantly, a deviation of movement can cause the particle to evade the possibility of becoming trapped for one or more time steps. The impact of Brownian motion, as the breakdown of the continuum assumption for particle movement, is evident in the work of Ham et al. [3] where approximately twice as many particles were needed to block the flow after the inclusion of discrete forces.

3.3.2 Wall Collision Model

MWF particles in fluids are subject to collisions with walls as they flow through the membrane pore structure. In previous models [3, 13, 15], post-collision movement was modeled as a mechanism isolating the particle at the wall, causing it to roll along the curvature of the microfilter.

These models do not describe the complete collision physics on particle trajectory. Instead, it is likely that the particle will rebound off the wall into the fluid stream before being recaptured by fluid forces. This is because: (1) the momentum of the particle is conserved

and its impulse after collision imparts a surface-departing velocity; and (2) varying boundary layer fluid velocities cause a larger force onto the non-collision surface than the collision surface thereby imparting both a surface-directed velocity and a moment on the particle. This combination of surface-departing velocity, from (1), and surface-directing velocity, from (2), isolates the particle at the membrane surface; the moment, from (2), causes particle rotation, thereby rolling the particle along the surface curvature. This section details the reflection mechanism, aspect (1), prior to fluid force impartation.

A MWF particle travels in a continuous trajectory until the trajectory is altered by a physical object such as a wall. A wall can either be the microfilter membrane or a previously trapped particle surface. Take note that walls can be denoted as *faces* as this is the proper terminology for finite elements used in this simulation—terminology depictions can be seen in Fig. 3.8.

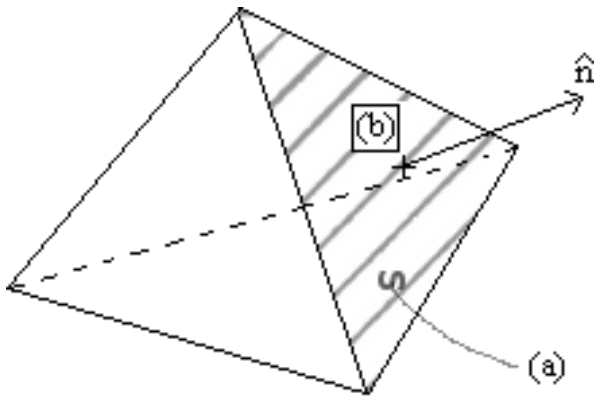

Figure 3.8 - Depiction of Triangular Face (a) and Face Centroid (b) on this Tetragonal Cell. Face Normal Depicted with $\hat{n}$

When a face centroid is encountered to be less than a radius distance away from the particle centroid, the particle reflects in a direction according to specular reflection (Fig. 3.9),

$$\Delta\vec{v} = -(1+\alpha)(\vec{v}_0 \cdot \hat{n})\hat{n}, \tag{3.2}$$

where $\Delta\vec{v}$ is the change in the velocity of the particle, α is the coefficient of restitution, $\vec{v}_0$ is the incident velocity vector, and $\hat{n}$ is the vector normal of the collision surface.

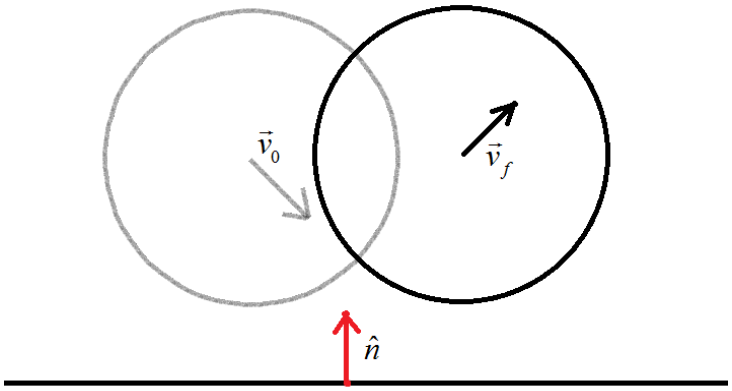

Figure 3.9 - Specular Reflection for Particles

The change in velocity is then accounted for in the velocity in the succeeding time step, viz.,

$$\vec{v}_f = \vec{v}_0 + \Delta\vec{v}, \tag{3.3}$$

where $\vec{v}_f$ is the resultant velocity vector. The position of the particle in the succeeding time step is also calculated,

$$\vec{x}_f = \vec{x}_0 + \vec{v}_f \Delta t, \tag{3.4}$$

where $\vec{x}_f$ is the post-collision position, $\vec{x}_0$ is the pre-collision position, and Δt is the time step.

The post-collision position and the resultant velocity, as calculated from Eqns. 3.3 and 3.4, are set as the positions and velocities for the succeeding time step. In that time step, the particle receives forces from hydrodynamics, electrostatics, and Brownian motion. Its position and velocity is then updated accordingly. This model operates in four steps:

1. Select a face and determine the distance between the face centroid and the particle centroid.
    a. If the distance is less than the particle radius, mark collision; continue to Step 2.
    b. Else, no collision; restart at Step 1.
2. Taking the face of closest distance, consider the particle incident velocity so that:
    a. If particle is moving away from face, no collision possible; repeat Step 2 with the next closest face.
    b. Else, continue to Step 3.
3. Particle is approaching the face. Calculate resultant velocity vector from Eqn. 3.3.
4. Update position and velocity for the succeeding time step. Calculate the values for and the effect of the hydrodynamic and electrostatic forces and Brownian motion. Start wall collision algorithm on the succeeding time step with Step 1.

Step 1 is used to find all faces within collision distance, i.e., all faces where the distance between their centroids and the particle centroid is less than the radius of the particle. The

reflection algorithm is not run on faces that are beyond a radius distance, as these faces have no effect on reflection.

First, define the set of all faces in the geometry as *F*, so that there are *a* faces in *F*. The distance d_j between the centroid of face F_j and the particle position is calculated as,

$$d_j = \sqrt{\left(x_p - x_j\right)^2 + \left(y_p - y_j\right)^2 + \left(z_p - z_j\right)^2} \quad \text{for } j = 1, 2, ..., a, \tag{3.5}$$

where x_p, y_p, and z_p are the x-, y-, and z-position, respectively, of the particle and x_j, y_j, and z_j are x-, y-, and z-position, respectively, of the centroid of the *j*-th face. If the distance d_j is less than radius of the particle (r_p), then a collision is detected. An array (or subset, *S*) of all collided faces F_s, from all existing faces, is established as

$$S = \left\{ F_j \;\middle|\; d_j \le r_p \right.$$
$$F_s \in S \quad \text{for } s = 1, 2, ...b, \quad b \le a. \tag{3.6}$$

There are *b* faces in subset *S*.

Steps 2 and 3 do not establish collision analysis for faces that exist in the radius distance, but cannot be collided with the particle if the particle is moving away from the face. Collidability was found by examining the angle (θ_s) between the particle velocity and the wall normal vector:

$$\theta_s = \cos^{-1}\left(\hat{v}_0 \cdot \hat{n}_s\right), \tag{3.7}$$

where $\hat{v}_0$ is the particle normalized incident velocity vector and $\hat{n}_s$ is the normalized face normal vector. θ_s, in degrees, ranges from 0°: where the particle is moving in the same direction as the face normal vector (no collision); to 180°: where the particle is moving the opposite direction as the face normal vector (collision). Faces that satisfy a collision scenario F_t form the final array (or subset *T*) of collidable faces, from all existing faces,

$$\begin{aligned} &T = \{\, F_s \mid \theta_s < 90° \\ &F_t \in T \quad \text{for } t = 1, 2, ...c, \quad c \le b. \end{aligned} \tag{3.8}$$

There are *c* faces in subset *T*.

Lastly, to solve the issue of multiple face collisions, it is ensured that one and only one face is analyzed for reflection. One face, the closest face to the particle F_{min} has the index *min* and is determined from the face set of collidable faces, *T*, through,

$$d_{min} = \min(d_t). \tag{3.9}$$

The final velocity can now be calculated (Step 4), with reference from Eqns. 3.2 and 3.3, as:

$$\vec{v}_f = \begin{cases} \vec{v}_0 & 0° \le \theta_{min} < 90° \\ \vec{v}_0 - (1+\alpha)(\hat{v}_0 \cdot \hat{n}_{min})\hat{n}_{min} & 90° \le \theta_{min} \le 180°, \end{cases} \tag{3.10}$$

where $\hat{n}_{min}$ and θ_{min} are determined based off d_{min}.

In summary, this wall collision model determines that the particle collided with the closest collidable face F_{min} at a centroid-to-centroid distance of d_{min}. The resultant velocity $\vec{v}_f$ of

the particle is calculated from Eqn. 3.10 with influence from the incident velocity $\vec{v}_0$, the normalized face normal $\hat{n}_{min}$, and the coefficient of restitution α.

3.3.3 Particle Trapping Model

It can be visually recognized when a particle has become trapped in two dimensions [3, 8, 13, 14]. However, the disposition of a particle is difficult to judge in three dimensions due to the tortuous nature of the pore path and the poor distinguishability between particle and membrane mesh. Therefore, the wall collision model serves a dual purpose—not only used for the aforementioned wall collision scenarios, but also is paramount in determining when a particle has become trapped.

Being trapped is realized quantitatively when location of a particle remains the same for consecutive time steps or suffers repeated wall collisions that isolate its position in the same location. The particle trapping model activates after Step 3 but before Step 4 (i.e., before the succeeding time step) of the wall reflection model.

Particle trapping is determined by calculating the moving average of the particle position and finding the difference between the current position of the particle and the moving average. The positional moving average M_i of a time step number, *i*, is determined by the average of the current position of the particle P_i and the positional moving average for the previous time step M_{i-1},

$$M_i = \frac{\left(P_i + M_{i-1}\right)}{2}. \tag{3.11}$$

where M_0, the starting value of the positional moving average, equals P_1.

The positional moving average is used to determine how far or close the current position of a particle is in relation to its average position over time. The distance difference D_i is the distance between the current position of the particle and the positional moving average. This is defined as:

$$D_i = \left|P_i - M_i\right|. \tag{3.12}$$

The distance difference depicts the spread of the particle to the moving average. The spread can then be put into relative terms by taking its ratio with a characteristic length L

$$R_i = \frac{D_i}{L}. \tag{3.13}$$

Here, the characteristic length is based upon the maximum distance difference obtained through the life of the simulation.

If the ratio of the distance difference versus a characteristic length is consecutively less than 5% of the particle movement over multiple time steps, the particle is trapped. This is seen conceptualized as a particle remaining at the same position, due to any combination of hydrodynamic, electrostatic, stochastic, or wall collision forces.

3.4 Fluid Flow and Particle Simulation

This section details the fluid flow and particle simulation in a three-dimensional tortuous mesh. Furthermore, particle diameter determination is discussed, as well as the fluid dynamics simulation methodology for this research. The flux decline model is then discussed and the resulting fouling mechanisms are presented.

3.4.1 Simulation Methodology and Design

The three-dimensional tortuous pore geometry was obtained from FIB cross-sectional slices of a microfilter recombined, meshed, and prepared for simulation. The Navier-Stokes equations of fluid motion were solved using the commercial software package FLUENT. MWF colloids, imitated by particles, are injected into the fluid and simulated until trapped to resemble particle movement and fouling. The metrics guiding the injected particles are a size and entry location distribution.

Wentz et al. [13] showed particle size distribution varying as a function of filtration time. Therefore, the particle sizes are based on the particle size distributions at 2000 minutes of filtration of Castrol Clearedge 6519, a semi-synthetic MWF. Beginning the simulation at this time of use of the MWF ensures that particles that enter the stream are of size to block the pores. The limiting size is 125 nm as particles smaller than 125 nm commonly pass through the system. Particle diameters, *x*, were determined randomly from a size probability density function *f(x)* per Wentz et al. [13],

$$f(x) = 0.0137 - 2.384 \cdot 10^{-5}x \quad for \quad (125 \leq x \leq 550). \tag{3.14}$$

The flow profile and the path of an escaped particle can be seen in Fig. 3.10. Moreover, the difficulty in ascertaining particle disposition is evident as many flow lines, mesh lines, and complex membrane geometries prevent identification of constricting pores as typically done in two dimensions.

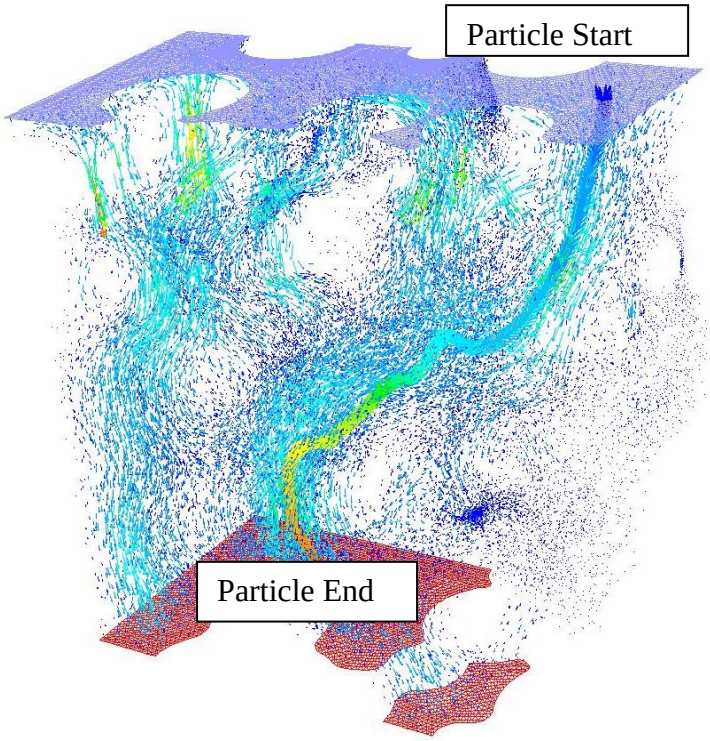

Figure 3.10 - Flow Velocity Profile and Particle Trajectory from the Velocity Inlet to the Pressure Outlet

The particles are injected from a random location on the velocity inlet area. The particles then travel through the tortuous pore structure and either escape through the pressure outlet or become trapped between walls. The entire fluid and particle simulation method occurs in three steps:

1. Simulate the continuous phase velocity flow field within the pore area.
2. Simulate the injection of a randomly selected particle size and location, and evaluate the particle trajectory. The particle trapping model is utilized to evaluate the disposition of the particle.
    a. If the particle is trapped, continue.
    b. Else, the particle escaped; repeat Step 2 with a new particle.
3. Remove the cells that compose the volume of the trapped particle and set the removed volume boundary as a wall.

This entire process simulates one injected particle, determined its fate, and removed its volume from the fluid region. The volume removal procedure in Step 3 produces two results: (1) walls are created at the surface of the trapped particle, setting more locations where particles may collide; (2) fluid flow region is reduced due to volume removal, thereby reducing the effective area of the tortuous pores and reducing the flow rate.

Figure 3.11 has been created to illustrate how particles travel from the inlet to the outlet. Upon injection at the inlet, particles travel through the *bulk flow region* before entering a pore. This region allows particles to come to steady movement after being injected. Then, particles enter the tortuous *pore region*. If the particles are able to pass through the tortuous pore region, they exit at the outlet. The particles have one of two behaviors: (1) enter the pores; or (2) stop at or above the interface of the two regions. It is therefore useful to define a **penetration depth** *D* initiating at zero at the interface showing how deep a particle traveled into the pore before becoming trapped. Positive penetration depth means that a particle has completely passed through the bulk flow region and has entered the pore region. Negative penetration depth means that the particle has not passed nor entered a tortuous pore. Rather,

its trapped location resides above the pores in the bulk flow region. The penetration depth will be used later in the interpretation of the fouling mechanisms.

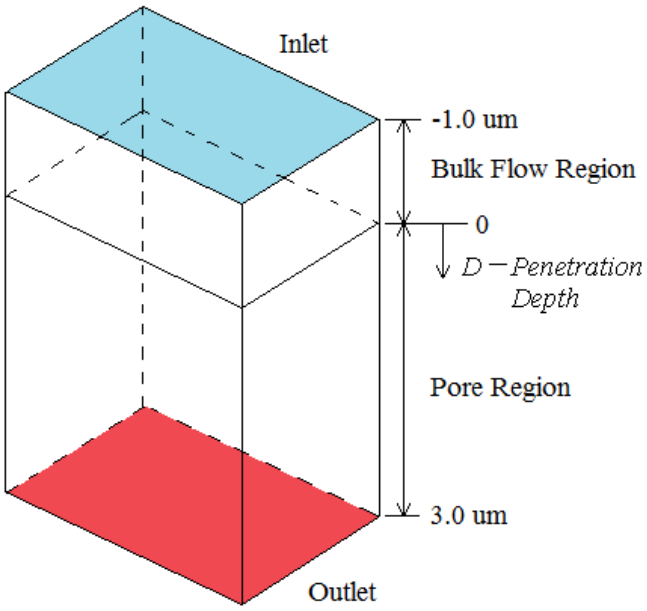

Figure 3.11 - Schematic of the *Penetration Depth* with the Bulk Flow Region and the Pore Region

Particles were injected from the velocity inlet into the three-dimensional tortuous pore geometry one by one, one after the other. That is, a particle was not injected until the disposition of the previous particle was known and recorded. A particle can achieve *trapped* status if its position is the same after consecutive time steps; it achieves *escaped* status if it leaves through the pressure outlet. The result of this process for two trapped particles can be seen in Fig. 3.12. The three-step particle injection procedure is repeated as many times as necessary until the flux reaches steady state or the bulk flow region is completely full of particles.

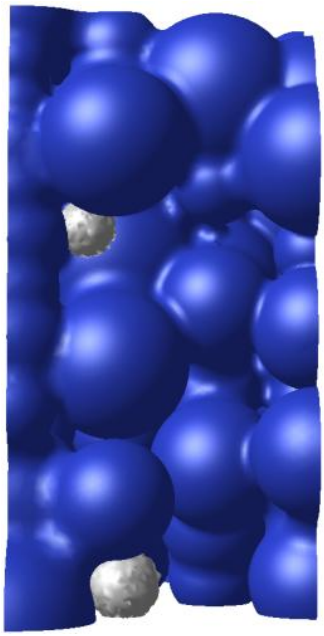

Figure 3.12 - Two Trapped Particles (light) in a Tortuous Membrane (dark)

For these simulations, the microemulsions have a potential of -50 mV from ζ-potential measurements using laser Doppler electrophoresis. The membrane surface has a ζ-potential of 0 mV due to electrostatic similarity to the MWF pH [3]. Although we recognize the membrane can attain a non-zero charge, in this initial study we assume no charge.

3.4.2 Simulation Results and Discussion

Particles are trapped within the tortuous pore paths causing fluid flux decline. Furthermore, the disposition of certain particles has a significant impact on the dispositions of future particles and on the modes of fouling. In this section, the flux decline and fouling modes from the particle simulations are presented and discussed.

Flux Decline

Flow through the model was calculated by examining the effective flow area of numerous parallel cross sections of a simulation and finding the minimum area. Since the flow material is liquid and incompressible, the minimum effective cross-sectional flow area A_{min} regulates how much volumetric flow $\dot{V}$ can pass,

$$\dot{V} = A_{min} v_{inlet}, \tag{3.15}$$

where v_{inlet} is the inlet velocity. As particles become trapped, effective cross-sectional flow areas shrink, with some shrinking faster than others. The faster shrinking areas become the areas limiting the volumetric flow.

The flow rate of the geometry is 3.25e-10 liters per hour at the start of the simulation. After 48 particles, the flow became steady state and 2.41e-10 liters per hour; a 27% decrease. Simulation ended at 48 particles as continued injection led to immediate blocking at the membrane surface by the congregation of particles filling the bulk flow region. Fig. 3.13 shows the flux decline over the life of the simulation. Fig. 3.14 provides the visualization of the particles that became trapped. Although flow does have a minor decrease prior to the end of the simulation, additional injected particles past Particle 48 did not have a significant impact on flux decline due to how the particles were stacked in the bulk flow region. Particles resting upon one another were not able to affect the established minimum cross-sectional area of the pores. Due to this, the flow rate was not significantly affected.

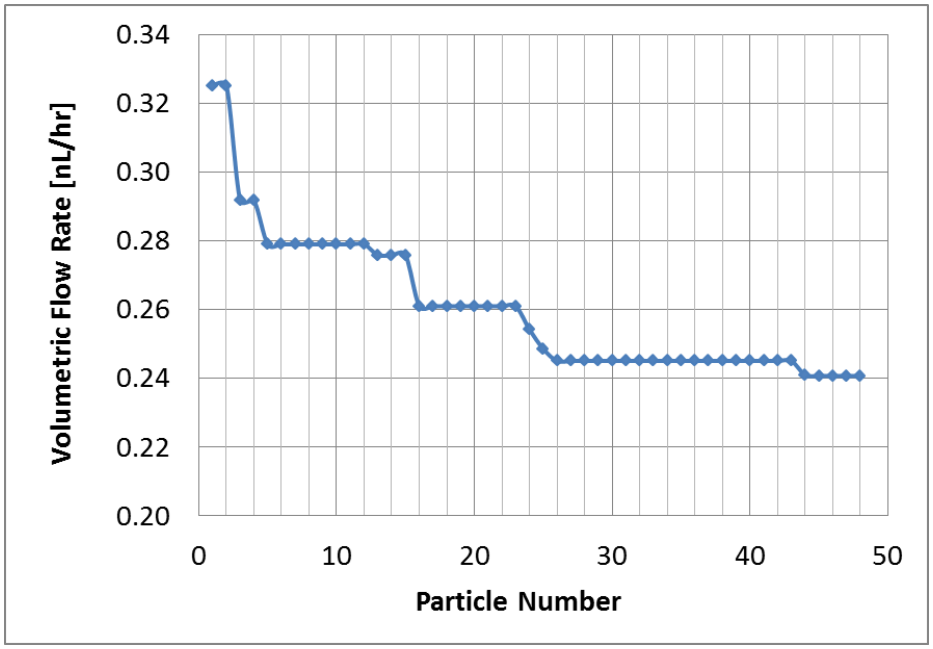

Figure 3.13 - Volumetric Flow Rate Decreases with Number Of Particles

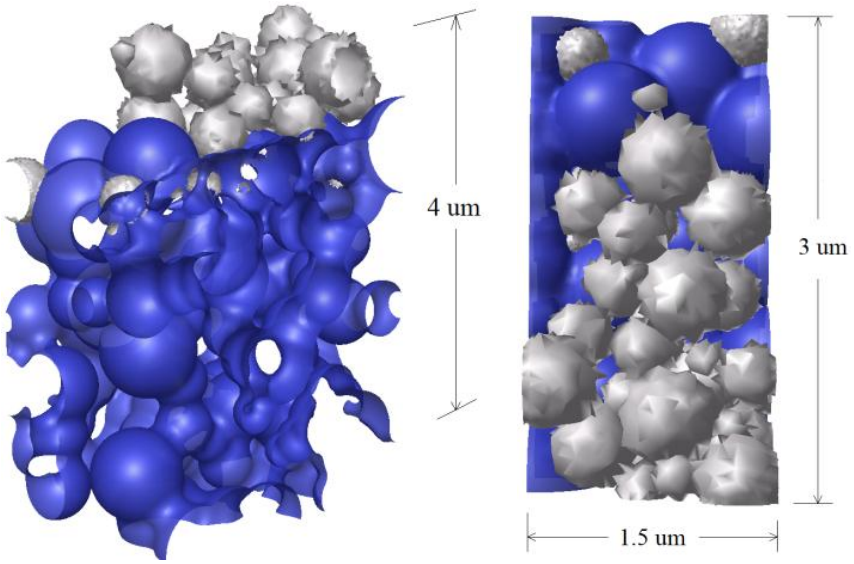

Figure 3.14 - Isometric/Top View of the Trapped Particles (light) and the Membrane (dark)

It is important to note that in Fig. 3.13 the flux decline profile reaches a non-zero steady state as in experimental results from [1, 4]. Also, this simulation shows that spherical particles do

not allow a complete sealing of the inlet flow as in [15]. However, the injection of more particles into the flow causes blockage at the crevices of the existing trapped particles thereby reducing the flux as shown in the flux decline results.

Fig. 3.13 also shows that flux initially decreases sharply and then transitions to steady state. This is also similar to experimental results from [4] and [1]. This flow response is caused by one particle trapping in a significantly sized pore and initiating surface fouling. This behavior is realized towards the beginning of the simulation at Particle 3. The particle causes flow to drop substantially as a major pore has become blocked. This is because pore obstructions cause the effective flow area to decrease and thereby the flow rate to decrease.

Fouling by Cake Layer

Results from this simulation are shown in Fig. 3.15. The scale of -1.0 to 3.0 is maintained to emphasize that particles are mostly deposited in the pore entrance region and bulk flow area, not deposited in the rest of the membrane. Particles 1 to 10, at the start of the simulation, have positive penetration depth (recall Fig. 3.11) and show blocking within the pores. Injections after Particle 4 are shown to be less deep than Particle 4. This reveals that although particles can still enter other pores, once a major pore is partially blocked, particle stacking ensues nearby the blocked pore leading to further restriction of partially blocked pore and the formation of cake layers. Moreover, after Particle 13, a majority of particles injected have zero or negative penetration depth. Here, particles stack at the pore inlets and are unable to travel deeper. Succeeding particles then accumulate at the inlets and grow into the bulk flow

region. This further suggests that once particles are trapped, succeeding particles begin stacking. This resembles the fouling method called caking.

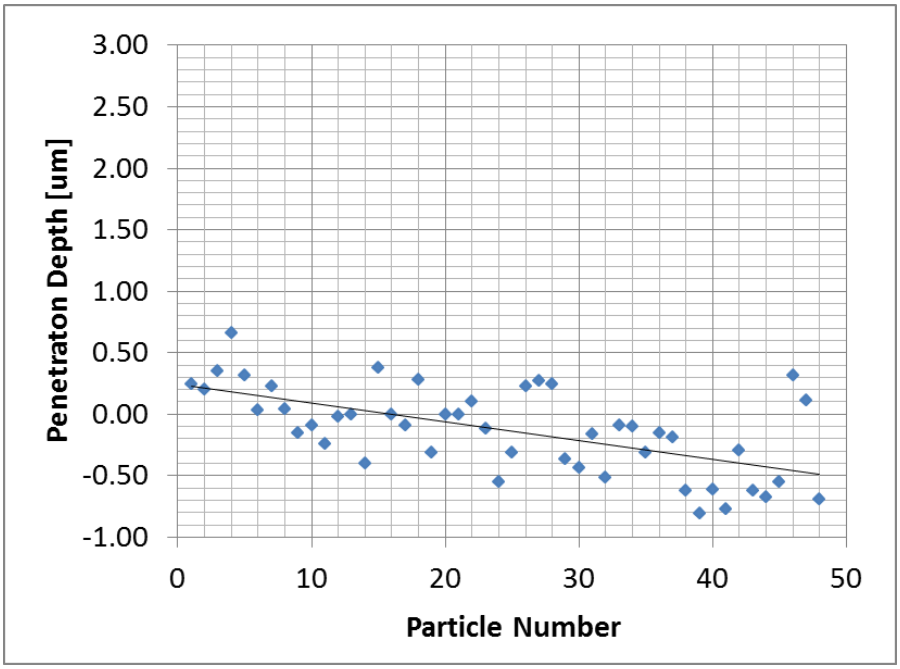

Figure 3.15 - Relationship between Penetration Depth and Injected Number of Particles

Fouling by cake layer was examined comprehensively by the microfiltration review done by Belfort et al. [5]. Their review highlighted the significant problem of cake layer development in many applications and feed fluids. Specifically, this fouling mechanism was discussed by Skerlos et al. [6] where the filtration of synthetic MWF defoamers in absence of lubricants formed a cake layer; and likewise in [21] where the end-result of filtering semi-synthetic fluids resulted in cake layer formation as seen in Fig. 3.16.

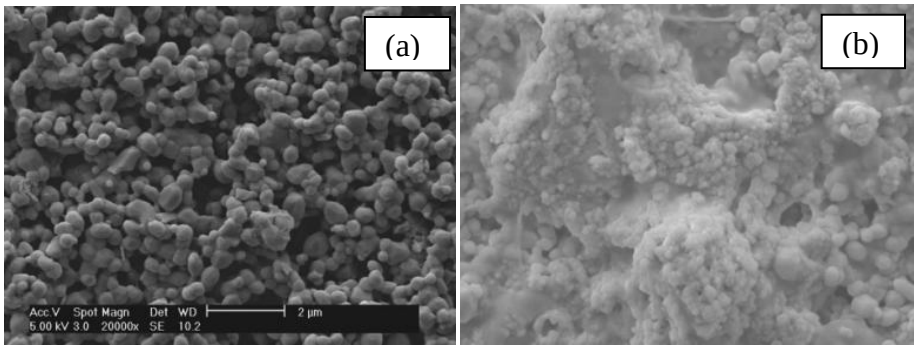

Figure 3.16 - SEM Images of a Clean Microfilter (a) and a Developed Cake Layer (b) [13]

In an effort to simulate and visualize fouling mechanisms, Wentz et al. [13] fashioned a tortuous two-dimensional model showing partial pore blocking. However, the caking fouling mechanism was unseen. The multi-layer three-dimensional simulations by Ham et al. [15] alluded to cake layer formation from significant partial pore blocking on layers closer to the velocity inlet than layers elsewhere.

Figure 3.15 clearly shows that penetration depth has a decreasing linear trend versus the number of particles injected. This is not unexpected as the model does not consider the effect of cross-flow on the cake layer.

Even though pores are on average larger than the diameters of particles injected, particles become trapped primarily due to partial pore blocking and particle-particle stacking internal to the pores and cake layer formation external to the pores thereafter. This is different than previous work showing particles being trapped at all depths of pore constrictions [15, 28], instead of primarily on the upmost layer.

Caking behavior is attributed to the particle trapping model as it is through the wall collision model that particles can become trapped in *any* location instead of just certain pore

restrictions. Without the particle trapping model, the simulation would have been completed when all pores were blocked. This would not have shown any cake layer buildup. However in this research, upon a pore becoming partially blocked, injected particles continued to stack in non-pore locations resulting in an emergent cake layer.

It may be noted that caking, as a mode of fouling, is highly susceptible to surfactant flushing or backpulsing as the cake layer residing at the filtration surface would be dislodged from the surface and flux would have regained its original value, similar to [4]. Moreover, a pressure change such as that obtained from backpulsing could have dislodging effects on the cake layer similar to the scenario of increasing flow from pressure relaxation [6].

3.5 Effect of Particle Size Distribution on Flux Decline

Particle size distributions for different ages of MWF were established in [13]. This section details a parametric study of the simulation of microfilter fouling due to alternative size distributions.

3.5.1 Design of Parametric Study Experiments

The parameter of change in this parametric study is the age of the MWF. Three values for the age of the MWF exist: *used, semi-used,* and *new*. The age of the MWF is represented by the particle size distributions, based on Castrol Clearedge 6519. The input settings and results of the *semi-used* and *new* MWFs are discussed here; the *used* MWF has been covered in Section

3.4.2. The *semi-used* and *new* MWFs have particle size distributions determined at 900 minutes and 180 minutes of filtration [13], respectively. These distributions were also linearized into probability density functions. These functions, along with the MWF class and particle size ranges are listed in Table 3.1. Note that the high range of the diameters increases due to particle aggregation.

Table 3.1 - Governing Equations and Statistics for Particles Sizes

MWF class	Time of use [min]	Particle diameter probability density function	Particle diameter range [nm]
Used	2000	$f(x) = 0.0137 - 2.384 \times 10^{-5} x$ for $(125 \leq x \leq 550)$	125 to 550
Semi-used	900	$f(x) = 0.0549 - 1.220 \times 10^{-4} x$ for $(50 \leq x \leq 450)$	50 to 450
New	180	$f(x) = 0.1191 - 4.760 \times 10^{-4} x$ for $(50 \leq x \leq 250)$	50 to 250

New MWF is considered as fluid that is relatively unused; it has not been used for more than 200 minutes in system filtration. The majority of particles in this class can pass through a majority of the pores due to their diameter being smaller than the average 500 nm pore diameter. *Semi-used* fluid is considered fluid that has been slightly used. The particles in this class can pass through microfiltration material, however a fraction of particles do block pores. *Used* fluid is considered fluid that that has been used for a long time. The particles in this class can also pass through microfiltration material, but significantly more particles than the *semi-used* MWF are larger and block the pores.

3.5.2 Parametric Study Results and Discussion

The parametric study considers three particle size distributions for simulation and includes the *used* case as discussed in Section 3.4.2. The resulting flux decline profiles, trapped particle visualizations, and penetration depth profiles are discussed in this section.

Flux Decline Profiles

The flux decline profiles reveal the reduction in performance of the microfilter. The profiles for the *semi-used* and *new* MWFs are displayed in Figs. 3.17 and 3.18.

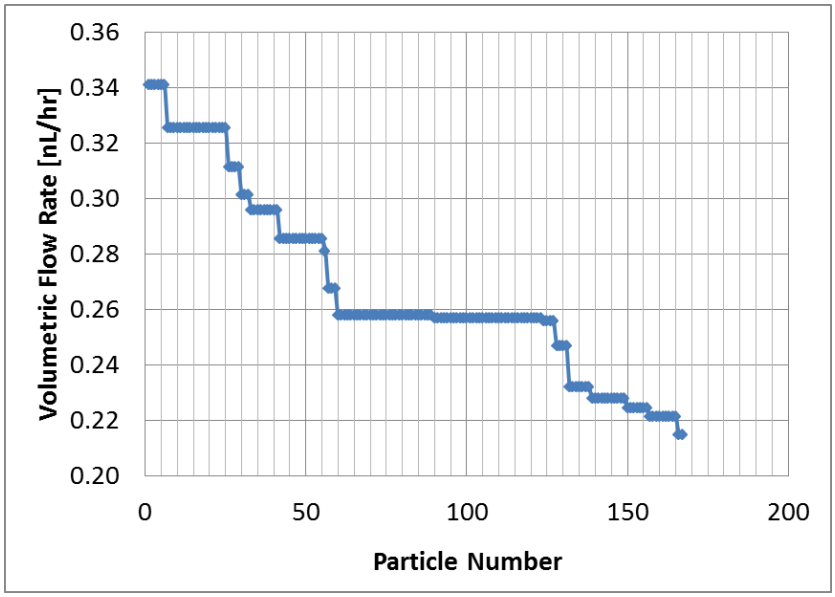

Figure 3.17 - Flux Decline for S*emi-used* MWF

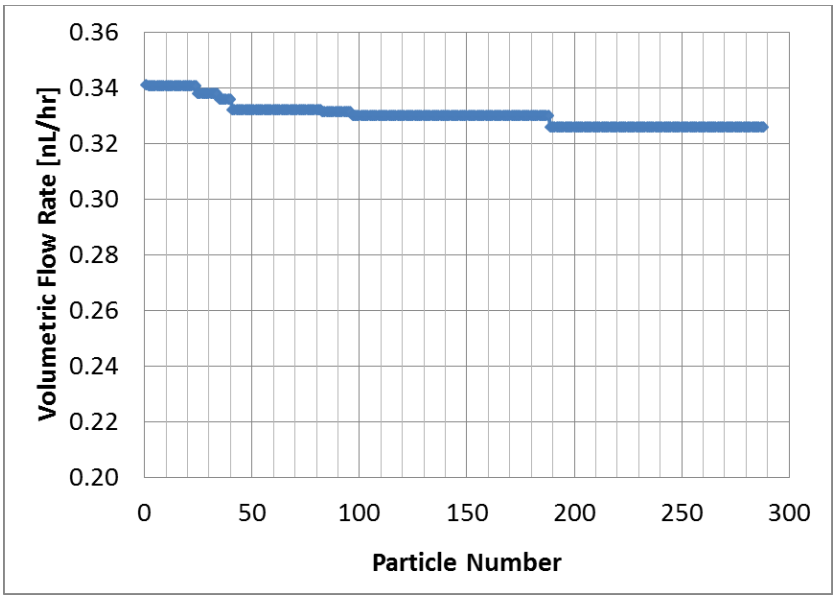

Figure 3.18 - Flux Decline for *New* MWF

Simulation for the *semi-used* MWF ended at 167 particles due to a buildup of particles in the bulk flow region (Fig. 3.17). The simulation exhibited a linearly decreasing flux at the start of the simulation, steady state flux at the middle, and continued decreasing flux towards the end. Over the life of this simulation, there is a 37% decrease in flux compared to initial value. The simulation for the *new* MWF ended at 288 particles due to unending and consistent particle escape (Fig. 3.18)—continued injections only led to predictable linear decrease, and a conclusive sign for ending the simulation would require a prohibitively large number of particles. Over the life of this simulation, there is a 4.5% decrease in flux compared to initial value.

The *semi-used* flux decline profile decreases linearly at the start of the simulation, trending to quasi-steady state, and finally declining again. The quasi-steady state exists because as particles are injected from the velocity inlet, the majority of particles stack in the center of system at a penetration depth near 0; this is visible in simulation visualizations (Fig. 3.19)

and later sections. Injected particles that collide with the large stacked column in the middle become trapped near the middle. This does not change flux decline as it does not change the smallest effective area.

However, as the middle cannot sustain more particles any higher, the particles settle around it, filling in locations not occupied with particles, increasing the volume occupied by particles and reducing the effective flow area. This reduction causes a decrease in flux according to Eqn. 3.15.

The *new* MWF profile also exhibits a continuous linear decrease in flux throughout the simulation; heavy at the start and light thereafter. The first 50 injected particles have three trapped particles compared to three trapped particles in the rest of the simulation (237 injected particles). The rate of particle trapping is much higher at the start of the simulation than after (6% versus 1.3%). This difference in trapping percentage suggests that small pores at the start of the simulation are blocked first, leaving the large pores unblocked for particles to flow through.

The results from the comparison of *used, semi-used,* and *new* flux decline profiles reveal that older MWFs trends to steady state faster because they fill the flow volume faster. The *new* MWF fills up the flow volume slower and it takes more particles to attain a significant decrease to its effective area and flux profile.

Trapped Particle Visualizations

The visualizations showing trapped particles and blocked membrane are in Figs. 3.19 and 3.20. These aid in determining which fouling mechanism is at work.

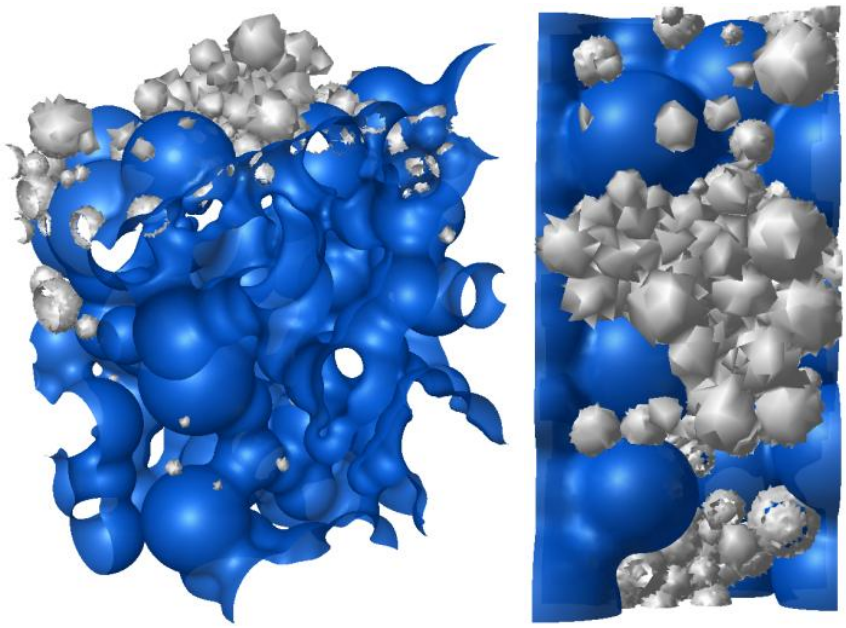

Figure 3.19 - Isometric/Top View of the Trapped Particles (light) and the Membrane (dark) in a *Semi-used* MWF

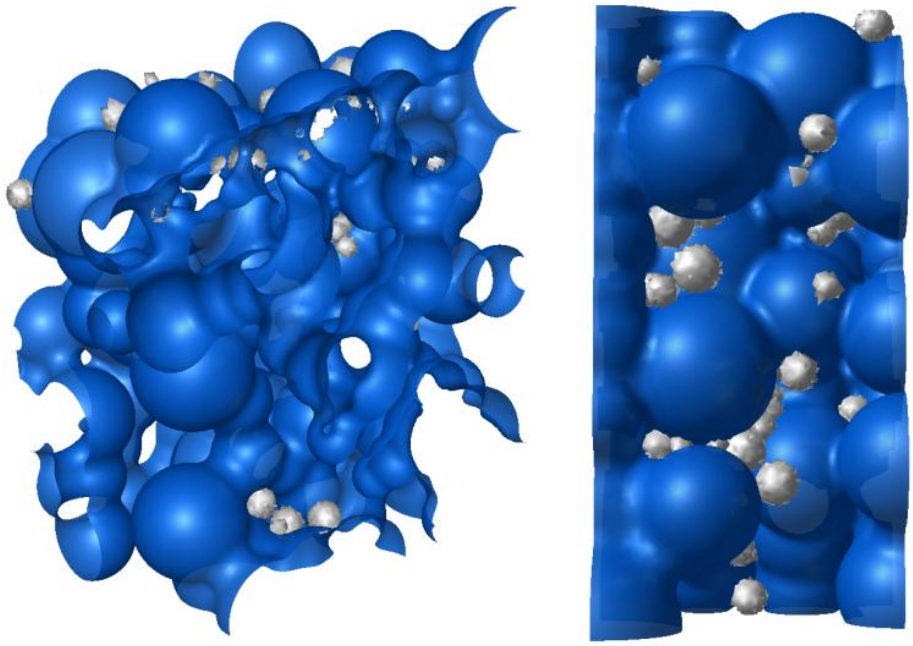

Figure 3.20 - Isometric/Top View of the Trapped Particles (light) and the Membrane (dark) in *New* MWF

The s*emi-used* MWF shows evidence of cake layer development as the primary mechanism of fouling and a secondary mode of fouling (partial pore blocking) prior to cake layer development. The former was visualized towards the end of the simulation in Fig. 3.19, whereas the latter was seen at times throughout the start of the simulation. Initial partial pore blocking transitioning into cake layer formation is similar to the progression of fouling documented by [43]. The particle size distribution of the *semi-used* MWF contained particles both larger and smaller than the average pore size causing more particles to trap than the *used* MWF. This is why Fig. 3.19 has more particles at the surface and why a higher flux decline was seen with *semi-used* MWFs. It is likely that the development of fouling, initiating with partial pore blocking, may be the motivation for the inclusion and study of repulsive surface electrostatics in [8] and [3].

The *new* MWF shows evidence of partial pore blocking as the primary mechanism of fouling. This particle size distribution has more small particles than both the *used* and *semi-used* MWF, allowing more particles to pass through pores and escape. As visualized in Fig. 3.20, this MWF showed a dearth in trapped particles. For the particles that did become trapped, their final positions were scattered throughout the tortuous pore region instead of just on the membrane surface. Since particles were only blocking pores, this manner of fouling is partial pore blocking.

Penetration Depth Profiles

The penetration depth profiles for the *semi-used* and *new* MWFs are displayed in Figs. 3.21 and 3.22. These figures show the particle disposition and trend of particle dispositions throughout the life of the simulations and show how the filter become blocked over time.

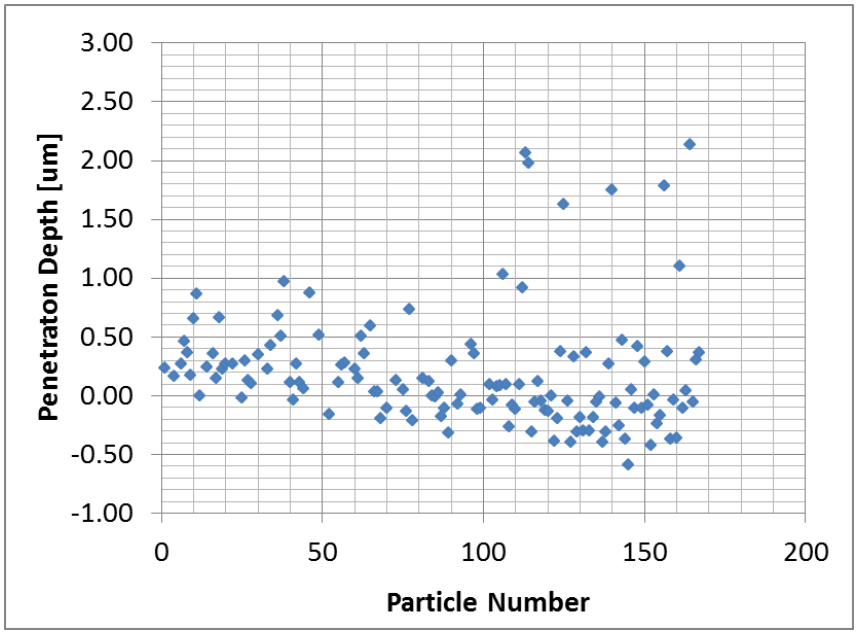

Figure 3.21 - Penetration Depth Profile for *Semi-used* MWF

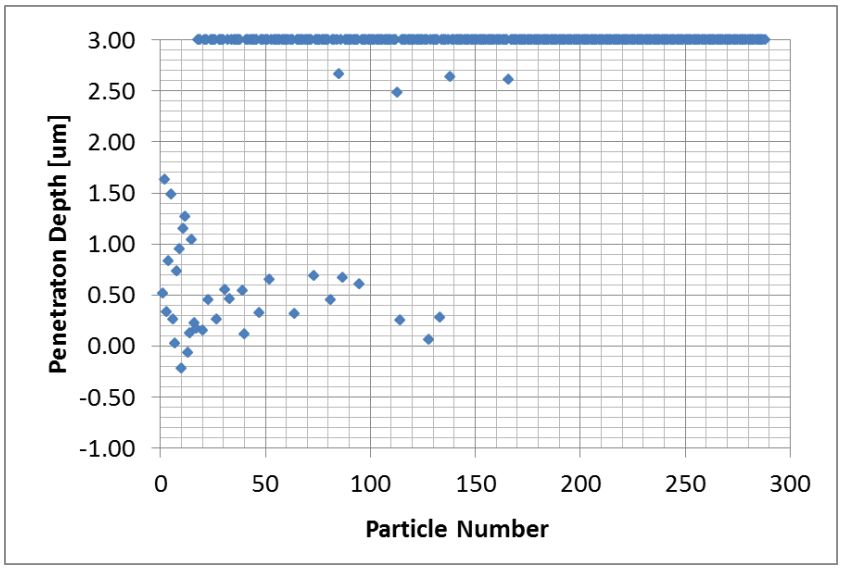

Figure 3.22 - Penetration Depth Profile for *New* MWF

The penetration depth profile of the *semi-used* MWF (Fig. 3.21) confirms that two fouling mechanisms are at work: initial partial pore blocking transitioning into cake layer development. Since the particle size distribution of the *semi-used* MWF has a range of

particles containing both small and large particles, different particle dispositions are possible: large particles will commonly block pores while small particles commonly escape. The two actions are evident in the relatively equal distribution of particles escaping and trapping at the start and middle of the simulation.

As more particles are injected (i.e., towards the end of the simulation), more particles trap than escape. This is because almost all pores are blocked, reducing the possibility of particles passing through the system and resulting in cake layer development. Particles become trapped with recorded penetration depths at the membrane surface, hinting at cake layer development. Further injected particles showed a linear decreasing trend of penetration depth, hinting at cake layer growth. Figure 3.19 confirms that particles are trapped in the bulk flow region and the layers are thick from growth.

The penetration depth profile of the *new* MWF (Fig. 3.22) shows evidence of initial partial pore blocking, but no cake layer development. Particles become trapped in arbitrary locations, regardless of penetration depth. This is evident at the start of the simulation. It is likely that due to their small sizes, particles travel anywhere in the membrane and become trapped at any location where a pore constriction exists.

This action blocks off small pores from flow. The streamlines of the flow adjust towards the remaining open, but large, pores. Particles follow these streamlines into the large pores and escape the system. This behavior is evident through the prevalent penetration depth readings of 3.00 µm, signifying particle escape, towards the middle and end of the simulation. At this time of the simulation, specifically after Particle 170, two features of the penetration depth profile for the *new* MWF were noted: (1) the rate of particles becoming trapped decreased

and (2) ultimately no particles become trapped. It is logical to reason that with the trend of the declining number of trapped particles, further injected particles may not become trapped. With no more particles trapped, it is possible that partial pore blocking, cake layer development, and ultimately, membrane fouling may become eliminated given a continuously maintained particle size distribution similar to this *new* MWF.

3.6 Conclusions

This chapter has presented a three-dimensional simulation of cross-flow microfilter fouling in tortuous pore profiles with semi-synthetic metalworking fluid. The conclusions from this work are:

- The three-dimensional model developed enables the prediction of flux decline, the results of which compares favorably to experimental results.
- The wall collision model enables particle simulation in three dimensions, as established techniques for visual identification of particle trapping is not possible due to mesh lines, fluid lines, and tortuous pore geometry.
- The particle trapping model enables the simulation and visualization of primary fouling mechanisms: partial pore blocking and cake layer development.
- Fouling was observed to initiate with partial pore blocking, leading to particle stacking, and followed by cake layer development.
- Cake layer growth was observed to be linear as they might be expected in simulations where cross-flow influence on cake layer development is not considered.
- *New* MWF does not show evidence of cake layer development, in contrast to cake layer development in the bulk-flow region by *semi-used* and *used* MWFs.

Chapter 4

Investigation of the Variables Governing Fouling on Flux Decline

4.1 Overview

In this chapter, the fluid dynamic model developed in Chapter 3 is enhanced with a model to simulate the particle-membrane electrostatic forces. The enhanced model will then be experimentally validated. The model will be used to investigate the effects of changing the variables: transmembrane pressure, particle-particle (PP) zeta potential, and particle-membrane (PM) zeta potential; on the contribution to flux decline from partial and complete pore blocking.

The electrostatic force model is first discussed. Next, details of the experimental validation of the fluid dynamic model are covered. Additional simulations are conducted via a design of experiments, and the results are presented and discussed. The chapter concludes with a summary of findings.

4.2 Enhanced Fluid Dynamic Model

4.2.1 Enhanced Electrostatic Force Model

There are two types of electrostatic forces: PP-electrostatic forces and PM-electrostatic forces. PP-electrostatic forces are between two simultaneously traveling particles, or between a traveling particle and the particles trapped in a tortuous pore geometry. Electrostatic forces are caused by the repulsion of two similarly-charged alternating layers of counter- and co-ions from two colloid surfaces [32, 44]. A special potential value, called the zeta potential, characterizes the electrostatic potential for the paired surfaces. In previous works, PP-electrostatic forces were approximated by the Derjaguin approximation of the linearized Poisson-Boltzmann equation [3, 8, 15].

PM-electrostatic forces may differ from the PP-electrostatic forces because of intrinsically or deliberately different surface potentials. The Derjaguin approximation, however, over-predicts the electrostatic force because it assumes that the majority of the electrostatic interaction energy is contributed at the point closest to both surfaces. This could be incorrect as different curvatures away from the point of closest approach may not contribute as high of forces [37]. Furthermore, the steric factor cannot be obtained for complex pore geometries as seen in the tortuous pore geometry of this research. The over-prediction of forces and the inapplicability in complex geometries leads to the consideration of another double layer electrostatic force model.

In the current research on a single traveling particle in a tortuous geometry, the Surface Element Integration (SEI) technique [37] was utilized to determine the PP-electrostatic forces between a traveling particle and trapped particles and the PM-electrostatic forces through

discrete, finite element calculations of paired interacting surfaces. This technique is based on a sphere-flat plate geometry interaction [35] as seen in Fig. 4.1.

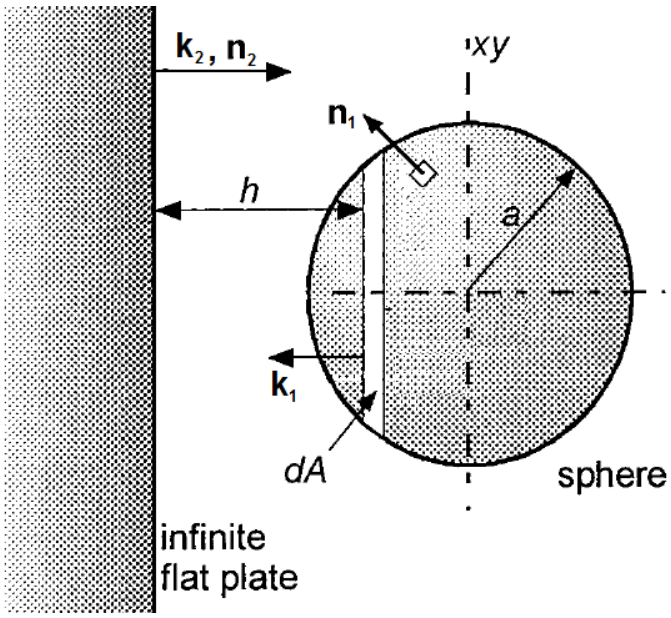

Figure 4.1 - Electrostatic Force of a Particle against an Infinite Flat Plate (Adapted from Bhattacharjee et al. [35])

The SEI technique determines the electrostatic energy, *U*, via:

$$U = \int \boldsymbol{n_2} \cdot \boldsymbol{k_2} \frac{\boldsymbol{n_1} \cdot \boldsymbol{k_1}}{|\boldsymbol{n_1} \cdot \boldsymbol{k_1}|} E(h) dA_1, \tag{4.1}$$

where $\boldsymbol{n_1}$ and $\boldsymbol{n_2}$ are the unit normal vectors of each element on each respective body, $\boldsymbol{k_1}$ and $\boldsymbol{k_2}$ are the unit normal vectors directed towards the positive z-axes of each body, and dA_1 is a differential area on the traveling particle. The flat plate interaction energy per area, $E(h)$, is given by the Hogg et al. expression of flat plate interaction energy per area:

$$E(h) = \frac{\varepsilon_0 \varepsilon_r \kappa}{2} \left[\left({\psi_1}^2 + {\psi_2}^2 \right) \{1 - \coth(\kappa h)\} + 2\psi_1 \psi_2 \cosh(\kappa h) \right], \tag{4.2}$$

where ε_0 is the permeability of free space, ε_r is the relative permeability, κ is the inverse Debye number, h is the closest distance between paired interacting surfaces, and ψ_i is the surface potential of surface i. Surface i is: 1 for the traveling particle or 2 for the encountered surface.

Although this development allows for the calculation of the electrostatic force in complex geometries, absolute values of the zeta potentials greater than 25 mV, such as those tested in the current fluid dynamic model, gives inaccurate results. Instead, the linear superposition approximation (LSA) calculates the interaction energy per unit area as the sum of the potential distribution of two interacting surfaces where the distribution from each body is calculated as if the other body was non-existent [34]. The flat plate interaction energy per area for the SEI technique [37]:

$$E(h) = 32\varepsilon_0\varepsilon_r\kappa\gamma_1\gamma_2\left(\frac{kT}{\nu e}\right)^2 \exp(-\kappa h), \tag{4.3}$$

where $\gamma_i = tanh(\Psi_i/4)$, $\Psi_i = \nu e\psi_i/kT$, k is the Boltzmann constant, T is the absolute fluid temperature, ν is the ionic charge number, and e is the electron charge. The zeta potential approximates the surface potential, which is difficult to experimentally determine [45].

The SEI technique utilizes the linear superposition approximation (LSA), Eqn. 4.3, for the flat plate interaction energy per area [37, 44] to determine the electrostatic energy, U, via:

$$U = \int n_2 \cdot k_2 \frac{n_1 \cdot k_1}{|n_1 \cdot k_1|}\left[32\varepsilon_0\varepsilon_r\kappa\gamma_1\gamma_2\left(\frac{kT}{\nu e}\right)^2 exp(-\kappa h)\right] dA_1. \tag{4.4}$$

The zeta potential approximates the particle surface potential, which is difficult to experimentally determine [45]. The integral in Eqn. 4.4 is evaluated over the surface of the

traveling particle. $n_2 \cdot k_2$ evaluates to 1 because both n_2 and k_2 are unit vectors that face the same direction on a flat plate [37].

In a finite element scheme, the integral in Eqn. 4.4 is discretized into the form,

$$U = \sum_{i=0}^{m} \frac{n_{1_i} \cdot k_{1_i}}{|n_{1_i} \cdot k_{1_i}|} \left[32 \varepsilon_0 \varepsilon_r \kappa \gamma_1 \gamma_2 \left(\frac{kT}{ve} \right)^2 exp(-\kappa h_i) \right] A_{1_i}, \tag{4.5}$$

where m is the total number of elements on the surface of the traveling particle, A_{1_i} is the area of each surface element on the traveling particle, and h_i is the distance between an element on the traveling particle and an element on the encountered surface. The interaction energy is then divided by the particle-center-to-membrane vector, $\vec{r}$, less the particle radius, a, to determine the electrostatic force, $\vec{F}_E$, of surfaces on the particle:

$$\vec{F}_E = \frac{U}{(|\vec{r}| - a) \cdot \hat{r}}, \tag{4.6}$$

where $\hat{r}$ is the particle-center-to-membrane unit vector.

The traveling particle was subdivided into sections, as shown in Fig. 4.2; these elements are called *particle surface elements.*

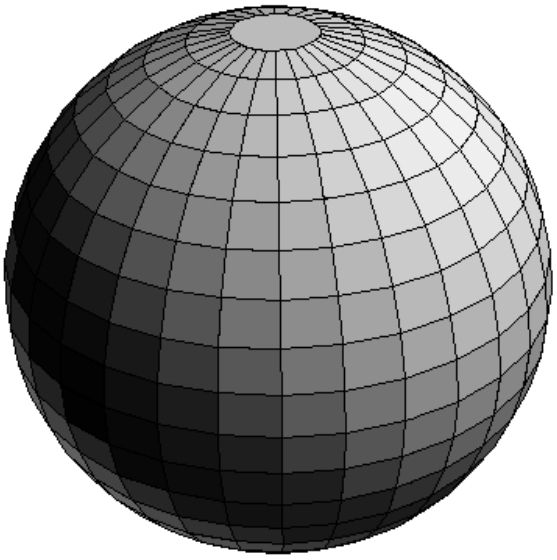

Figure 4.2 - Subdivided Traveling Particle

Membrane surface elements are finite elements on the surface of the three-dimensional pore geometry. If membrane surface elements are further than one Debye length away from the particle surface, the electrostatic force is electrically screened [30] and the force determination process is not executed; if one or more membrane surface elements are within the Debye length from one or more particle surface elements, the process to determine the electrostatic force is executed. This process, which determines all pair-wise electrostatic forces between the particle and a surface, is:

1. Determine, from a database of element identifiers, whether an interacting membrane surface element is a trapped particle or the membrane:
    - If the element was a trapped particle, substitute the PP-zeta potential for ψ_2;
    - If the element was the membrane, substitute the PM-zeta potential for ψ_2;
2. Calculate the electrostatic interaction energy of the membrane surface element against a particle surface element via Eqn. 4.5;

3. Repeat Steps 1 and 2 with other particle surface elements found within a Debye length from the membrane surface element;
4. Repeat Steps 1, 2, and 3 with other membrane surface elements found within a Debye length from the first particle surface element;
5. Sum all electrostatic interaction energies among all encountered particle surface elements and all membrane surface elements;
6. Find the electrostatic force on the particle via Eqn. 4.6.

4.2.2 Utilization of the Enhanced Fluid Dynamic Model in the Determination of Particle Trajectory

The electrostatic force, in conjunction with Brownian forces, $\vec{F}_B$, and hydrodynamic interactions, $\vec{F}_H$, are utilized in the Langevin equation to calculate the particle trajectory through the tortuous membrane geometry [3, 4, 8, 29], giving the enhanced fluid dynamic model:

$$m_P \frac{du_P}{dt} = \vec{F}_H + \vec{F}_B + \vec{F}_E, \tag{4.7}$$

where m_P is the mass of the particle, u_P is the velocity vector of the particle, and *t* is the time of the simulation. Together, the hydrodynamic force, electrostatic force, Brownian force, and particle disposition evaluations divert the particle from its typical trajectory, cause particles to interact with membrane surfaces, and initiate particle trapping.

The enhanced electrostatic force model is compared to two other electrostatic force models via three simulated particle trajectories to demonstrate the importance of PM-electrostatic

forces in the determination of particle trajectories. One force model, employed by [3, 8], implemented hydrodynamic forces and PP-electrostatic forces via the Derjaguin approximation. The other model, employed by [13], implemented only hydrodynamic forces. Brownian motion forces were ignored for the purpose of highlighting the differences solely between electrostatic force models.

Movement of three particles, each under the effects of one of these force models, was simulated in the enhanced fluid dynamic model. Each particle started at the same location on the pressure inlet and traveled through the tortuous three-dimensional geometry which is augmented by two trapped particles. The PP- and PM-zeta potentials for these simulations were -100 mV. The results from the particle trajectory simulations are shown in Fig. 4.3.

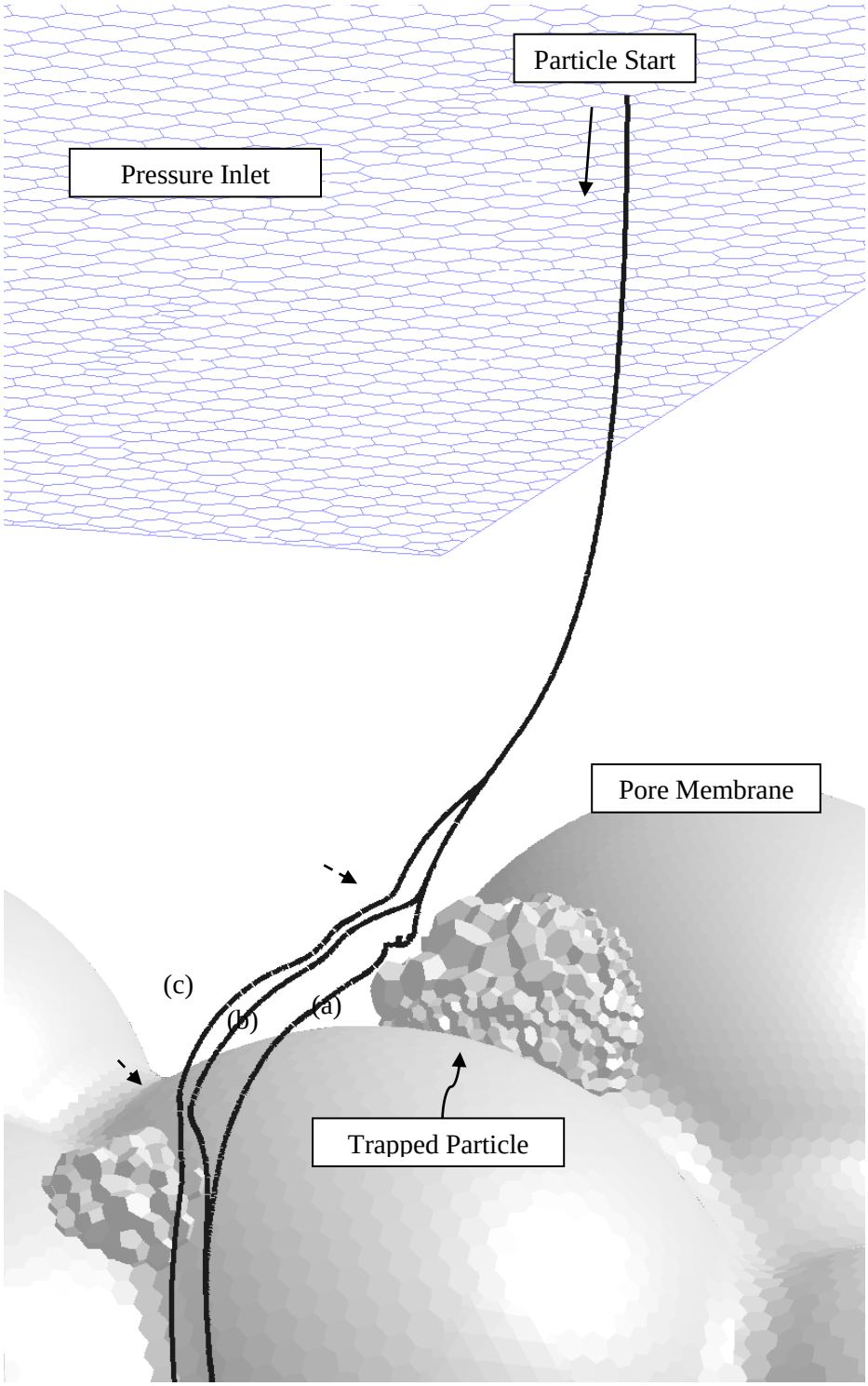

Figure 4.3 - Particle Trajectories Employing: (a) Hydrodynamics Only; (b) PP-electrostatic Forces via the Derjaguin Approximation; and (c) PP- and PM-electrostatic Forces via the Enhanced Electrostatic Force Model

The particle trajectory without electrostatic forces (a) moves from the pressure inlet down towards the membrane. The course is not altered by the membrane surface or the trapped particles. The particle trajectory employing the Derjaguin approximation (b) shows a particle that follows the same trajectory as (a) but becomes diverted near the first trapped particle. Its path is again altered as the particle nears the next trapped particle. The trajectory employing the enhanced electrostatic force model (c) initially matches the former two but splits earlier as the particle is affected by the PM-electrostatic forces near the membrane. The trajectory is then altered in two locations, indicated by the dashed arrows in Fig. 4.3, showing the effect of the PP-electrostatic force near trapped particles.

The marked difference in the particle trajectory of the enhanced electrostatic force model versus the other two force models demonstrates the importance of including PM-electrostatic forces.

4.3 Enhanced Fluid Dynamic Model Validation

4.3.1 Model Validation Methodology

Before the enhanced fluid dynamic model can be used for design purposes it must be experimentally validated. However, validation is made difficult because typical flux decline experiments involve three fouling mechanisms: adsorption leading to pore constriction, partial and complete pore blocking, and cake layer development; while in the enhanced fluid dynamic model, only partial pore blocking and complete pore blocking are at work.

The experimentally validated Zhao et al. [12] model accounts for flux decline contributions due to adsorption leading to pore constriction, partial and complete pore blocking, and cake layer development. This model may be fit to experimentally obtained flux decline data with parameter estimates that account for each of the fouling mechanisms. Further, the model may be simplified to represent the combined flux decline contribution of just partial and complete pore blocking. By verifying equivalent model parameters that characterize the combined effect of partial and complete pore blocking on flux decline between (1) the fit of the Zhao et al. model to the experimental flux data and (2) the fit of the simplified Zhao et al. model to the simulation flux data, validation of the enhanced fluid dynamic model can be achieved.

4.3.2 The Zhao et al. Model for Flux Decline Prediction

In [11], Song recognized that membranes can be partially blocked through the deposition of particles within the pores and developed a model that predicted flux decline due to partial and complete pore blocking, and cake formation. In [12], Zhao et al. extended the Song model to include pore constriction due to adsorption and predicted the total flux over time, $J(t)$, due to the impacts of three fouling mechanisms: adsorption leading to pore constriction, partial and complete pore blocking, and cake-layer formation. The Zhao et al. model:

$$J(t) = \frac{\Delta P}{R_m} \cdot e^{(-\alpha_b * t)} \cdot \left(e^{(-\alpha_c * t)} + (1 - R^*)^4 \cdot \left(1 - e^{(-\alpha_c * t)}\right)\right)$$

$$+ \frac{\Delta P}{R_{bm}} \cdot \left(1 - e^{(-\alpha_b * t)}\right) \cdot \left(1 + \frac{2 \cdot \Delta P \cdot \psi \cdot c_0 \cdot t}{R_{bm}^2}\right)^{-0.5}, \qquad (4.8)$$

is governed by five model parameters that define the effect of the three fouling mechanisms: internal pore restriction time constant, α_c, and steady-state effective internal restriction, R^*, both related to adsorption leading to pore constriction; partial and complete pore blocking time constant, α_b; the specific surface film resistance, ψ, related to cake layer development; and the partially blocked membrane resistance, R_{bm}. The concentration of fouling ingredients in the MWF, c_0, is determined from the concentration of foulants in the solvent and the MWF concentrate density. t is the independent variable, defined as the in-use time of microfiltration. The membrane resistance, R_m, is determined through experimentation to be the ratio of the transmembrane pressure and initial flux. The Zhao et al. model, Eqn. 4.8, is used to estimate α_c, R^*, α_b, ψ, and R_{bm} from experimental flux data.

The simplified Zhao et al. model, predicting flux from partial and complete pore blocking only, is derived from the Zhao et al. model, Eqn. 4.8. The terms representing the flux contribution from unblocked pores and partially and completely blocked pores are separated into $J_1(t)$ and $J_2(t)$, respectively. $J_1(t)$ is given by:

$$J_1(t) = \frac{\Delta P}{R_m} e^{(-\alpha_b * t)} \cdot \left(e^{(-\alpha_c * t)} + (1 - R^*)^4 \cdot \left(1 - e^{(-\alpha_c * t)}\right)\right). \tag{4.9}$$

Adsorption leading to pore constriction is ignored, therefore R^* is zero; the resulting equation after simplification is:

$$J_1(t) = \frac{\Delta P}{R_m} e^{(-\alpha_b * t)}. \tag{4.10}$$

$J_2(t)$ is given by:

$$J_2(t) = \frac{\Delta P}{R_{bm}} \cdot \left(1 - e^{(-\alpha_b * t)}\right) \cdot \left(1 + \frac{2 \cdot \Delta P \cdot \psi \cdot c_0 \cdot t}{R_{bm}^2}\right)^{-0.5}. \quad (4.11)$$

Contributions to flux decline in the enhanced fluid dynamic model do not include cake layer development. ψ is therefore zero; the resulting equation after simplification is:

$$J_2(t) = \frac{\Delta P}{R_{bm}} \cdot \left(1 - e^{(-\alpha_b * t)}\right). \quad (4.12)$$

Combining Eqns. 4.10 and 4.12 gives the simplified Zhao et al. model:

$$J(t) = \frac{\Delta P}{R_m} \cdot e^{(-\alpha_b * t)} + \frac{\Delta P}{R_{bm}} \cdot \left(1 - e^{(-\alpha_b * t)}\right), \quad (4.13)$$

which is the same as the Song model for flux decline due to partial and complete pore blocking [11]. Eqn. 4.13 is used to estimate α_b and R_{bm} from simulation flux data obtained from the enhanced fluid dynamic model.

4.3.3 Validation Experiment

The microfiltration validation experiment was completed using a laboratory-scale microfiltration testbed. The membrane used was an α-alumina tubular ceramic membrane with an average pore size of 0.5 μm. The initial water permeability of the membrane at 20°C as reported by the manufacturer is in the range of 4500-5500 L/hr-m^2 (LMH). The membrane is contained within a stainless steel membrane module. The entire system can be seen in Fig. 4.4. It consists of a 4-liter process tank that holds the metalworking fluid and feeds it into the inlet port of the membrane module through a 1 hp gear pump. The pressure entering (P1) and exiting (P2) the membrane module was measured and the transmembrane pressure was

calculated as the average of these two pressures. Transmembrane pressure was controlled by a butterfly valve downstream of the membrane. Permeated fluid that has passed through the membrane pores was collected and measured periodically by a data collection system. This data was then used to determine membrane flux decline as a function of filtration time.

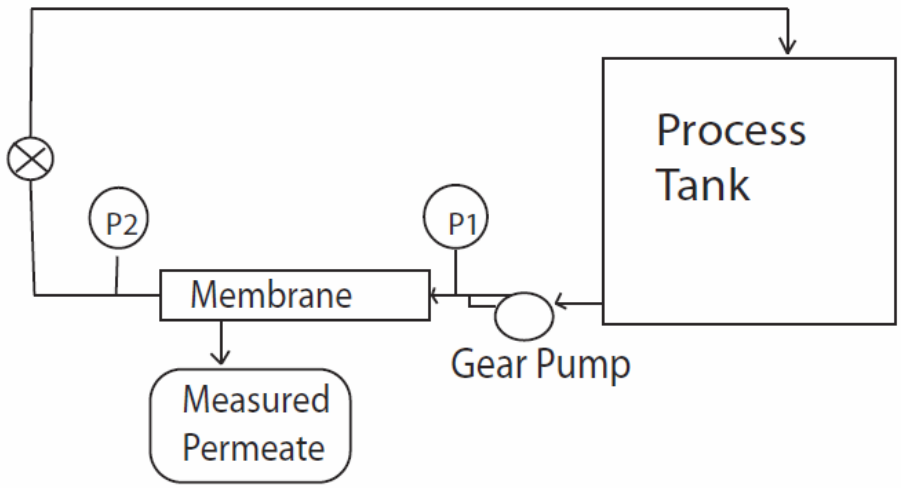

Figure 4.4 - Experimental Setup [28]

The validation experiment was performed by running 5% concentration Castrol Clearedge 6519 semi-synthetic MWF (with concentrate density of 996 kg/m^3) through a clean microfilter operating at 3.49 psig transmembrane pressure; the PP-zeta potential was measured to be -50 mV via laser Doppler electrophoresis (Zetasizer, Malvern Instruments Ltd, Worcestershire, UK) [3]. The PM-zeta potential was recognized to be zero due to the point of zero charge between the 9.1 pH fluid and the α-alumina microfilter [41]. Output flux data, in Fig. 4.5, shows relatively large decreases of flux at the start of the experiment; this continues for approximately 50 hours, at which time flux no longer decreases as sharply. At approximately 70 hours, the flux reaches steady-state.

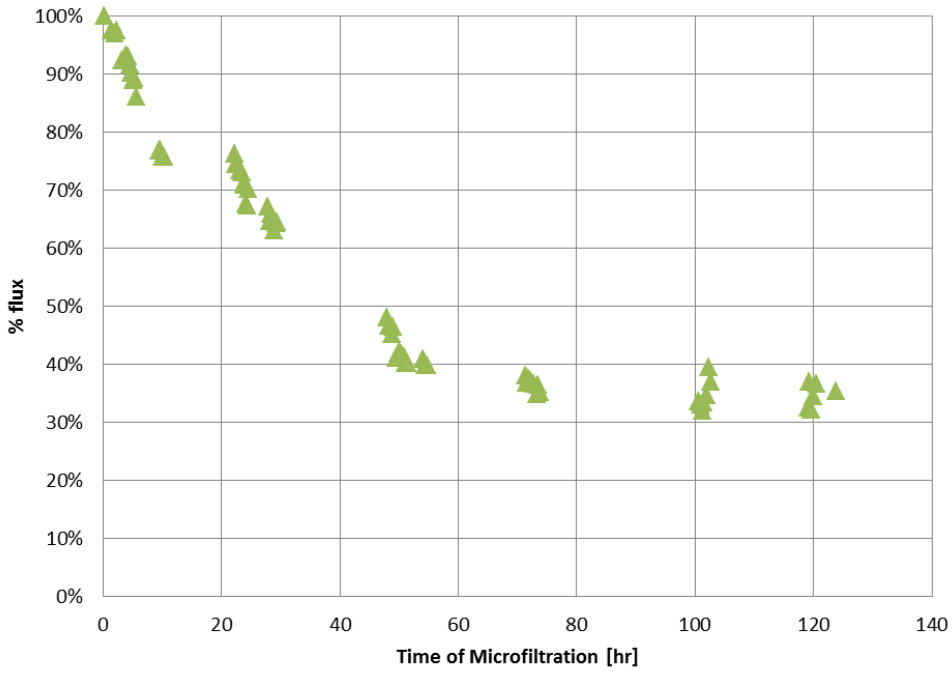

Figure 4.5 - Validation Experimental Flux Profile

The Zhao et al. model, Eqn. 4.8, was fit to the experimental flux data by minimizing the sum of squared errors to obtain estimates of α_c, R^*, α_b, ψ, and R_{bm}. The fluid properties and experimental operating conditions are as follows. c_0 was 25 kg/m^3, obtained from a concentrate of Castrol Clearedge 6519 with density of 996 kg/m^3 and foulant ingredient composition of 50%, diluted 5% in solvent. Based on experimental operating conditions, the transmembrane pressure was 24.1 kPa, and R_m was 1.4e8 Pa-s/m per the ratio of the transmembrane pressure and the initial flux of 641.9 LMH. Both the experimentally-determined flux decline data and the fitted Zhao et al. model are displayed in Fig. 4.6 along with the estimates of the model parameters. The coefficient of determination of the fit was 0.97.

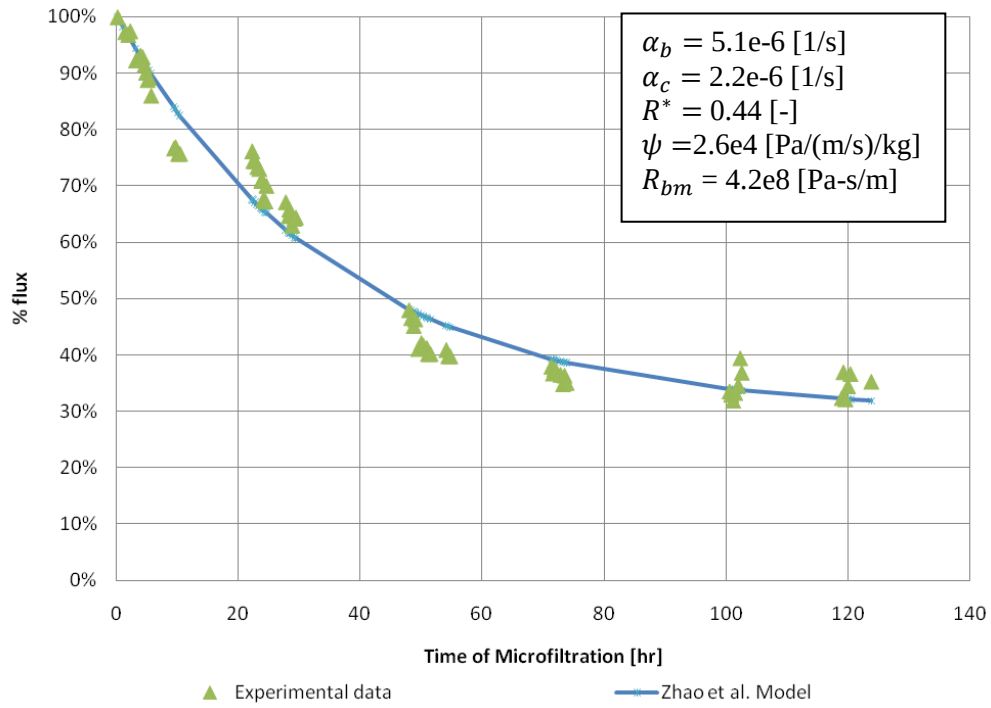

Figure 4.6 - Experimental Flux Decline Profile and Fitted Zhao et al. Model

The similar values of the partial and complete pore blocking time constant and internal restriction time constant suggests that the adsorption leading to pore constriction and partial and complete pore blocking occur at similar rates and have similar durations. The value of R^* suggests that pore constriction contributes to more than half of the total flux decline. A R_{bm} value that is three times the resistance of R_m suggests that one-third of the initial flux still remains when the experiment and model is at steady-state, which in fact is what the data approximates. Since ψ is smaller in magnitude versus the resistances of adsorption leading to pore constriction and partial and complete pore blocking, it is likely that the developed cake layer does not contribute significantly to flux decline at this point.

4.3.4 Fitting the Simplified Zhao et al. Model to the Enhanced Fluid Dynamic Model Data

The simplified Zhao et al. model, Eqn. 4.13, was fit to simulation flux data by minimizing the sum of squared errors to obtain an estimate of α_b and R_{bm}. To mimic the conditions of the validation experiment, the simulation was run at the same microfilter operating conditions, namely a transmembrane pressure of 24.1 kPa and initial flux of 641.9 LMH. R_m was the same as the experiment: a ratio of the transmembrane pressure and initial flux of the validation experiment, equaling 1.4e8 Pa-s/m. The flux data consisted of the average flux profiles of simulations for two pore geometries (Fig. 4.7); this was done to obtain data more typical of flux decline in the bulk microfilter. The average flux profile, the simplified Zhao et al. model, and the estimated model parameters can be seen in Fig. 4.8. The coefficient of determination is 0.96. The value of the estimated partial pore blocking time constant and that from the validation experiment are within 2.0%, suggesting that the enhanced fluid dynamic model provides a good representation of the actual flux decline due to partial pore blocking. The R_{bm} value for the 47 hour simulation is only 36% of the value for the 125 hour experimental data. This is expected because R_{bm} indicates the resistance of the partially blocked membrane and therefore should increase with permeation time as the membrane becomes progressively more blocked.

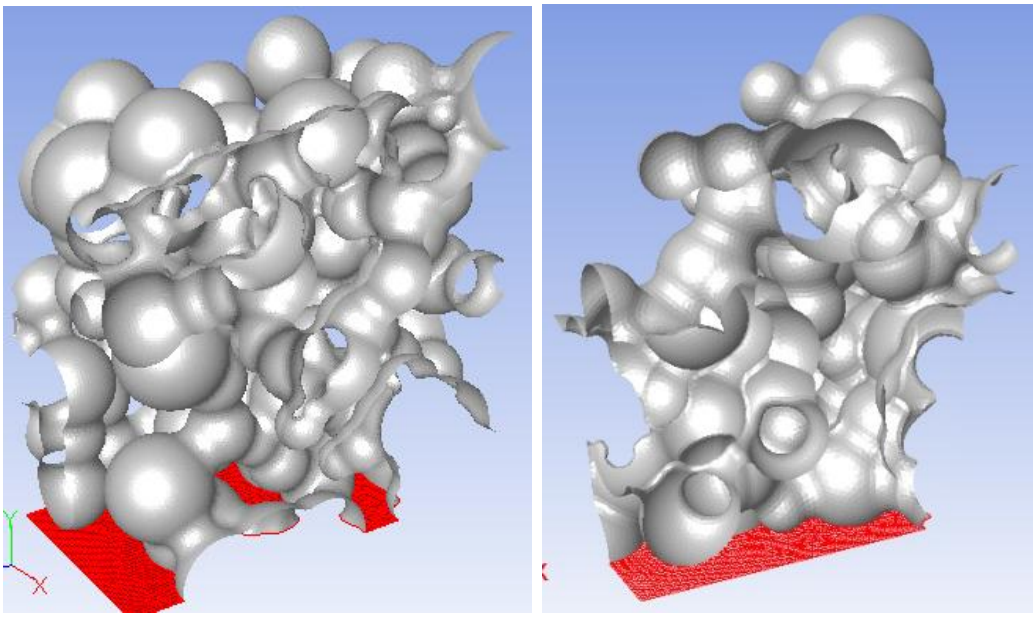

Figure 4.7 - Tortuous Pore Geometry 1 (left) and 2 (right)

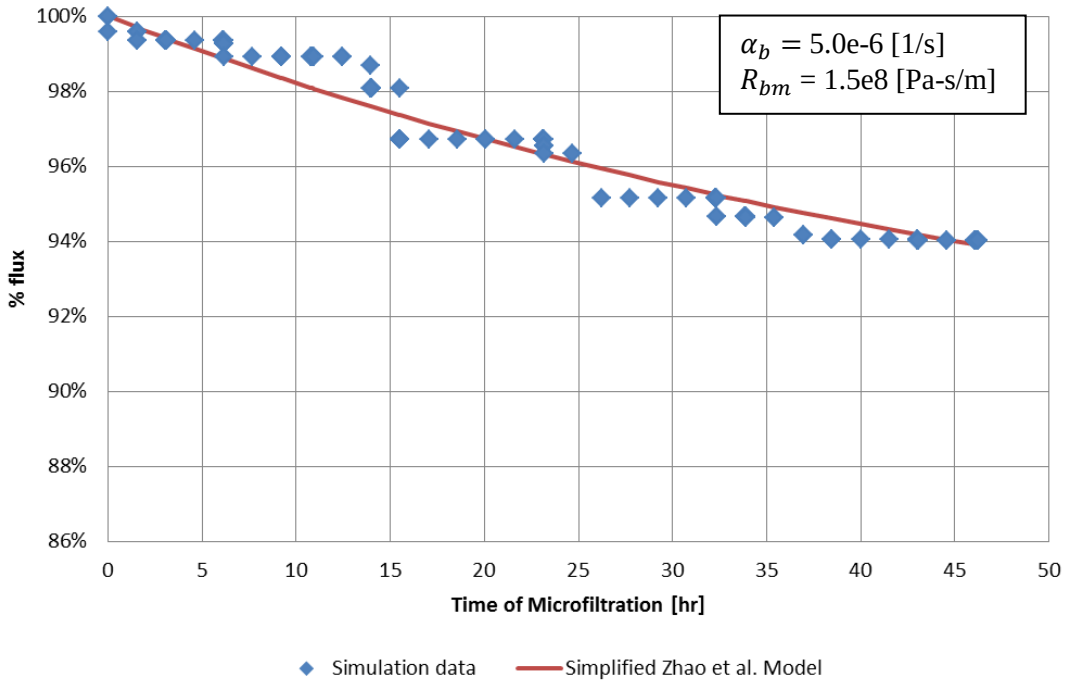

Figure 4.8 - Simulation Flux Data and the Simplified Zhao et al. Model

4.4 Investigation of Flux Decline

Hydrodynamic forces and electrostatic forces are important physical phenomena that affect partial pore blocking in microfiltration. To understand how best to reduce fouling due to partial pore blocking, some of the variables that govern these physical phenomena are now studied via the validated enhanced fluid dynamic model. Understanding the effects of such variables can lead to the development of a knowledge base for designing better microfilters and MWFs.

4.4.1 Design of Simulation Experiments

The input variables affecting partial pore blocking and flux decline examined here are: transmembrane pressure, PP-zeta potential, and PM-zeta potential. The variable values studied were determined from previous works [21] and from experimental measurements of MWF samples via laser Doppler velocimetry and phase analysis light scattering, and range from 10 to 40 kPa for transmembrane pressure and -100 to 0 mV for both PP- and PM-zeta potential.

The output response characterizing microfiltration efficacy is % flux decline and is determined by:

$$\Delta V = \frac{J_{initial} - J_{final}}{J_{initial}} \cdot 100\%, \tag{4.14}$$

where the initial flux, $J_{initial}$, and the final flux, J_{final}, are the values of the first and last data points in a set of flux data.

Since it is expected that the three input variables have non-linear effects on flux decline [3, 4, 8, 21], a central composite design of experiments (CCD) was chosen so as to enable the study of multi-level variable effects. The CCD employed here is shown in Table 4.1.

Table 4.1 - Central Composite Design of Experiments

	Test number	Variables			Response
		Transmembrane pressure, ΔP, [kPa]	PP-zeta potential, Ψ_p, [mV]	PM-zeta potential, Ψ_m, [mV]	% Flux decline, ΔV, [-]
Centerpoint	1	25.0	-50	-50	8.1%
Factorial points	2	33.7	-25	-25	10.7%
	3	33.7	-25	-75	4.5%
	4	33.7	-75	-25	6.7%
	5	33.7	-75	-75	3.8%
	6	16.3	-25	-25	2.3%
	7	16.3	-25	-75	3.0%
	8	16.3	-75	-25	4.1%
	9	16.3	-75	-75	8.1%
Axial points	10	40.0	-50	-50	6.7%
	11	10.0	-50	-50	5.4%
	12	25.0	0	-50	3.7%
	13	25.0	-100	-50	5.0%
	14	25.0	-50	0	7.2%
	15	25.0	-50	-100	6.0%

4.4.2 Conducting the Simulation Experiments

Each operating condition for the simulation experiments in Table 4.1 was input into the enhanced fluid dynamic model. The model simulated particles that traveled, one at a time, through the tortuous pore geometry. Once the disposition of a particle was known (escaped or trapped), the next particle was injected into the geometry. Escaped particles do not reduce system flux, likewise, not all trapped particles do either; in fact, system flux is reduced only when trapped particles reduce the size of the minimum cross-sectional area, which solely

regulates the amount of incompressible fluid flow. Some particles may trap in blind pores [46] or other locations that do not reduce the minimum cross-sectional area and therefore do not reduce the system flux. The system flux after each trapped particle was obtained via:

$$\dot{V} = A_{min}\bar{v}_{min}, \tag{4.15}$$

where A_{min} is minimum area among the forty-two (42) two-dimensional cross-sectional areas in the modeled portion of the tortuous pore geometry that is shown to the right in Fig. 4.7. Each of these cross-sectional areas are calculated every 0.1 μm throughout the depth of the three-dimensional tortuous pore geometry. $\bar{v}_{min}$ is the average of the velocity magnitudes of all finite elements in the corresponding minimum area. The flux after each trapped particle was recorded as one data point on a flux decline profile. No more data was added to the flux decline profile when the simulation stopped as a result of simulated particles having sizes that were no longer characteristic of partial pore blocking, but instead of cake layer development.

In Fig. 4.9, a sequence of four images for simulation experiment test number 9 shows a partial set of trapped particles, where particle 2, 12, 31, and 38 trapped in the geometry while the remaining particles from 1 to 37 escaped. The flux decline associated with each trapped particle was 0, 0.1%, 0, and 0.5%, respectively, demonstrating: non-zero % flux decline from particles reducing the minimum cross-sectional area; and zero % flux decline from particles trapped in blind pores or other locations that do not reduce the minimum cross-sectional area.

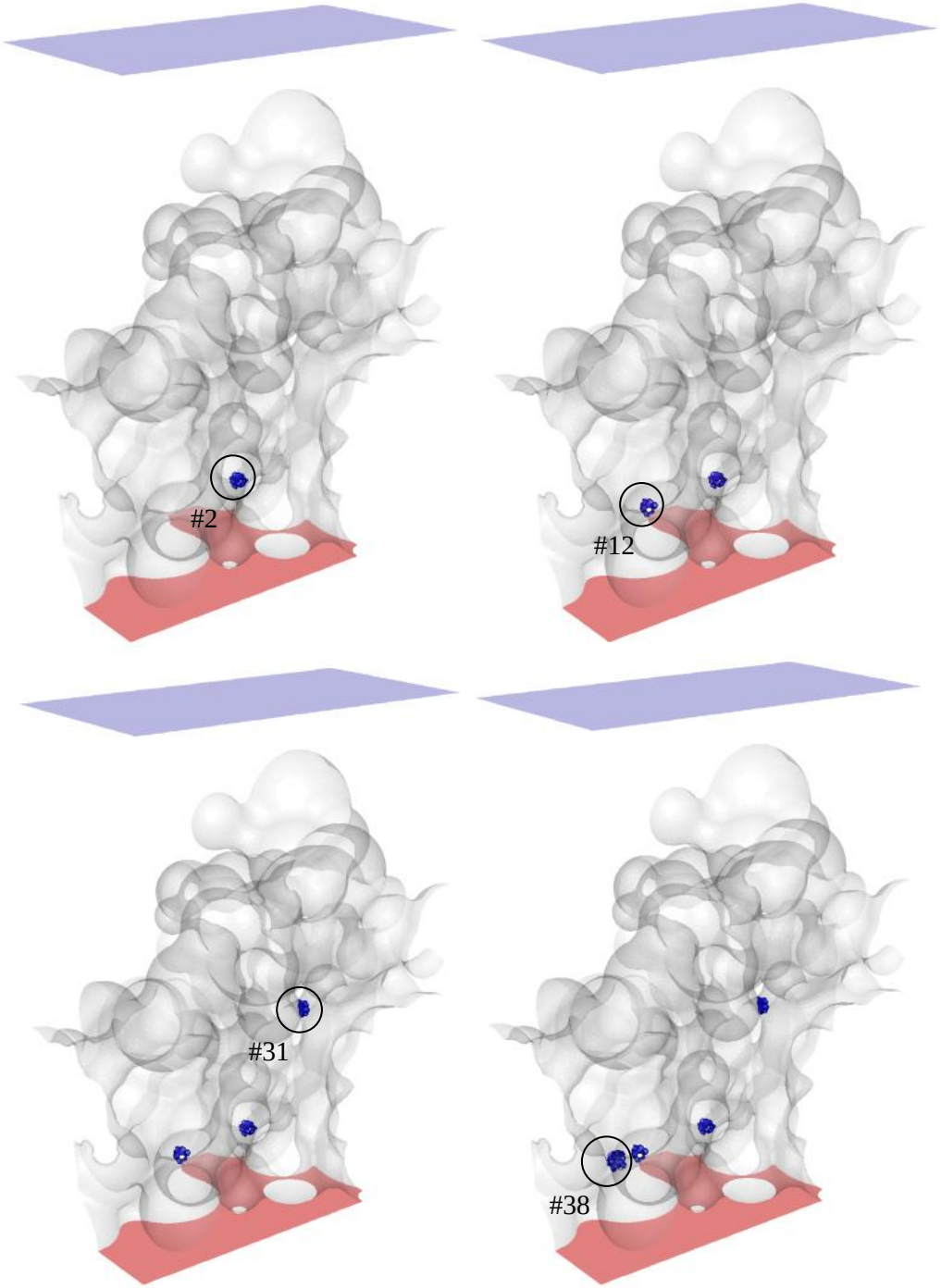

Figure 4.9 - Trapped Particles via the Enhanced Fluid Dynamic Model Operating at a Transmembrane Pressure of 16.3 kPa and PP- and PM-zeta Potentials of -75 mV (Simulation Experiment Test Number 9)

4.5 Results and Discussion

The CCD results were analyzed via a second-order model and its associated contour diagrams to reveal the effects of transmembrane pressure, PP-zeta potential, and PM-zeta potential on % flux decline. The second-order model, as a function of input variables ΔP, Ψ_{PP}, and Ψ_{PM}, was found via the least-squares method [47] to be:

$$\Delta V = -19.9846 + 1.2748\Delta P - 0.259\Psi_{PP} - 0.1717\Psi_{PM} + 0.0067\Delta P\Psi_{PP} + 0.008\Delta P\Psi_{PM} + 0.0013\Psi_{PP}\Psi_{PM} - 0.0091\Delta P^2 - 0.0015{\Psi_{PP}}^2 - 0.0006{\Psi_{PM}}^2. \quad (4.16)$$

The fitted model coefficient of determination is 0.98. Contour diagrams of Eqn. 4.16 are in Fig. 4.10.

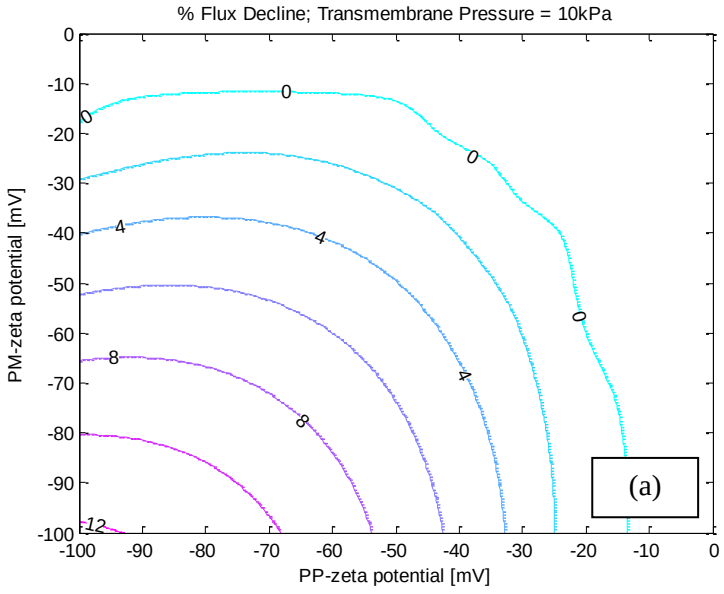

Figure 4.10 - Contour Diagrams for % Flux Decline Varying Two Input Variables, Operating at Transmembrane Pressures of (a) 10 kPa

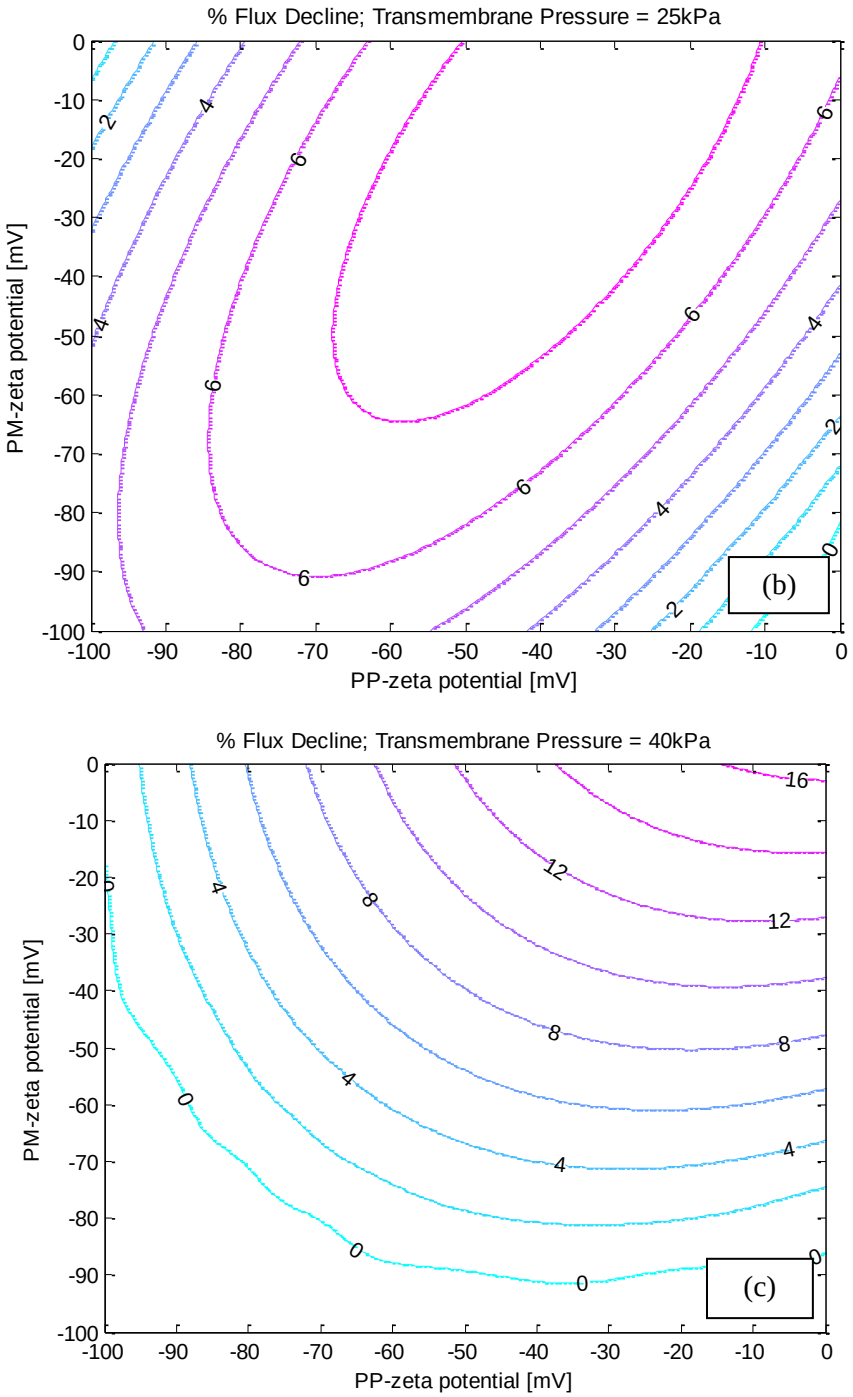

Figure 4.10 (cont.) - Contour Diagram for % Flux Decline Varying Two Input Variables, Operating at Transmembrane Pressures of (b) 25 kPa and (c) 40 kPa

Figure 4.10 shows that the effect of PP-zeta potential and PM-zeta potential on % flux decline varies greatly with three levels of transmembrane pressure: low, moderate, and high. At values of more-negative PP- and PM-zeta potentials, low transmembrane pressures give high % flux decline, whereas high transmembrane pressures for such PP- and PM-zeta potentials give low % flux decline. Furthermore, at near-zero values of PP- and PM-zeta potential, low transmembrane pressures give low % flux decline, whereas high transmembrane pressures give high % flux decline for the same near-zero values of PP- and PM-zeta potential. This response behavior creates maximum % flux decline in each contour diagram in Fig. 4.10 that trends from more-negative values of PP- and PM-zeta potential for the low transmembrane pressure (Fig. 4.10(a)) to the near-zero values of PP- and PM-zeta potential for the high transmembrane pressure (Fig. 4.10(c)). The value of the maximum % flux decline changes from 12 percent to 7 percent to 16 percent for low, moderate, and high transmembrane pressures, respectively.

Examination of % flux decline due to specific combinations of input variables helps to reveal the physical nature of the underlying partial pore blocking mechanisms. High % flux decline is caused by competing hydrodynamic and electrostatic forces on particles entering the largest membrane pore (primary pore, arrows in Fig. 4.11) and small membrane pores (secondary pores, circled in Fig. 4.11; depicted only once to maintain visual clarity). In simulation experiment test number 2, where imparted hydrodynamic forces from high transmembrane pressure overcome low electrostatic forces, particles block various secondary pores in addition to the primary pore, as seen in Fig. 4.11(a). Similarly, in simulation experiment test number 9, imparted electrostatic forces from high PP- and PM-zeta potentials overcome low hydrodynamic forces due to low transmembrane pressures and repel particles

to block secondary pores after the primary pore has been blocked; trapped particles can be seen in both the primary pore and secondary pores in Fig. 4.11(d). In these two operating scenarios, primary and secondary pores have become blocked, reducing flow area and flux; these conditions led to high % flux decline.

Observations of low % flux decline can also be explained with the same competing hydrodynamic and electrostatic forces. For low pressure and low potentials, particles are not restricted in their movement and are free to trap throughout the pore membrane; this behavior is seen in the scattered distribution of particles throughout the membrane and a dearth of particles in the primary pore of Fig. 4.11(c), simulation experiment test number 6. For high pressure and high potentials, particles are restricted to the fluid streamline with the highest flow rate, the primary pore. Partial pore blocking is therefore concentrated in one area and does not affect secondary pores; this is seen in Fig. 4.11(b), simulation experiment test number 5, where the majority of particles are trapped at the primary pore. In these two cases, not once are both primary and secondary pores blocked simultaneously, leading to low % flux decline.

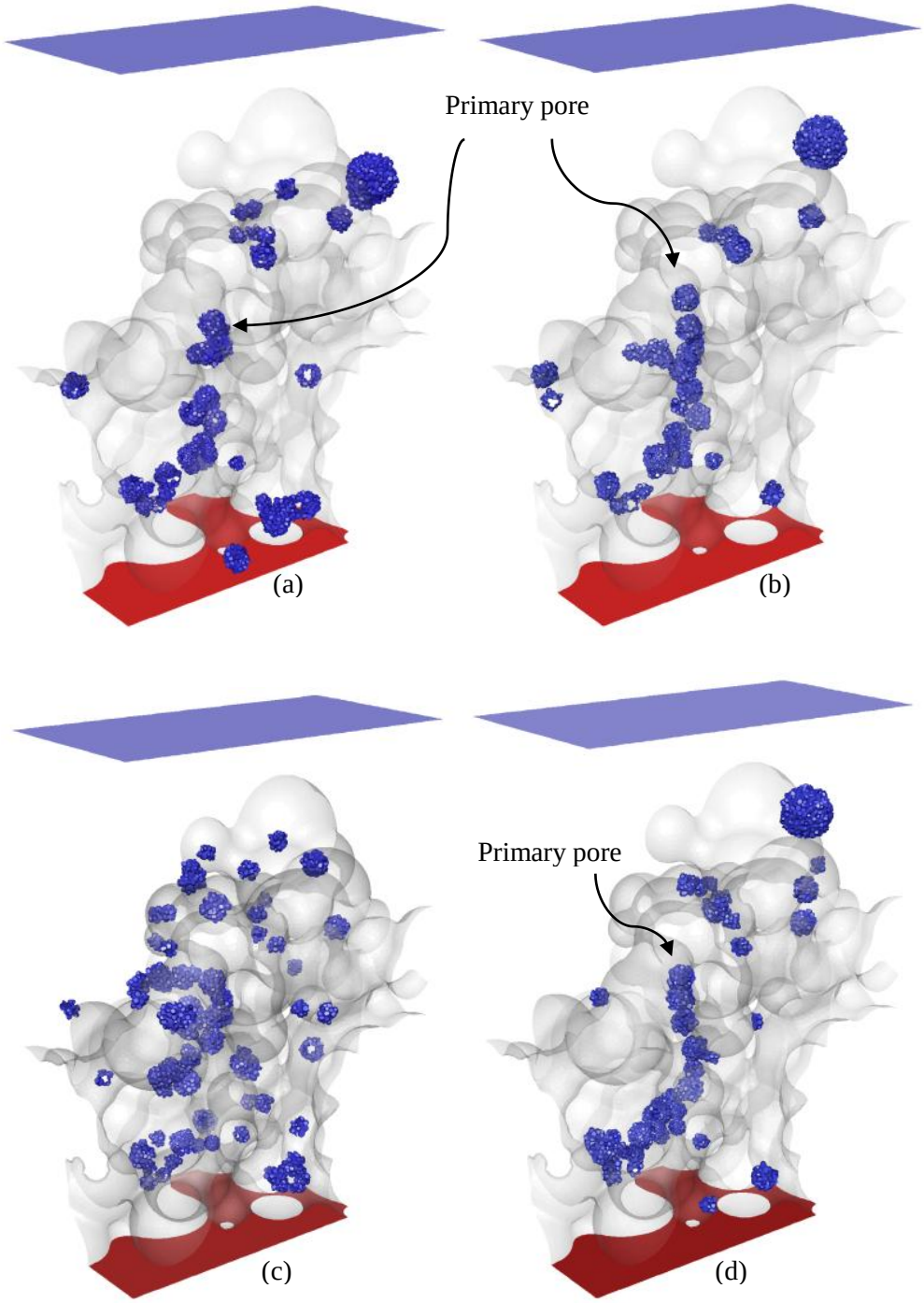

Figure 4.11 - Results of Simulation Experiment (a) Test Number 2; (b) Test Number 5; (c) Test Number 6; and (d) Test Number 9; Secondary Pore Locations are Circled only in Fig. 4.11(a) to Maintain Visual Clarity

Fig. 4.12(b) shows the effect of altering only PP-zeta potential causing the primary pore to open and particles to aggregate in secondary pores. It is interesting to note that in this particular case, comparison among preferential pore fouling in Figs. 4.12(a), (b), and Fig. 4.11(b) and correlation to the flux decline of simulation experiment test number 2, test number 4, and test number 5, suggests that blocking secondary pores leads to larger flux decline than blocking primary pores at high transmembrane pressures (Table 4.2).

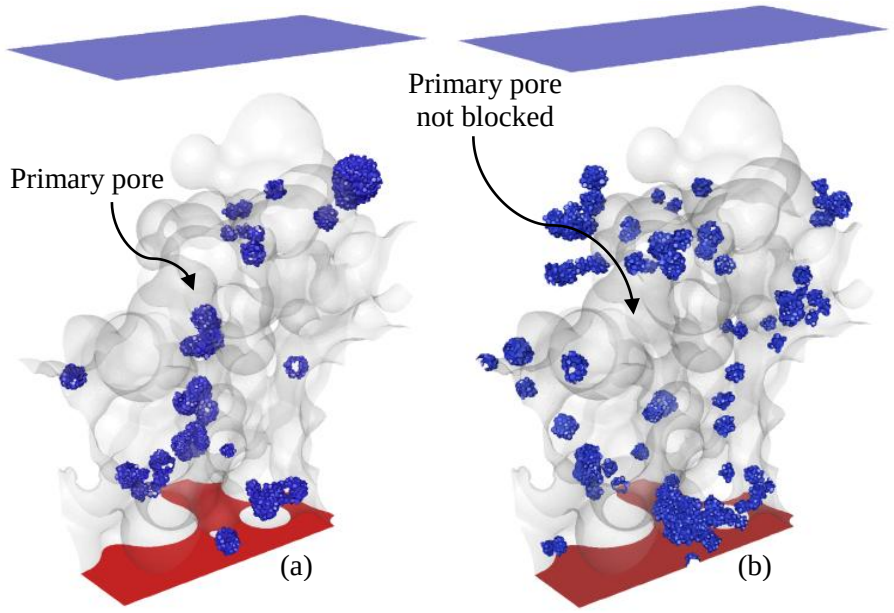

Figure 4.12 - Results of Simulation Experiment (a) Test Number 2 and (b) Test Number 4

Table 4.2 - Effect of Partially Blocked Pore Type on % Flux Decline

Figure number	Partially blocked pore type	ΔP, [kPa]	Ψ_p, [mV]	Ψ_m, [mV]	% Flux decline
12(a)	Primary and Secondary	33.7	-25	-25	10.7%
12(b)	Secondary	33.7	-25	-75	6.7%
11(b)	Primary	33.7	-75	-75	3.8%

The fact that electrostatically charged particles, trapped in the membrane at certain locations, can reduce flux decline suggests that charges in the membrane at strategic locations, if physically possible to impart, can have the same effect.

4.6 Conclusions

The conclusions from this work are:

- The fluid dynamic model was enhanced to include particle-membrane electrostatic forces.
- Simulations conducted with no electrostatic forces, only PP-electrostatic forces, and both PP- and PM-electrostatic forces produced distinctly different particle trajectories in the membrane pore structure.
- Validation of the enhanced fluid dynamic model was accomplished by comparing experimental flux decline data with simulation flux decline data.
- The validated enhanced fluid dynamic model was employed to investigate the effects of transmembrane pressure, particle-membrane zeta potential, and particle-particle zeta potential on flux decline due to partial and complete pore blocking via a set of simulation experiments.
- The simulation experiment results revealed: low flux decline at low transmembrane pressures and near-zero values of PP- and PM-zeta potential; and low flux decline at high transmembrane pressures and more-negative values of PP- and PM-zeta potential.

- The effect of various combinations of transmembrane pressure, PP-zeta potential, and PM-zeta potential on flux decline was shown to be correlated to the specific nature of partial and complete pore blocking in the pore structure.
- Interpretation of the simulation experiment results suggests the possibility of reducing flux decline by applying electrostatic forces to certain locations of the microfilter, instead of to its entirety.

Chapter 5

Conclusions and Recommendations

5.1 Overview

The objective of this research is to predict the flux decline of semi-synthetic MWFs in cross-flow microfiltration via a three-dimensional fluid dynamic model of the tortuous pore geometry. The first stage of this research was to create a three-dimensional tortuous pore fluid dynamic model. The second stage was to enhance the fluid dynamic model with particle-membrane electrostatic forces. The third stage of this research was to validate the enhanced fluid dynamic model. The fourth stage was to investigate the nature of microfilter flux decline through a series of design of simulation experiments.

5.1.1 Creation of the Three-dimensional Tortuous Pore Fluid Dynamic Model

The three-dimensional tortuous pore geometry was created from images of two-dimensional cross-sectional slices of a α-alumina microfilter obtained from the focused ion beam. A wall collision model and a particle trapping model were developed for the investigation of fouling mechanisms. Hydrodynamic, particle-particle electrostatic forces, Brownian forces, and the wall collision model and particle trapping model were used in the reconstructed geometry via computational fluid dynamics to simulate metalworking colloidal particles traveling through and becoming trapped in the tortuous pore paths of a microfilter. The major conclusions from this stage of the research were:

- The three-dimensional model developed enables the prediction of flux decline, the results of which compare favorably to experimental results.
- The wall collision model enables particle simulation in three dimensions, as established techniques for visual identification of particle trapping is not possible due to mesh lines, fluid lines, and tortuous pore geometry.
- The particle trapping model enables the simulation and visualization of primary fouling mechanisms: partial pore blocking and cake layer development.
- Fouling was observed to initiate with partial pore blocking, followed by cake layer development.
- Cake layer growth was observed to be linear as they might be expected in simulations where cross-flow influence on cake layer development is not considered.

- For the microfilter simulations experiments with MWFs of varying in-use time profiles (new, semi-used, and used), *new* MWF does not show evidence of cake layer development, in contrast to cake layer development in the bulk-flow region by *semi-used* and *used* MWFs.

5.1.2 Enhancement of the Fluid Dynamic Model with Particle-Membrane Electrostatic Forces

- The fluid dynamic model was enhanced with particle-membrane electrostatic forces via the Surface Element Integration technique and the linear superposition approximation of the flat plate interaction energy per area.
- Simulations conducted with no electrostatic forces, only PP-electrostatic forces, and both PP- and PM-electrostatic forces produced distinctly different particle trajectories in the membrane pore structure.

5.1.3 Validation of the Enhanced Fluid Dynamic Model

The enhanced fluid dynamic model was validated by comparing model parameters characterizing partial and complete pore blocking between the fit of the Zhao et al. flux decline model to experimental flux decline data and the fit of the simplified Zhao et al. flux decline model, based only on partial and complete pore blocking, to simulation flux decline data. The major conclusions from this stage of the research were:

- An experimental cross-flow microfiltration testbed was successfully developed to operate with α-alumina microfilters and semi-synthetic MWFs, control transmembrane pressure, and measure permeate flux. The testbed was used to conduct flux decline experiments for the purpose of model validation.
- The value of the estimated partial and complete pore blocking time constant and that from the validation experiment are within 2.0%, suggesting that the enhanced fluid dynamic model provides a good representation of the actual flux decline due to partial and complete pore blocking.
- The value of the estimated partial and complete pore blocking time constant and that from the validation experiment are within 2.0%, suggesting that the enhanced fluid dynamic model provides a good representation of the actual flux decline due to partial and complete pore blocking.
- Estimates of the time-dependent parameter for membrane resistance due to partial and complete pore blocking compare favorably in relative magnitude, given the relative time duration of the flux decline experiments and the model simulations of flux decline. This provides further evidence of the validity of the enhanced fluid dynamic model.

5.1.4 Investigation of Microfilter Flux Decline

The fluid dynamic model was employed via a central composite design of simulation experiments to investigate the effects of transmembrane pressure, particle-membrane zeta

potential, and particle-particle zeta potential on flux decline due to pore blocking via a set of simulation experiments. The major conclusions from this stage of the research were:

- The simulation experiment results revealed: low flux decline at low transmembrane pressures and near-zero values of PP- and PM-zeta potential; and low flux decline at high transmembrane pressures and more-negative values of PP- and PM-zeta potential.
- The effect of various combinations of transmembrane pressure, PP-zeta potential, and PM-zeta potential on flux decline was shown to be correlated to the specific nature of partial and complete pore blocking in the pore structure.
- Interpretation of the simulation experiment results suggests the possibility of reducing flux decline by applying electrostatic forces to certain locations of the microfilter, instead of to its entirety.

5.2 Recommendations for Future Work

5.2.1 Inclusion of Multiple Particle Injections

Particles introduced into the tortuous pore geometry are typically larger than 100 nm. Due to their likelihood of existence in the MWF, they are therefore introduced one-by-one into the geometry. Particles smaller than 100 nm in diameter have not been introduced into the system due to the assumption that their small size is not likely to cause partial or complete pore blocking. Yet these small particles lead to membrane adsorption, pore constriction, and flux decline, phenomena unable to be modeled because of the inability for simultaneous

particle injection. The enhancement of the fluid dynamic model would enable simulation of these small particles and the adsorption fouling mechanism for the first time.

Particle movement is governed by the Langevin equation and other force models, such as electrostatic and Brownian forces, and particle disposition schemes. One particle can be successfully injected and its disposition determined. It is suggested to apply the Langevin equation and the force models to simultaneously to particles smaller than 100 nm that are introduced into a pore geometry. Multiple particles can then be simulated to adsorb onto surfaces and mimic the adsorption fouling mechanism.

It is shown in [8, 14] that the onset of PP-electrostatic forces occurring between two traveling particles was significant in affecting particle disposition. The application of PP-electrostatic forces can be applied to further increase the accuracy of the fluid dynamic model.

Lastly, current particle trajectory simulations are computationally tractable because only one particle is introduced into the pore geometry at a time. However as the number of particles introduced increase, simultaneous required solutions of the Langevin equation for multiple particles may be computational intractable. Multi-core simulation for the determination of one particle trajectory is recommended to reduce the computation time for one trajectory, or simulation for the determination of multiple particles at the same time is recommended to reduce the needs for the computer to loop through multiple injected particles.

5.2.2 MWF Design

Results from the prediction of the effects of transmembrane pressure, PP-zeta potential, and PM-zeta potential on flux decline have been revealed in Chapter 4. However, the usage of the knowledge base developed in this research to reduce flux decline in experimental applications have not been explored. The empirical investigation of different operating conditions based on the knowledge base gained in this research can help to design better MWFs and microfilter membranes for increased compatibility between semi-synthetic MWFs and microfilters.

To establish a foundation for these experiments, an experimental testbed should be built. A system similar to [4, 7] allows control over the parameters involved in microfiltration. To the very least, the ability to control transmembrane pressure and the ability to measure the PP- and PM-zeta potential should be implemented into, or operated in conjunction with, the testbed system. Microfilter transmembrane pressure can be controlled by maintaining a pressure differential across the microfilter via pressure gauges and flow regulators. Reduced lead times and testing costs associated with zeta potential measurements can be had by purchasing a Malvern Zetasizer.

Since the zeta-potential of MWF ingredients are based on the pH of the bulk MWF, different MWFs can be designed by altering the pH of the system with different concentrations of MWF concentration. Various combinations of these fluids can be tested to find minimum flux decline during microfiltration.

5.2.3 Externally-applied Membrane Electrostatic Forces

It was found via the enhanced fluid dynamic model that charges applied by trapped particles in the membrane caused a repelling force against incoming particles. This prevented certain pores from becoming blocked and resulted in lower flux decline. It would be interesting to experimentally test the effect of these electrostatic forces on a membrane without particles trapped.

The electrostatic forces must be applied to certain locations in the microfilter via an externally supplied source. Current tubular microfilter membranes are made from a sintering process after alumina particles have been already arranged into a desired shape. The same sintering process can be utilized to create the tube. To implement the electrostatic charges, a sheet metal cylinder with prongs sticking radially outwards can be used as the substrate on which the alumina particles are built into shape of the structure and sintered. The completed membrane can still be used in tubular cross-flow microfiltration applications, and now the electrostatic charge of the membrane can be altered via inducing an electric potential across the substrate and into the metallic prongs residing inside the microfilter. This can duplicate the effects of particle charges inside the microfilter.

List of References

[1] Zhao, F., Clarens, A., and Skerlos, S. J., 2006, "Optimization of Metalworking Fluid Microemulsion Surfactant Concentrations for Microfiltration Recycling," Environmental Science & Technology, 41(3), pp. 1016-1023.

[2] Rajagopalan, K., Rusk, T., and Dianovsky, M., 2004, "Purification of Semi-Synthetic Metalworking Fluids by Microfiltration," Tribology and Lubrication Technology, 60(Compendex), pp. 38-44.

[3] Ham, S., Wentz, J. E., Kapoor, S. G., 2010, "The Impact of Surface Forces on Particle Flow and Pore Blocking in the Microfiltration of Metalworking Fluids," Journal of Manufacturing Science and Engineering, 132(1), pp. 011006.1-9.

[4] Wentz, J. E., Kapoor, S. G., DeVor, R. E., 2005, "Experimental Investigation of Membrane Fouling due to Microfiltration of Semi-Synthetic Metalworking Fluids," Trans. NAMRI/SME, 33, pp. 8-281.

[5] Belfort, G., Davis, R. H., and Zydney, A. L., 1994, "The Behavior of Suspensions and Macromolecular Solutions in Crossflow Microfiltration," Journal of Membrane Science, 96(1-2), pp. 1-58.

[6] Skerlos, S. J., Rajagopalan, N., DeVor, R. E., 2000, "Ingredient-Wise Study of Flux Characteristics in the Ceramic Membrane Filtration of Uncontaminated Synthetic Metalworking Fluids, Part 2: Analysis of Underlying Mechanisms," Journal of Manufacturing Science & Engineering, 122(4), pp. 746-752.

[7] Skerlos, S. J., Rajagopalan, N., DeVor, R. E., 2000, "Ingredient-Wise Study of Flux Characteristics in the Ceramic Membrane Filtration of Uncontaminated Synthetic Metalworking Fluids, Part 1: Experimental Investigation of Flux Decline," Journal of Manufacturing Science & Engineering, 122(4), pp. 739-745.

[8] Kim, M., and Zydney, A. L., 2004, "Effect of Electrostatic, Hydrodynamic, and Brownian Forces on Particle Trajectories and Sieving in Normal Flow Filtration," Journal of Colloid and Interface Science, 269(2), pp. 425-431.

[9] Mahdi, S. M., and Sköld, R. O., 1991, "Experimental Study of Membrane Filtration for the Recycling of Synthetic Waterbased Metalworking Fluids," Tribology International, 24(6), pp. 389-395.

[10] Gilmer, J. A., Eppert, J. J., and Rajagopalan, N., 2005, "Formulation and Testing of a Microfiltration Compatible Synthetic Metalworking Fluid," Journal of Membrane Science, 256(1-2), pp. 18-28.

[11] Song, L., 1998, "Flux Decline in Crossflow Microfiltration and Ultrafiltration: Mechanisms and Modeling of Membrane Fouling," Journal of Membrane Science, 139(2), pp. 183-200.

[12] Zhao, F., Urbance, M., and Skerlos, S. J., 2004, "Mechanistic Model of Coaxial Microfiltration for Semi-Synthetic Metalworking Fluid Microemulsions," Journal of Manufacturing Science and Engineering, 126(3), pp. 435-444.

[13] Wentz, J. E., Kapoor, S. G., DeVor, R. E., 2008, "Dynamic Simulations of Alumina Membrane Fouling from Recycling of Semisynthetic Metalworking Fluids," Journal of Manufacturing Science and Engineering, 130(6), pp. 061015.1-11.

[14] Kim, M., and Zydney, A. L., 2005, "Particle-Particle Interactions during Normal Flow Filtration: Model Simulations," Chemical Engineering Science, 60(15), pp. 4073-4082.

[15] Ham, S., Wentz, J. E., Kapoor, S. G., and DeVor, R. E., (2011). "Three-Dimensional Fluid Dynamic Model for the Prediction of Microfiltration Membrane Fouling and Flux Decline," J. Manuf. Sci. Eng., 133(4), pp. 041001.1-8.

[16] Matsuura, T., 1994, "Synthetic membranes and membrane separation processes," CRC Press, Boca Raton, Florida.

[17] Hillie, T., and Hlophe, M., 2007, "Nanotechnology and the Challenge of Clean Water," Nat Nano, 2(11), pp. 663-664.

[18] Rajagopalan, N., Boddu, V. M., Mishra, S., 1998, "Pollution Prevention in an Aluminum Grinding Facility," Metal Finishing, 96(11), pp. 18-24.

[19] Mueller, J., Cen, Y., and Davis, R. H., 1997, "Crossflow Microfiltration of Oily Water," Journal of Membrane Science, 129(2), pp. 221-235.

[20] Crittenden, J., Trussell, R., Hand, D., 2005, "Water Treatment Principles and Design," John Wiley and Sons, New Jersey.

[21] Wentz, J. E., Kapoor, S. G., DeVor, R. E., 2007, "Development of a Novel Metalworking Fluid Engineered for use with Microfiltration Recycling," Journal of Tribology, 129(1), pp. 135-142.

[22] Skerlos, S. J., Rajagopalan, N., DeVor, R. E., 2001, "Microfiltration of Polyoxyalkylene Metalworking Fluid Lubricant Additives using Aluminum Oxide Membranes," Journal of Manufacturing Science and Engineering, 123(4), pp. 692-699.

[23] National Institute for Occupational Safety and Health, 1998, "What You Need to Know About Occupational Exposure to Metalworking Fluids," National Institute for Occupational Safety and Health.

[24] Groover, M.P., 2007, "Fundamentals of Modern Manufacturing: Materials, Processes, and Systems," J. Wiley & Sons, Hoboken, New Jersey.

[25] OSHA, 1999, "Metalworking Fluids: Safety and Health Best Practices Manual," U.S. Department of Labor, Occupational Safety and Health Administration, Salt Lake City.

[26] Byers, J.P., 2006, "Metalworking Fluids," CRC/Taylor & Francis, Boca Raton, Florida.

[27] Rudnick, L.R., and Shubkin, R.L., 1999, "Synthetic Lubricants and High-Performance Functional Fluids," CRC Press, New York.

[28] Wentz, J. E., Kapoor, S. G., DeVor, R. E., 2008, "Partial Pore Blocking in Microfiltration Recycling of a Semisynthetic Metalworking Fluid," Journal of Manufacturing Science and Engineering, 130(4), pp. 041014.1-9.

[29] Ansys Inc., 2009, "FLUENT User's Guide," Canonsburg, Pennsylvania.

[30] Israelachvili, J.N., 1991, "Intermolecular and Surface Forces," Academic Press, London, United Kingdom.

[31] Lyklema, H., 1991, "Fundamentals of Interface and Colloid Science," Academic Press.

[32] Gupta, A. K., Coelho, D., and Adler, P. M., 2007, "Influence of the Stern Layer on Electrokinetic Phenomena in Porous Media," Journal of Colloid and Interface Science, 316(1), pp. 140-159.

[33] Bowen, R. W., Filippov, A. N., Sharif, A. O., 1999, "Model of the Interaction between a Charged Particle and a Pore in a Charged Membrane Surface," Advances in Colloid and Interface Science, 81(1), pp. 35-72.

[34] Carnie, S. L., Chan, D. Y. C., and Stankovich, J., 1994, "Computation of Forces between Spherical Colloidal Particles: Nonlinear Poisson-Boltzmann Theory," Journal of Colloid and Interface Science, 165(1), pp. 116-128.

[35] Bhattacharjee, S., and Elimelech, M., 1997, "Surface Element Integration: A Novel Technique for Evaluation of DLVO Interaction between a Particle and a Flat Plate," Journal of Colloid and Interface Science, 193(2), pp. 273-285.

[36] Bhattacharjee, S., Chen, J. Y., and Elimelech, M., 2000, "DLVO Interaction Energy between Spheroidal Particles and a Flat Surface," Colloids and Surfaces A: Physicochemical and Engineering Aspects, 165(1-3), pp. 143-156.

[37] Bhattacharjee, S., Elimelech, M., and Borkovec, M., 1998, "DLVO Interaction between Colloidal Particles: Beyond Derjaguin's Approximation," Croatica Chemica Acta, 71(4), pp. 883-903.

[38] Tabor, D., and Winterton, R. H. S., 1969, "The Direct Measurement of Normal and Retarded Van Der Waals Forces," Proceedings of the Royal Society of London.Series A, Mathematical and Physical Sciences, 312(1511), pp. 435-450.

[39] Madou, J. M., 2002, "Fundamentals of Microfabrication: The Science of Miniaturization," CRC Press, Boca Raton, Florida.

[40] Ounis, H., Ahmadi, G., and McLaughlin, J. B., 1991, "Brownian Diffusion of Submicrometer Particles in the Viscous Sublayer," Journal of Colloid and Interface Science, 143(1), pp. 266-277.

[41] Yopps, J. A., and Fuerstenau, D. W., 1964, "The Zero Point of Charge of Alpha-Alumina," Journal of Colloid Science, 19(1), pp. 61-71.

[42] Inkson, B. J., Wu, H. Z., Steer, T., 2001, "3D Mapping of Subsurface Cracks in Alumina using FIB," Materials Research Society (Symposia Proceedings), 649, pp. 6-Q7.7.1.

[43] Nagata, N., Herouvis, K. J., Dziewulski, D. M., 1989, "Cross-Flow Membrane Microfiltration of a Bacteriol Fermentation Broth," Biotechnology and Bioengineering, 34(4), pp. 447-466.

[44] Gregory, J., 1975, "Interaction of Unequal Double Layers at Constant Charge," Journal of Colloid and Interface Science, 51(1), pp. 44-51.

[45] Kirby, B., 2010, "Micro- and Nanoscale Fluid Mechanics: Transport in Microfluidic Devices," Cambridge University Press, Cambridge.

[46] Solcová, O., Snajdaufová, H., and Schneider, P., 2003, "Liquid-Expulsion Perm-Porometry for Characterization of Porous Solids," Microporous and Mesoporous Materials, 65(2-3), pp. 209-217.

[47] DeVor, R.E., Chang, T.H., and Sutherland, J.W., 2007, "Statistical Quality Design and Control, Second Edition," Pearson Prentice Hall, Saddle River, New Jersey.

Appendix A

Images of the Microfilter from the Focused Ion Beam

A.1 Pore Geometry One

The figures show consecutive images of a sliced microfilter pore geometry, deemed geometry one, from the focused ion beam.

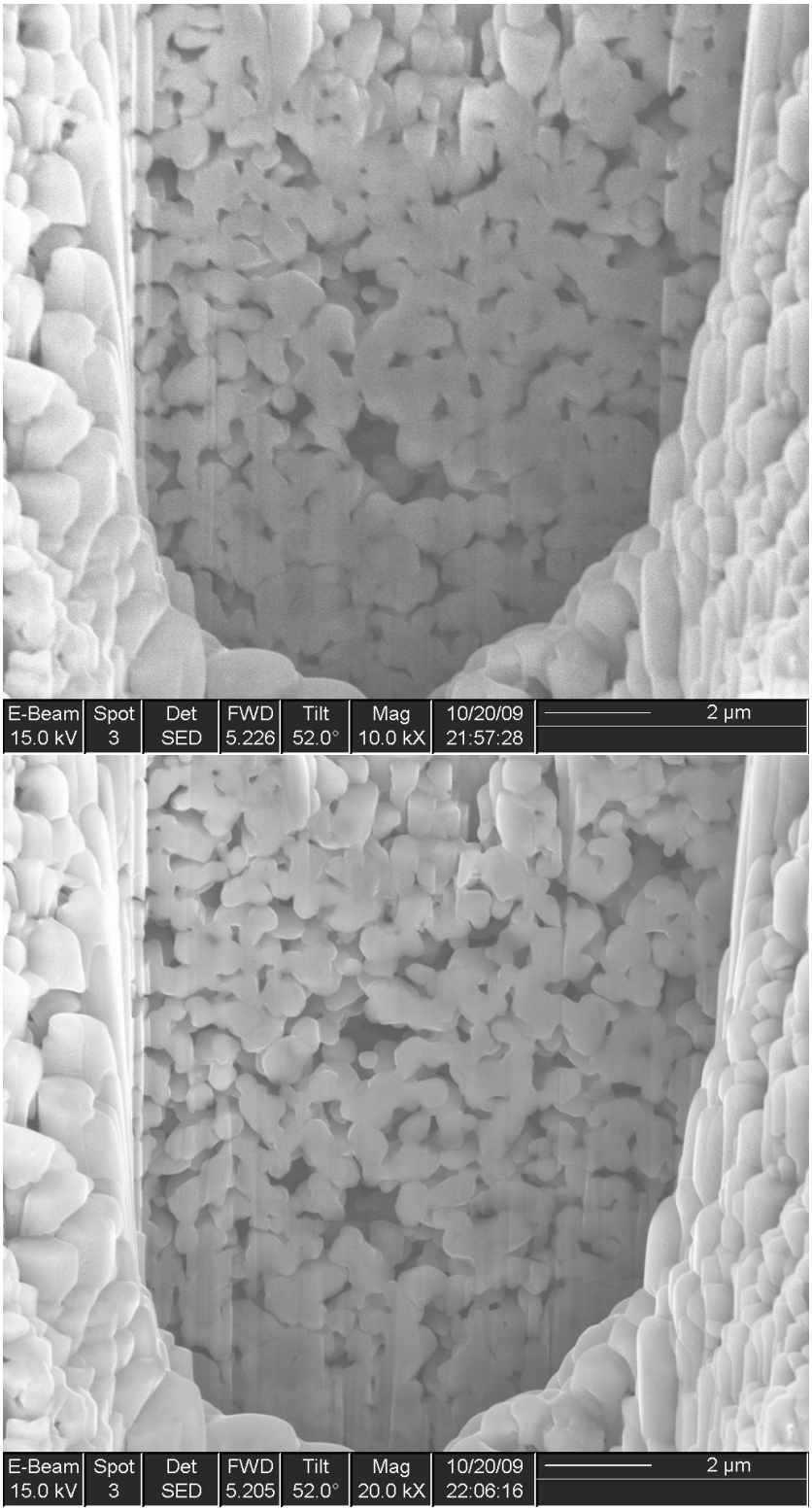

Figure A.1 - Slices 1 and 2 of Microfilter Pore Geometry 1

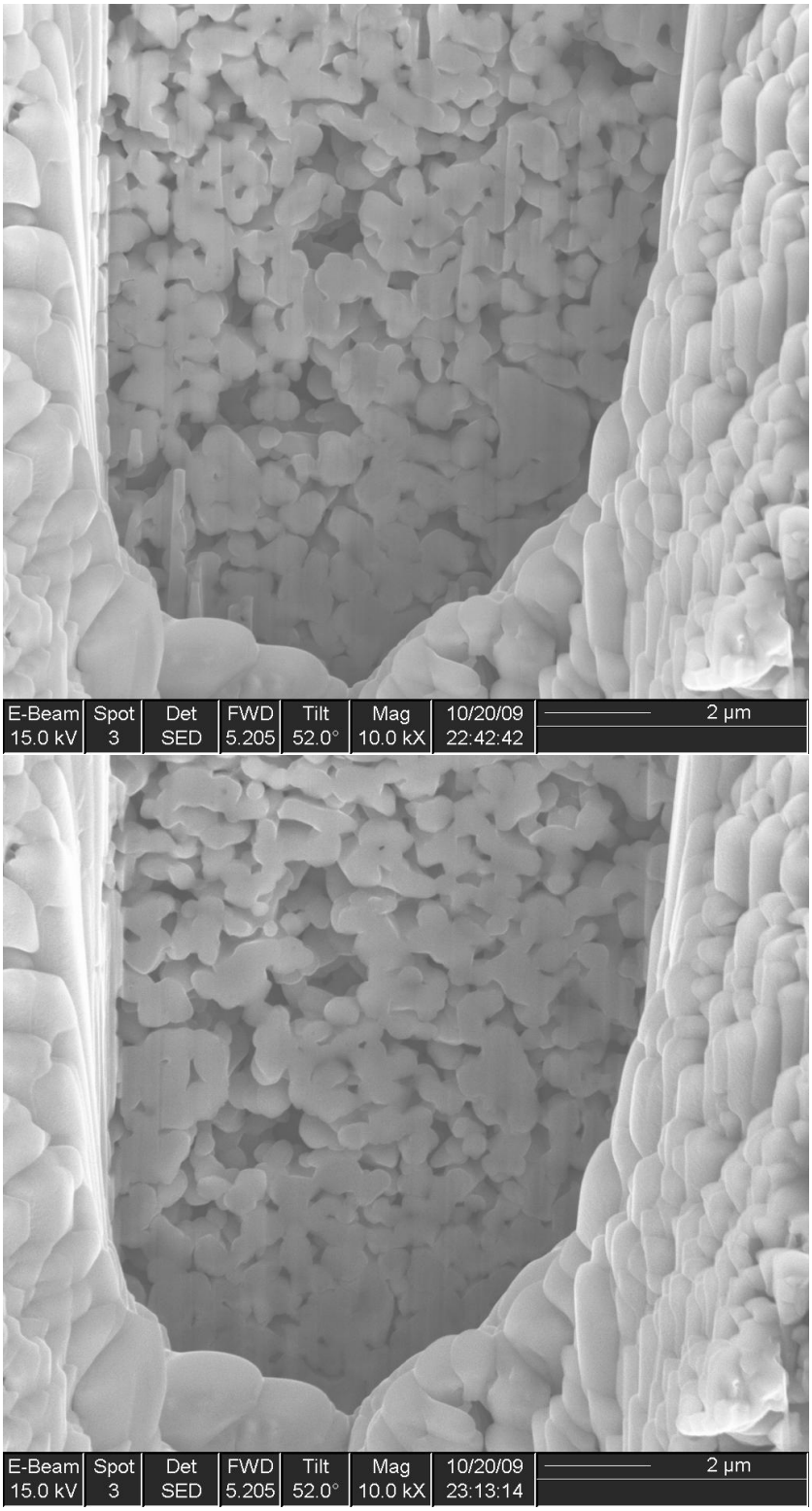

Figure A.2 - Slices 3 and 4 of Microfilter Pore Geometry 1

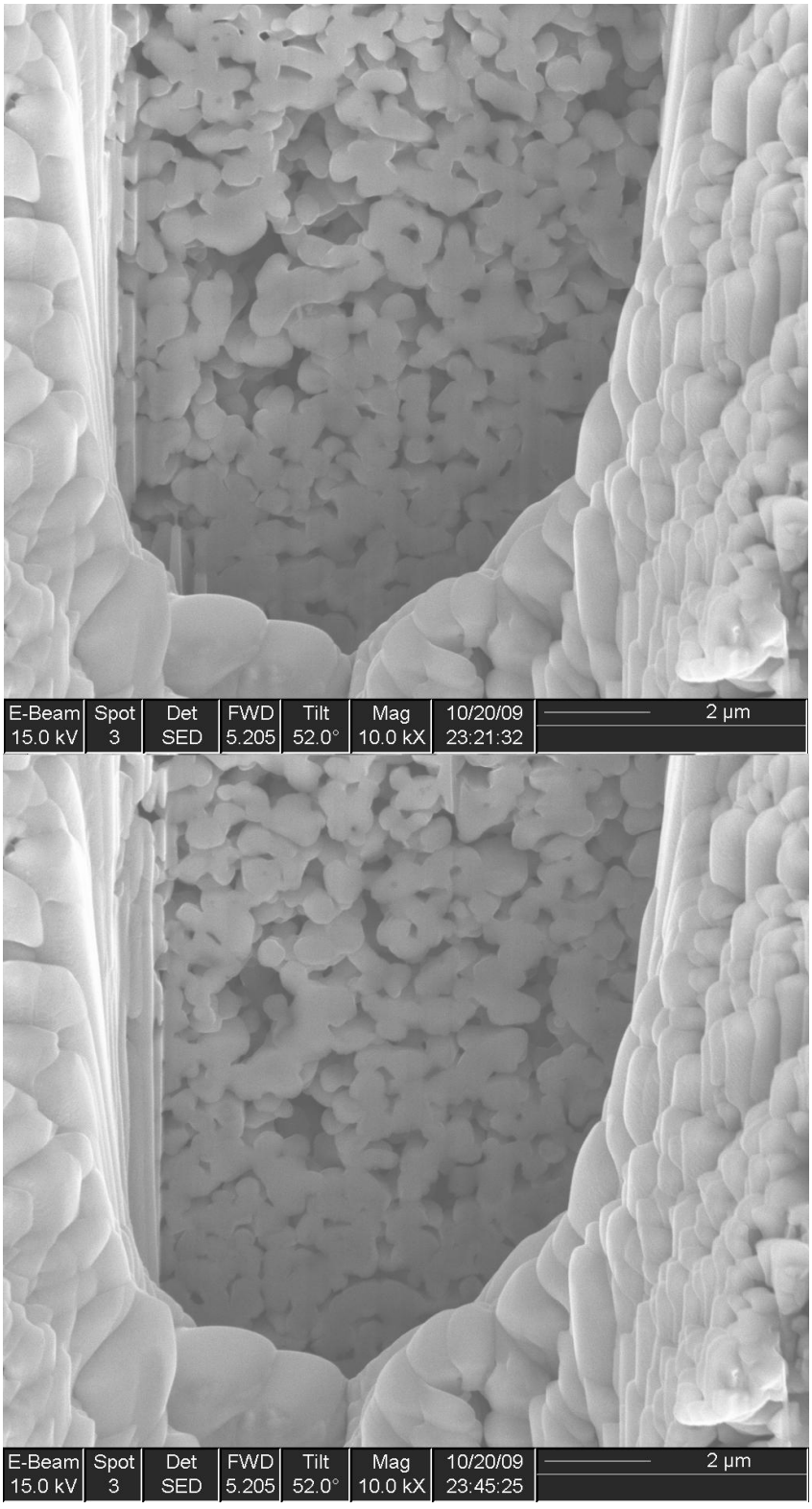

Figure A.3 - Slices 5 and 6 of Microfilter Pore Geometry 1

A.2 Pore Geometry Two

The figures show consecutive images of a sliced microfilter pore geometry, deemed geometry one, from the focused ion beam.

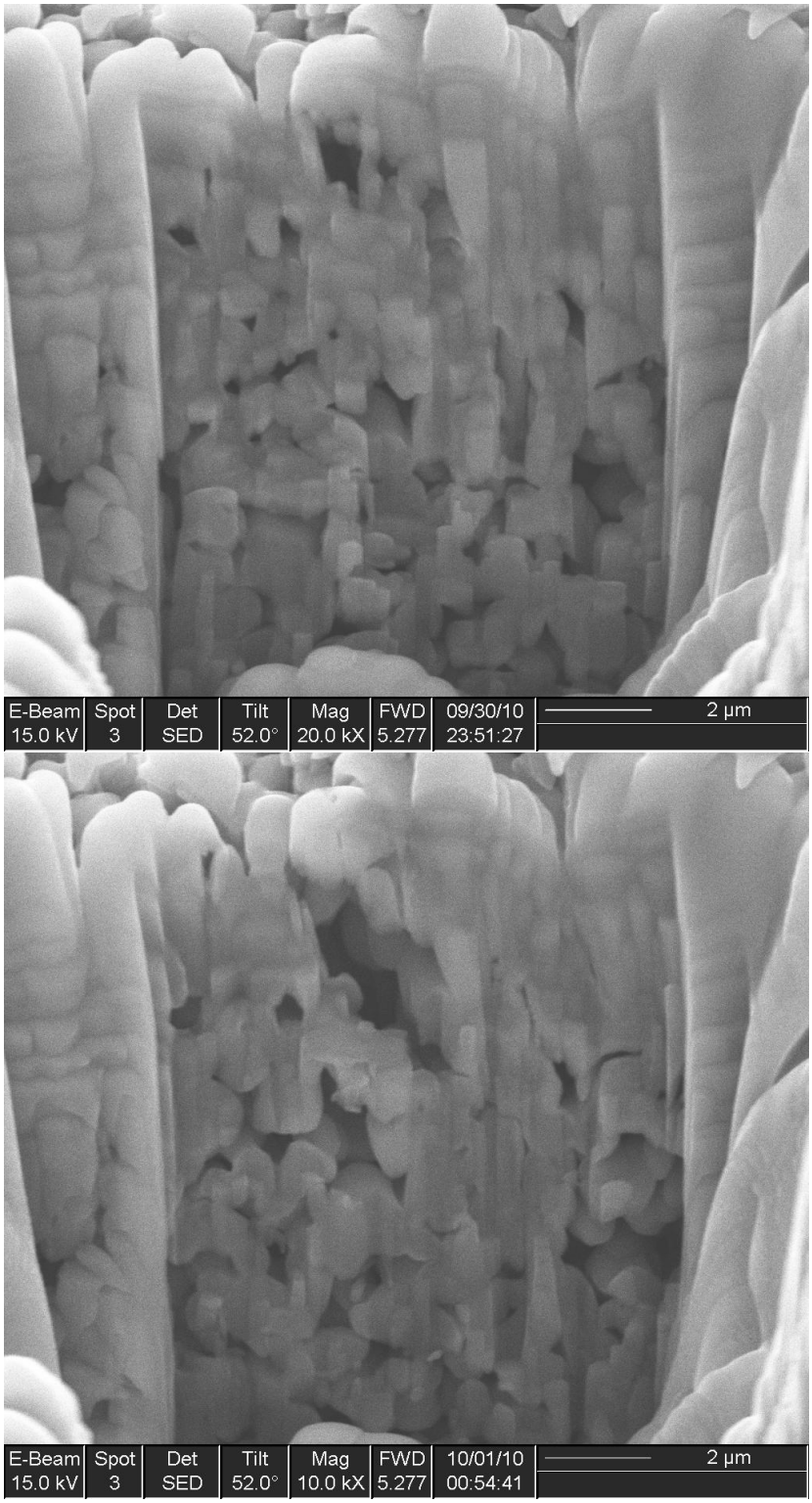

Figure A.4 - Slices 1 and 2 of Microfilter Pore Geometry 2

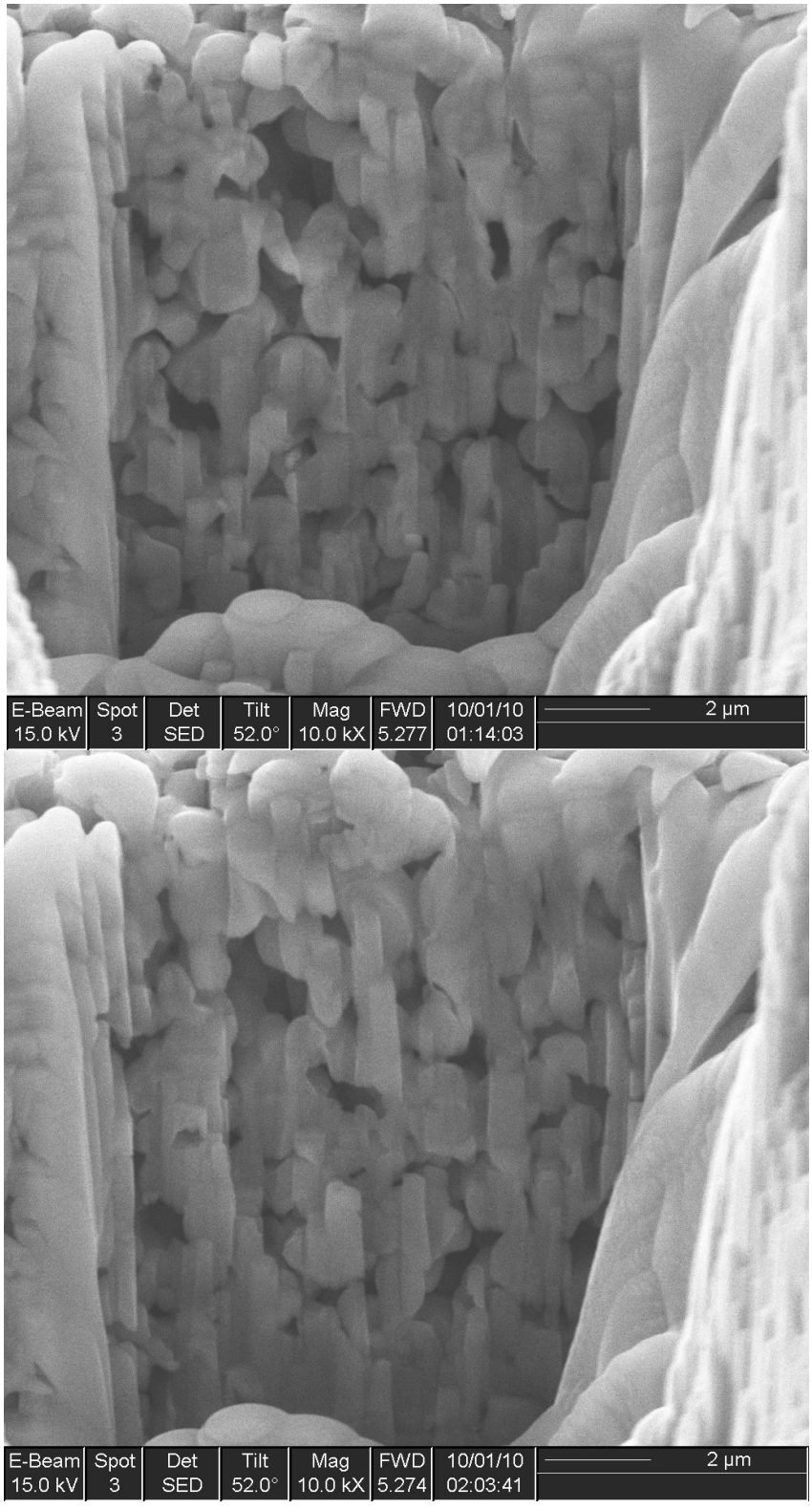

Figure A.5 - Slices 3 and 4 of Microfilter Pore Geometry 2

Appendix B

Recreated Tortuous Three-dimensional Pore Geometries

B.1 Pore Geometry One

The figures show the first of two three-dimensional pore geometry recreated from consecutive images of slices of the microfilter taken by the focused ion beam.

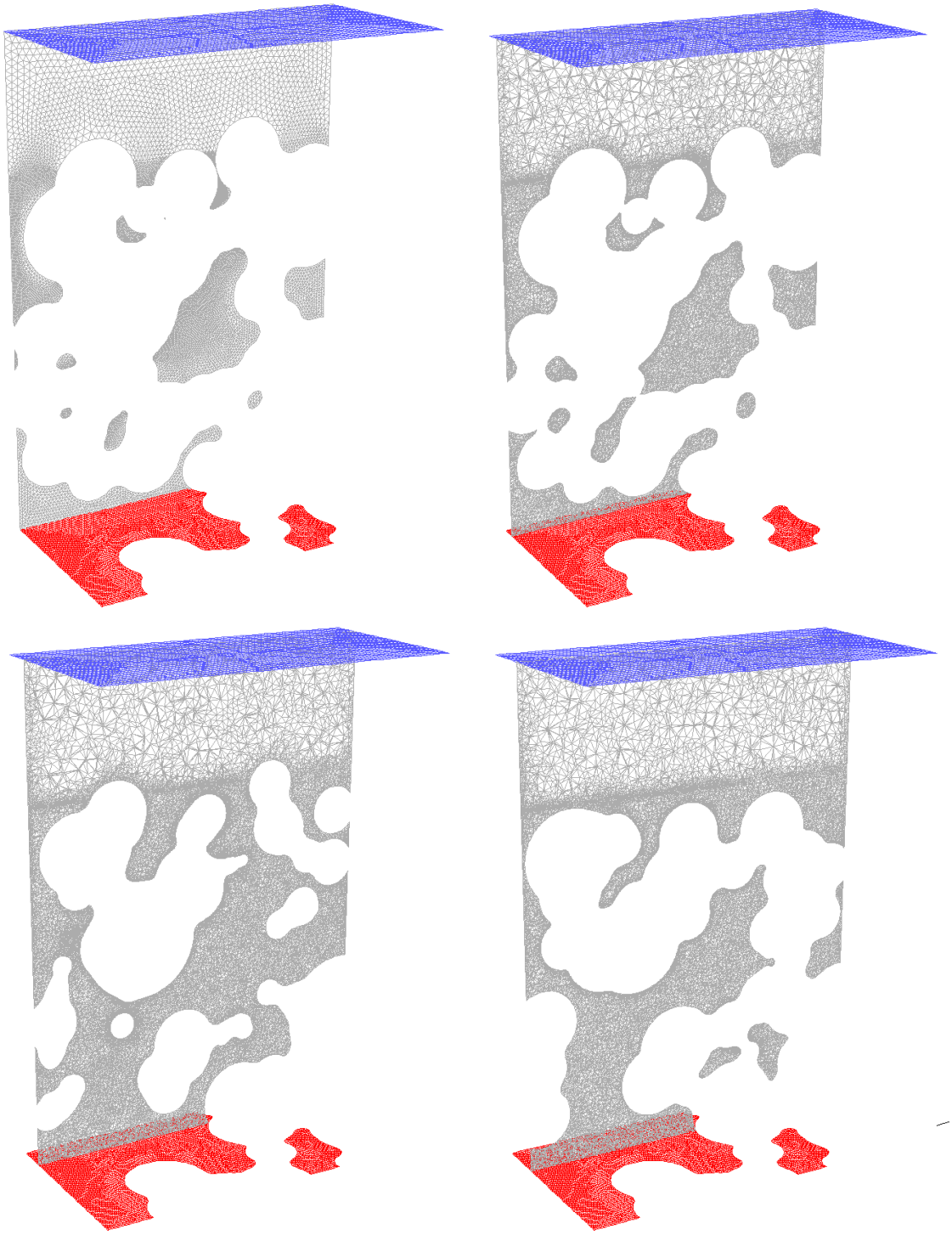

Figure B.1 - Cross-sections 1-4 of Geometry 1

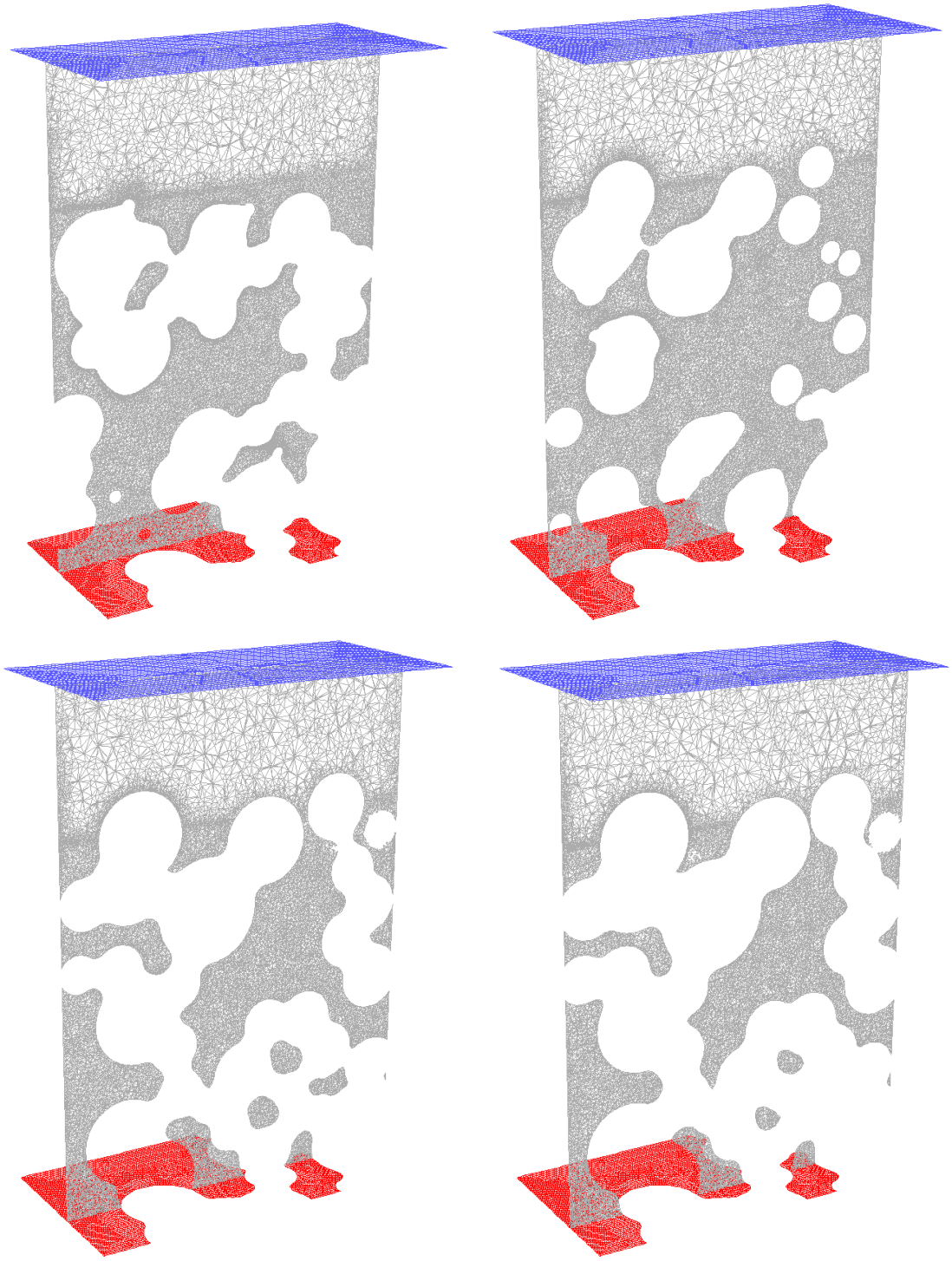

Figure B.2 - Cross-sections 5-8 of Geometry 1

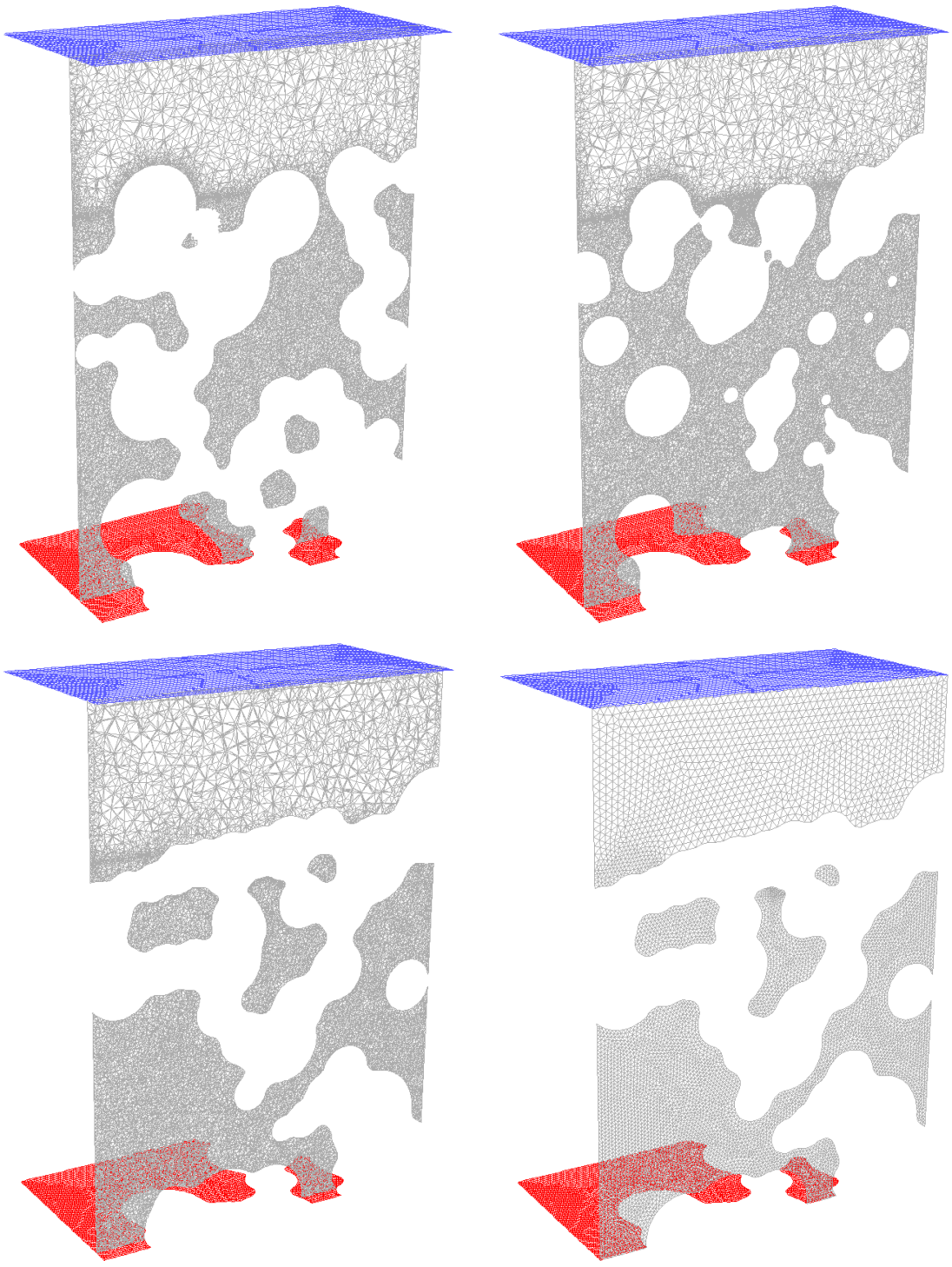

Figure B.3 - Cross-sections 9-12 of Geometry 1

B.2 Pore Geometry Two

The figures show the second of two three-dimensional pore geometry recreated from consecutive images of slices of the microfilter taken by the focused ion beam.

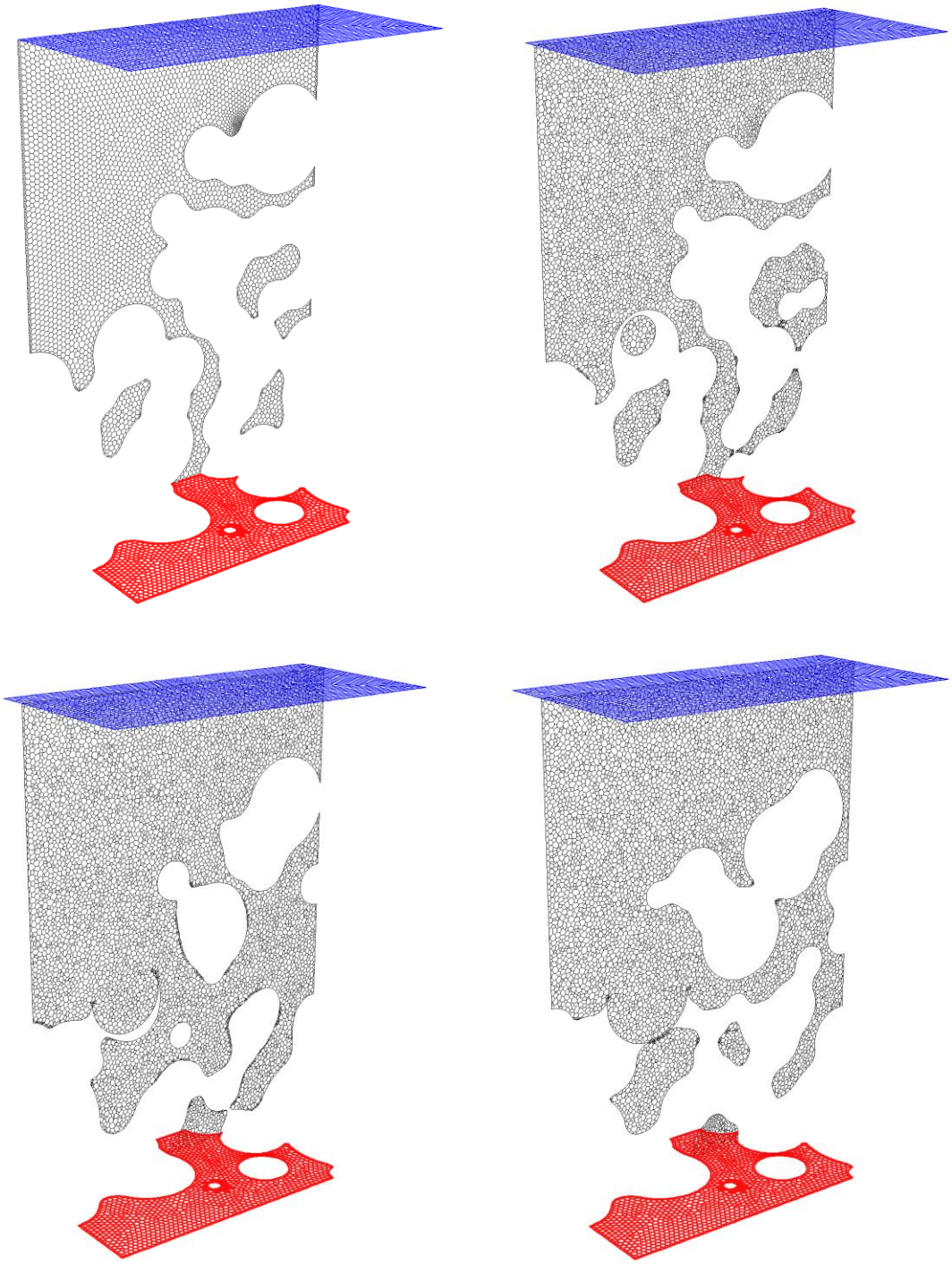

Figure B.4 - Cross-sections 1-4 of Geometry 2

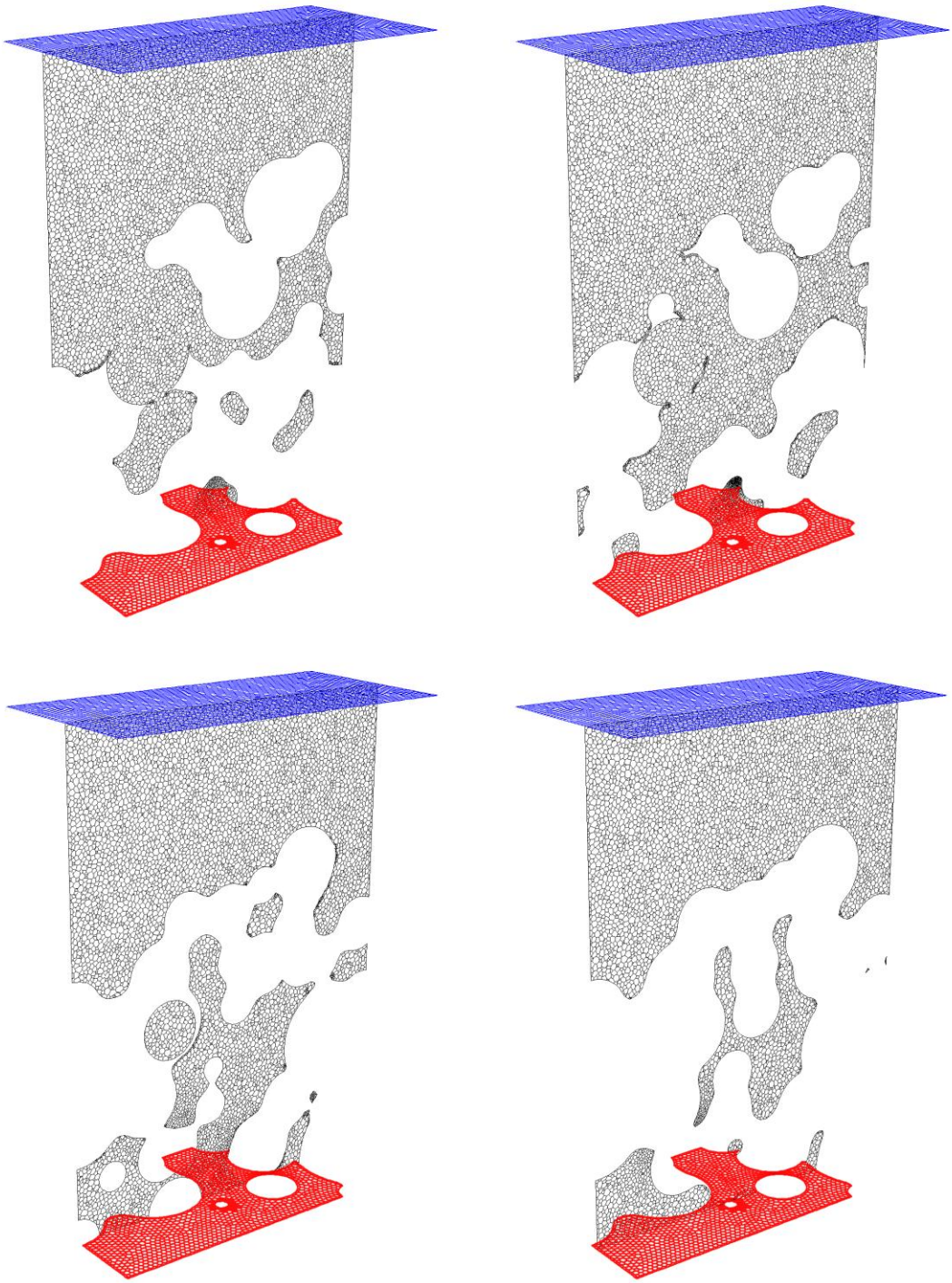

Figure B.5 - Cross-sections 5-8 of Geometry 2

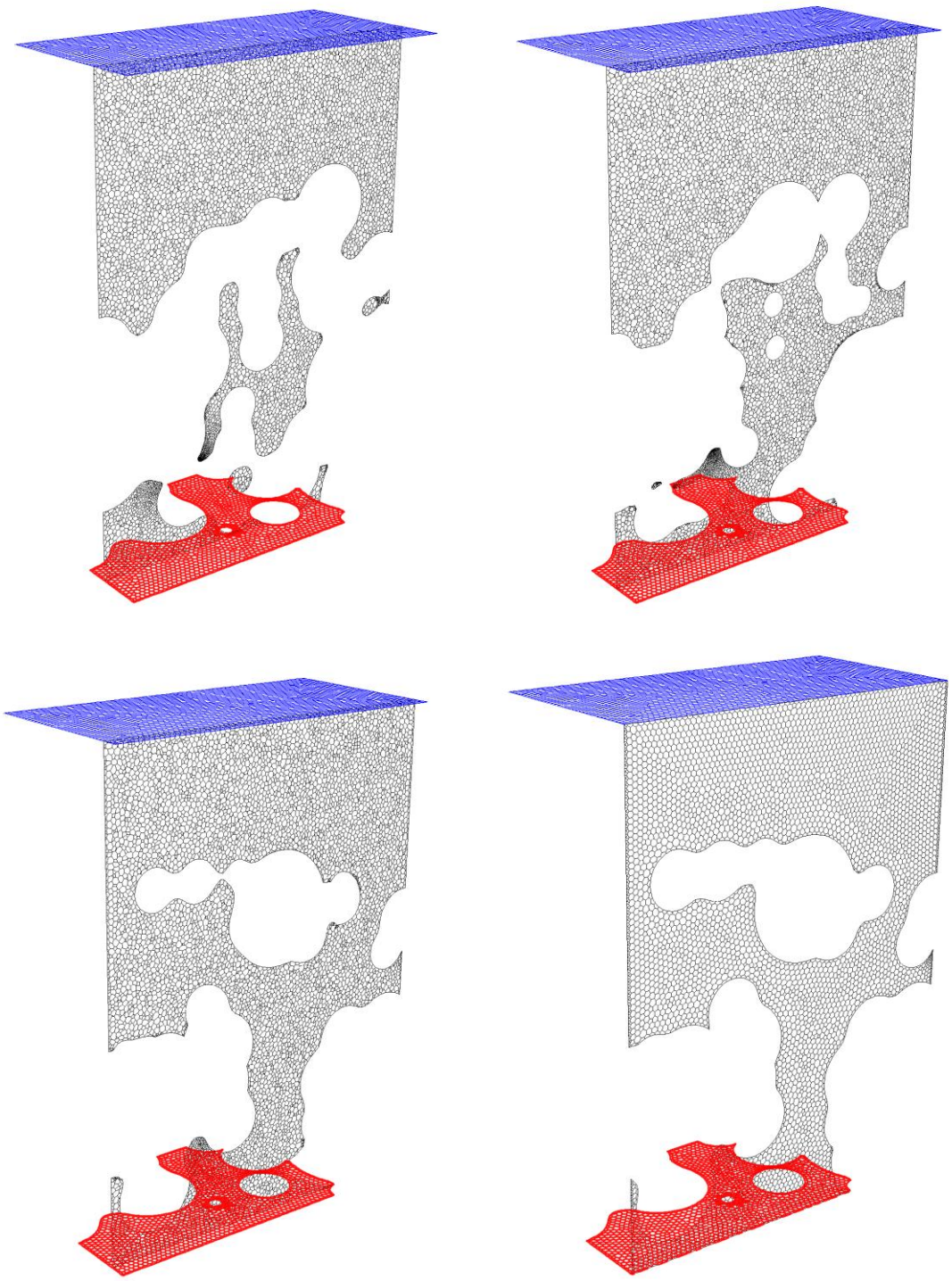

Figure B.6 - Cross-sections 9-12 of Geometry 2

Appendix C

Particle Injection Parameter Values for the Simulations of Varying In-use Time Particle Size Distributions

Particles were injected from a 1.5 μm by 3.0 μm (x-axis and z-axis, respectively) pressure inlet which is located at a y-value of 4.1 μm in the tortuous pore geometry.

The table of particles injected into the geometry for the simulation of the *used* MWF particle size distributions is shown in Table C.1.

Table C.1 - Particle Injection Parameters for the *Used* MWF Particle Size Distribution

Particle Number	Particle Diameter [um]	Injection Location [um]			Penetration Depth [um]	% Loss in Flux [-]
		X	Y	Z		
1	0.350	1.01	4.10	0.61	0.7	0.0%
2	0.275	1.04	4.10	1.94	0.3	11.5%
3	0.150	0.95	4.10	0.75	0.0	0.0%
4	0.175	0.51	4.10	2.30	0.2	4.6%
5	0.400	0.35	4.10	0.49	0.0	0.0%
6	0.300	0.99	4.10	1.14	-0.2	0.0%
7	0.275	0.43	4.10	2.29	-0.1	0.0%
8	0.350	0.85	4.10	2.43	-0.2	0.0%
9	0.250	0.93	4.10	0.48	0.0	0.0%
10	0.200	1.12	4.10	1.43	3.0	0.0%
11	0.400	1.15	4.10	2.13	-0.4	0.0%
12	0.150	0.39	4.10	1.06	0.4	1.1%
13	0.200	0.88	4.10	0.59	3.0	0.0%
14	0.475	1.00	4.10	0.49	-0.1	0.0%
15	0.200	1.03	4.10	1.66	0.2	5.7%
16	0.175	0.74	4.10	1.44	-0.3	0.0%
17	0.425	0.94	4.10	1.74	3.0	0.0%
18	0.500	0.62	4.10	2.41	3.0	0.0%
19	0.500	0.85	4.10	2.21	0.1	0.0%
20	0.350	1.04	4.10	0.97	-0.1	0.0%
21	0.175	0.40	4.10	1.98	-0.5	0.0%
22	0.200	1.16	4.10	2.47	-0.3	0.0%
23	0.450	0.80	4.10	1.32	0.2	2.7%
24	0.550	0.44	4.10	1.25	0.3	2.3%
25	0.375	1.15	4.10	1.87	0.2	1.4%
26	0.350	0.85	4.10	2.65	-0.4	0.0%
27	0.175	0.99	4.10	2.33	-0.4	0.0%
28	0.200	0.60	4.10	2.02	-0.2	0.0%
29	0.225	1.16	4.10	0.30	-0.5	0.0%
30	0.175	0.57	4.10	1.56	-0.1	0.0%
31	0.525	0.40	4.10	2.64	-0.1	0.0%
32	0.525	0.35	4.10	2.02	-0.3	0.0%
33	0.325	0.72	4.10	2.21	-0.1	0.0%
34	0.175	0.82	4.10	2.48	-0.2	0.0%
35	0.375	0.67	4.10	2.48	-0.6	0.0%
36	0.425	0.82	4.10	2.49	-0.8	0.0%
37	0.275	0.70	4.10	1.62	-0.6	0.0%
38	0.300	1.00	4.10	0.59	-0.8	0.0%

Table C.1 (cont.)

39	0.500	0.48	4.10	1.18	-0.3	0.0%
40	0.550	0.63	4.10	1.41	-0.6	0.0%
41	0.250	0.45	4.10	0.78	-0.7	0.0%
42	0.250	1.14	4.10	1.52	-0.6	0.0%
43	0.200	0.53	4.10	0.48	0.3	1.7%
44	0.350	0.73	4.10	0.49	0.1	0.1%
45	0.375	0.99	4.10	2.04	-0.7	0.0%
46	0.150	1.04	4.10	2.26	3.0	0.0%

The table of particles injected into the geometry for the simulation of the *semi-used* MWF particle size distributions is shown in Table C.2.

Table C.2 - Particle Injection Parameters for the *Semi-Used* MWF Particle Size Distribution

Particle Number	Particle Diameter [um]	Injection Location [um]			Penetration Depth [um]	% Loss in Flux [-]
		X	Y	Z		
1	0.175	0.70	4.10	1.48	3.0	0.0%
2	0.100	0.93	4.10	1.40	3.0	0.0%
3	0.100	0.62	4.10	1.94	0.2	0.0%
4	0.325	1.05	4.10	2.12	3.0	0.0%
5	0.050	0.72	4.10	2.64	0.3	0.0%
6	0.275	0.58	4.10	1.58	0.4	4.8%
7	0.300	0.64	4.10	0.32	0.4	0.0%
8	0.125	0.99	4.10	0.66	0.1	0.0%
9	0.250	0.47	4.10	1.13	0.6	0.0%
10	0.100	0.55	4.10	1.46	0.9	0.0%
11	0.100	1.13	4.10	0.53	0.0	0.0%
12	0.250	1.14	4.10	0.61	3.0	0.0%
13	0.100	0.56	4.10	1.08	0.2	0.0%
14	0.250	0.37	4.10	1.48	3.0	0.0%
15	0.075	0.33	4.10	2.38	0.4	0.0%
16	0.125	0.52	4.10	0.65	0.1	0.0%
17	0.125	0.93	4.10	1.00	0.7	0.0%

Table C.2 (cont.)

18	0.200	0.54	4.10	0.36	0.2	0.0%
19	0.100	0.88	4.10	0.80	0.3	0.0%
20	0.125	0.96	4.10	0.59	3.0	0.0%
21	0.125	1.19	4.10	1.21	0.3	0.0%
22	0.125	1.04	4.10	0.31	-0.7	0.0%
23	0.100	0.89	4.10	2.02	3.0	0.0%
24	0.050	0.95	4.10	2.09	0.0	0.0%
25	0.200	1.04	4.10	1.75	0.3	4.6%
26	0.250	0.98	4.10	1.51	0.1	0.0%
27	0.250	0.31	4.10	1.55	0.1	0.0%
28	0.250	0.41	4.10	1.14	3.0	0.0%
29	0.100	0.90	4.10	2.59	0.3	3.3%
30	0.250	0.43	4.10	1.20	3.0	0.0%
31	0.050	0.90	4.10	1.94	3.0	0.0%
32	0.050	1.10	4.10	0.62	0.2	1.8%
33	0.250	1.12	4.10	2.50	0.4	0.0%
34	0.175	0.60	4.10	1.03	3.0	0.0%
35	0.050	0.85	4.10	1.90	0.7	0.0%
36	0.100	0.46	4.10	0.39	0.5	0.0%
37	0.200	0.81	4.10	0.60	1.0	0.0%
38	0.350	0.47	4.10	2.54	3.0	0.0%
39	0.150	0.86	4.10	2.15	0.1	0.0%
40	0.325	0.66	4.10	1.72	-0.1	0.0%
41	0.300	1.15	4.10	0.81	0.3	3.7%
42	0.225	1.18	4.10	0.82	0.1	0.0%
43	0.150	0.89	4.10	1.55	0.1	0.0%
44	0.350	0.58	4.10	1.47	3.0	0.0%
45	0.050	0.37	4.10	2.46	0.9	0.0%
46	0.225	0.59	4.10	1.70	3.0	0.0%
47	0.050	0.75	4.10	0.66	3.0	0.0%
48	0.100	0.80	4.10	2.67	0.5	0.0%
49	0.250	0.67	4.10	0.89	3.0	0.0%
50	0.075	0.79	4.10	2.51	3.0	0.0%
51	0.050	0.31	4.10	1.13	-0.2	0.0%
52	0.400	0.50	4.10	1.39	3.0	0.0%
53	0.050	0.79	4.10	0.71	3.0	0.0%
54	0.050	0.51	4.10	2.30	0.1	0.0%
55	0.125	0.82	4.10	1.59	0.3	1.5%
56	0.2	1.01	4.10	0.47	0.3	5.1%
57	0.25	1.03	4.10	0.35	3.0	0.0%
58	0.05	0.97	4.10	1.08	3.0	0.0%

Table C.2 (cont.)

59	0.05	0.33	4.10	1.32	0.2	3.8%
60	0.3	0.78	4.10	2.69	0.1	0.0%
61	0.2	0.87	4.10	0.53	0.5	0.0%
62	0.1	0.74	4.10	0.81	0.4	0.0%
63	0.075	0.31	4.10	2.41	3.0	0.0%
64	0.05	0.74	4.10	1.74	0.6	0.0%
65	0.225	0.98	4.10	0.49	0.0	0.0%
66	0.25	0.43	4.10	0.97	0.0	0.0%
67	0.325	0.33	4.10	0.72	-0.2	0.0%
68	0.4	0.45	4.10	1.06	3.0	0.0%
69	0.05	0.36	4.10	1.49	-0.1	0.0%
70	0.275	0.99	4.10	1.25	3.0	0.0%
71	0.05	0.83	4.10	2.63	3.0	0.0%
72	0.05	0.38	4.10	2.09	0.1	0.0%
73	0.275	1.11	4.10	0.32	3.0	0.0%
74	0.1	0.73	4.10	2.65	0.0	0.0%
75	0.175	0.34	4.10	1.19	-0.1	0.0%
76	0.1	1.15	4.10	1.83	0.7	0.0%
77	0.1	0.37	4.10	0.54	-0.2	0.0%
78	0.3	1.18	4.10	1.36	3.0	0.0%
79	0.2	0.91	4.10	1.91	3.0	0.0%
80	0.075	0.98	4.10	2.49	0.1	0.0%
81	0.075	1.12	4.10	0.62	3.0	0.0%
82	0.05	0.89	4.10	0.98	0.1	0.0%
83	0.1	0.93	4.10	1.36	0.0	0.0%
84	0.15	0.67	4.10	1.84	0.0	0.0%
85	0.1	0.54	4.10	1.27	0.0	0.0%
86	0.1	0.73	4.10	1.78	-0.2	0.0%
87	0.075	1.06	4.10	1.10	-0.1	0.0%
88	0.25	0.94	4.10	1.15	-0.3	0.0%
89	0.2	1.16	4.10	1.48	0.3	0.4%
90	0.075	0.35	4.10	2.43	3.0	0.0%
91	0.125	0.59	4.10	2.09	-0.1	0.0%
92	0.1	0.45	4.10	1.25	0.0	0.0%
93	0.075	0.68	4.10	1.19	3.0	0.0%
94	0.15	0.79	4.10	2.26	3.0	0.0%
95	0.05	0.42	4.10	2.28	0.4	0.0%
96	0.175	0.60	4.10	0.34	3.0	0.0%
97	0.075	1.01	4.10	0.54	-0.1	0.0%
98	0.15	0.95	4.10	1.25	-0.1	0.0%
99	0.225	0.71	4.10	1.14	3.0	0.0%

Table C.2 (cont.)

100	0.1	1.09	4.10	2.16	3.0	0.0%
101	0.05	0.41	4.10	0.43	0.1	0.0%
102	0.275	0.35	4.10	2.01	0.5	0.0%
103	0.1	0.70	4.10	1.82	0.1	0.0%
104	0.175	0.97	4.10	1.36	0.1	0.0%
105	0.2	0.65	4.10	0.64	1.0	0.0%
106	0.15	0.37	4.10	2.64	0.1	0.0%
107	0.15	0.40	4.10	0.79	-0.3	0.0%
108	0.175	1.13	4.10	1.51	-0.1	0.0%
109	0.3	1.19	4.10	0.59	-0.2	0.0%
110	0.325	0.55	4.10	0.80	0.1	0.0%
111	0.05	1.12	4.10	0.45	0.9	0.0%
112	0.05	0.35	4.10	0.30	2.3	0.0%
113	0.05	0.92	4.10	1.55	2.0	0.0%
114	0.1	1.04	4.10	2.14	-0.3	0.0%
115	0.15	1.03	4.10	1.51	-0.1	0.0%
116	0.075	0.82	4.10	1.67	0.1	0.0%
117	0.1	0.37	4.10	0.76	-0.1	0.0%
118	0.2	0.79	4.10	0.48	-0.1	0.0%
119	0.15	0.78	4.10	1.93	-0.1	0.0%
120	0.1	0.92	4.10	1.71	0.0	0.0%
121	0.075	0.84	4.10	1.54	-0.4	0.0%
122	0.2	0.94	4.10	1.79	-0.2	0.0%
123	0.35	0.35	4.10	1.03	0.3	0.4%
124	0.15	0.33	4.10	2.54	1.6	0.0%
125	0.05	0.33	4.10	2.35	-0.1	0.0%
126	0.15	0.67	4.10	1.52	-0.4	0.0%
127	0.3	0.63	4.10	0.77	0.3	3.6%
128	0.25	1.00	4.10	2.47	-0.3	0.0%
129	0.2	0.81	4.10	1.70	-0.2	0.0%
130	0.075	0.36	4.10	0.99	-0.3	0.0%
131	0.225	1.03	4.10	1.52	0.4	6.4%
132	0.275	0.34	4.10	0.70	-0.3	0.0%
133	0.075	1.14	4.10	2.50	-0.2	0.0%
134	0.15	0.59	4.10	1.62	-0.1	0.0%
135	0.1	1.09	4.10	1.33	0.0	0.0%
136	0.1	0.95	4.10	1.25	-0.4	0.0%
137	0.075	0.61	4.10	1.01	-0.3	0.0%
138	0.15	0.94	4.10	1.58	0.3	1.8%
139	0.15	0.31	4.10	0.63	3.0	0.0%
140	0.05	1.06	4.10	1.93	-0.1	0.0%

Table C.2 (cont.)

141	0.1	0.51	4.10	1.91	-0.3	0.0%
142	0.15	0.82	4.10	1.97	0.5	0.0%
143	0.175	0.40	4.10	2.49	-0.4	0.0%
144	0.1	1.18	4.10	2.08	-0.6	0.0%
145	0.325	1.01	4.10	1.44	0.0	0.0%
146	0.1	0.84	4.10	1.21	-0.1	0.0%
147	0.125	0.84	4.10	2.43	0.4	0.0%
148	0.05	0.83	4.10	2.11	-0.1	0.0%
149	0.1	0.34	4.10	1.20	0.3	1.6%
150	0.175	0.85	4.10	0.42	-0.1	0.0%
151	0.1	0.89	4.10	2.03	-0.4	0.0%
152	0.15	0.92	4.10	1.60	0.0	0.0%
153	0.225	0.39	4.10	2.54	-0.2	0.0%
154	0.2	0.83	4.10	1.86	-0.2	0.0%
155	0.125	1.10	4.10	2.62	1.8	0.0%
156	0.05	0.58	4.10	1.53	0.4	1.3%
157	0.2	1.01	4.10	0.50	-0.4	0.0%
158	0.275	0.53	4.10	1.19	0.0	0.0%
159	0.1	0.43	4.10	2.27	-0.4	0.0%
160	0.25	0.83	4.10	1.61	1.1	0.0%
161	0.05	0.77	4.10	2.70	-0.1	0.0%
162	0.075	0.63	4.10	2.15	0.0	0.0%
163	0.175	0.59	4.10	2.59	2.1	0.0%
164	0.075	1.15	4.10	1.79	-0.1	0.0%
165	0.225	1.07	4.10	0.90	0.3	3.1%
166	0.175	1.16	4.10	0.47	0.4	0.0%

The table of particles injected into the geometry for the simulation of the *new* MWF particle size distributions is shown in Table C.3.

Table C.3 - Particle Injection Parameters for the *New* MWF Particle Size Distribution

Particle Number	Particle Diameter [um]	Injection Location [um]			Penetration Depth [um]	% Loss in Flux [-]
		X	Y	Z		
1	0.050	0.81	4.10	1.89	0.5	0.1%
2	0.200	0.69	4.10	0.97	1.6	0.0%
3	0.125	0.42	4.10	0.91	0.3	0.0%
4	0.125	0.98	4.10	2.13	0.8	0.0%
5	0.175	0.82	4.10	1.09	1.5	0.0%
6	0.150	1.08	4.10	1.16	0.3	0.0%
7	0.200	1.13	4.10	1.16	0.0	0.0%
8	0.050	0.80	4.10	1.76	0.0	0.0%
9	0.125	0.94	4.10	1.69	1.0	0.0%
10	0.075	0.61	4.10	2.59	-0.2	0.0%
11	0.050	1.03	4.10	1.56	3.0	0.0%
12	0.050	0.56	4.10	1.95	1.3	0.0%
13	0.125	0.39	4.10	2.23	-0.1	0.0%
14	0.175	0.65	4.10	2.07	0.1	0.0%
15	0.050	0.92	4.10	1.69	3.0	0.0%
16	0.225	0.83	4.10	2.23	0.2	0.0%
17	0.050	1.00	4.10	2.22	3.0	0.0%
18	0.200	0.58	4.10	1.38	0.2	0.0%
19	0.050	0.33	4.10	0.47	3.0	0.0%
20	0.100	0.75	4.10	0.46	3.0	0.0%
21	0.150	1.18	4.10	1.30	0.1	0.0%
22	0.050	0.82	4.10	1.33	3.0	0.0%
23	0.050	0.73	4.10	2.64	3.0	0.0%
24	0.150	1.09	4.10	1.50	0.5	0.8%
25	0.050	0.86	4.10	2.11	3.0	0.0%
26	0.075	0.49	4.10	2.13	3.0	0.0%
27	0.100	0.72	4.10	2.49	3.0	0.0%
28	0.150	1.16	4.10	2.06	0.3	0.0%
29	0.050	0.67	4.10	1.62	3.0	0.0%
30	0.100	0.36	4.10	1.43	3.0	0.0%
31	0.075	0.86	4.10	1.63	3.0	0.0%
32	0.100	0.42	4.10	1.65	0.6	0.0%
33	0.050	1.07	4.10	1.11	3.0	0.0%
34	0.125	0.71	4.10	1.95	0.5	0.5%
35	0.125	0.40	4.10	1.46	3.0	0.0%
36	0.050	0.94	4.10	1.93	3.0	0.0%
37	0.100	0.44	4.10	2.15	3.0	0.0%
38	0.125	0.63	4.10	2.44	3.0	0.0%

Table C.3 (cont.)

39	0.100	0.60	4.10	2.34	3.0	0.0%
40	0.150	0.82	4.10	2.00	0.5	1.2%
41	0.100	1.02	4.10	1.85	0.1	0.0%
42	0.050	0.94	4.10	1.50	3.0	0.0%
43	0.075	0.96	4.10	1.15	3.0	0.0%
44	0.075	0.54	4.10	0.93	3.0	0.0%
45	0.050	1.04	4.10	0.87	3.0	0.0%
46	0.075	0.39	4.10	1.03	3.0	0.0%
47	0.050	0.56	4.10	2.30	3.0	0.0%
48	0.150	0.81	4.10	2.12	0.3	0.0%
49	0.100	0.88	4.10	1.58	3.0	0.0%
50	0.100	0.94	4.10	1.30	3.0	0.0%
51	0.150	0.47	4.10	1.78	3.0	0.0%
52	0.075	0.56	4.10	1.96	3.0	0.0%
53	0.150	0.51	4.10	2.02	0.7	0.0%
54	0.050	0.51	4.10	0.60	3.0	0.0%
55	0.1	0.82	4.10	2.48	3.0	0.0%
56	0.05	0.65	4.10	1.69	3.0	0.0%
57	0.175	1.10	4.10	1.17	3.0	0.0%
58	0.125	0.95	4.10	1.71	3.0	0.0%
59	0.05	1.03	4.10	2.18	3.0	0.0%
60	0.15	1.16	4.10	0.94	3.0	0.0%
61	0.05	0.83	4.10	0.34	3.0	0.0%
62	0.05	0.34	4.10	0.36	3.0	0.0%
63	0.125	0.32	4.10	0.64	3.0	0.0%
64	0.1	0.85	4.10	0.48	3.0	0.0%
65	0.125	1.13	4.10	2.56	0.3	0.0%
66	0.1	0.35	4.10	0.57	3.0	0.0%
67	0.05	0.51	4.10	1.35	3.0	0.0%
68	0.05	1.04	4.10	0.95	3.0	0.0%
69	0.175	0.82	4.10	0.70	3.0	0.0%
70	0.05	1.09	4.10	2.05	3.0	0.0%
71	0.05	0.46	4.10	1.93	3.0	0.0%
72	0.1	0.88	4.10	2.29	3.0	0.0%
73	0.125	0.99	4.10	0.47	3.0	0.0%
74	0.175	0.92	4.10	2.03	0.7	0.0%
75	0.05	1.06	4.10	1.18	3.0	0.0%
76	0.075	0.48	4.10	0.33	3.0	0.0%
77	0.05	0.40	4.10	1.32	3.0	0.0%
78	0.1	1.05	4.10	0.80	3.0	0.0%
79	0.1	1.19	4.10	1.19	3.0	0.0%

Table C.3 (cont.)

80	0.075	1.20	4.10	2.61	3.0	0.0%
81	0.075	0.85	4.10	1.81	3.0	0.0%
82	0.1	0.61	4.10	1.88	0.5	0.1%
83	0.075	0.72	4.10	0.34	3.0	0.0%
84	0.05	0.56	4.10	2.62	3.0	0.0%
85	0.05	1.18	4.10	1.26	3.0	0.0%
86	0.2	1.02	4.10	1.20	2.7	0.0%
87	0.075	0.75	4.10	0.95	3.0	0.0%
88	0.125	0.93	4.10	2.09	0.7	0.0%
89	0.05	0.97	4.10	1.19	3.0	0.0%
90	0.075	0.43	4.10	2.03	3.0	0.0%
91	0.05	0.31	4.10	0.40	3.0	0.0%
92	0.05	0.59	4.10	0.75	3.0	0.0%
93	0.05	0.43	4.10	1.29	3.0	0.0%
94	0.075	0.59	4.10	1.23	3.0	0.0%
95	0.15	0.60	4.10	0.58	3.0	0.0%
96	0.225	0.99	4.10	2.35	0.6	0.4%
97	0.2	0.79	4.10	1.19	3.0	0.0%
98	0.175	0.86	4.10	1.78	3.0	0.0%
99	0.15	0.80	4.10	0.80	3.0	0.0%
100	0.1	0.46	4.10	1.30	3.0	0.0%
101	0.15	0.70	4.10	2.35	3.0	0.0%
102	0.05	0.57	4.10	1.96	3.0	0.0%
103	0.2	0.38	4.10	1.92	3.0	0.0%
104	0.05	0.65	4.10	1.97	3.0	0.0%
105	0.15	1.17	4.10	0.97	3.0	0.0%
106	0.15	0.60	4.10	2.64	3.0	0.0%
107	0.05	0.63	4.10	0.88	3.0	0.0%
108	0.05	0.91	4.10	1.70	3.0	0.0%
109	0.075	1.12	4.10	0.90	3.0	0.0%
110	0.05	0.31	4.10	1.20	3.0	0.0%
111	0.1	0.71	4.10	0.94	3.0	0.0%
112	0.1	0.90	4.10	2.34	3.0	0.0%
113	0.2	0.57	4.10	2.58	3.0	0.0%
114	0.1	0.76	4.10	0.94	2.5	0.0%
115	0.075	0.85	4.10	0.70	0.3	0.0%
116	0.15	0.53	4.10	1.24	3.0	0.0%
117	0.05	0.81	4.10	1.75	3.0	0.0%
118	0.075	0.55	4.10	0.41	3.0	0.0%
119	0.125	0.88	4.10	1.85	3.0	0.0%
120	0.05	0.64	4.10	2.05	3.0	0.0%

Table C.3 (cont.)

121	0.05	0.77	4.10	0.38	3.0	0.0%
122	0.05	0.99	4.10	2.48	3.0	0.0%
123	0.125	1.17	4.10	2.11	3.0	0.0%
124	0.075	0.85	4.10	1.52	3.0	0.0%
125	0.15	0.59	4.10	0.61	3.0	0.0%
126	0.1	1.15	4.10	0.90	3.0	0.0%
127	0.1	0.94	4.10	2.61	3.0	0.0%
128	0.05	0.31	4.10	2.57	3.0	0.0%
129	0.075	0.33	4.10	0.69	1.0	0.0%
130	0.15	0.37	4.10	2.42	3.0	0.0%
131	0.075	0.64	4.10	0.91	3.0	0.0%
132	0.075	0.85	4.10	0.64	3.0	0.0%
133	0.15	0.98	4.10	1.00	3.0	0.0%
134	0.05	0.30	4.10	2.58	0.3	0.0%
135	0.05	0.49	4.10	0.87	3.0	0.0%
136	0.15	0.71	4.10	0.85	3.0	0.0%
137	0.05	0.44	4.10	0.87	3.0	0.0%
138	0.2	1.01	4.10	2.50	3.0	0.0%
139	0.05	0.80	4.10	0.86	2.6	0.0%
140	0.2	0.92	4.10	2.09	3.0	0.0%
141	0.2	0.54	4.10	0.89	3.0	0.0%
142	0.1	0.35	4.10	1.22	3.0	0.0%
143	0.1	0.41	4.10	2.62	3.0	0.0%
144	0.175	0.89	4.10	2.14	3.0	0.0%
145	0.125	0.84	4.10	2.67	3.0	0.0%
146	0.05	0.76	4.10	0.53	3.0	0.0%
147	0.1	0.42	4.10	2.27	3.0	0.0%
148	0.05	0.49	4.10	0.64	3.0	0.0%
149	0.15	0.51	4.10	1.95	3.0	0.0%
150	0.2	0.34	4.10	0.75	3.0	0.0%
151	0.1	0.61	4.10	2.40	3.0	0.0%
152	0.075	0.91	4.10	1.82	3.0	0.0%
153	0.05	0.79	4.10	2.48	3.0	0.0%
154	0.15	0.62	4.10	0.56	3.0	0.0%
155	0.05	0.58	4.10	1.57	3.0	0.0%
156	0.075	0.64	4.10	0.42	3.0	0.0%
157	0.05	1.04	4.10	0.34	3.0	0.0%
158	0.175	0.38	4.10	1.41	3.0	0.0%
159	0.1	0.64	4.10	1.82	0.3	0.0%
160	0.075	1.20	4.10	0.54	3.0	0.0%
161	0.05	0.45	4.10	1.39	3.0	0.0%

Table C.3 (cont.)

162	0.15	0.49	4.10	2.41	3.0	0.0%
163	0.1	0.70	4.10	2.22	3.0	0.0%
164	0.125	0.81	4.10	0.44	3.0	0.0%
165	0.05	0.32	4.10	1.61	3.0	0.0%
166	0.1	0.46	4.10	2.24	3.0	0.0%
167	0.15	0.92	4.10	2.14	2.6	0.0%
168	0.1	0.40	4.10	2.50	3.0	0.0%
169	0.1	1.03	4.10	1.72	3.0	0.0%
170	0.2	0.58	4.10	1.46	3.0	0.0%
171	0.05	0.39	4.10	2.37	3.0	0.0%
172	0.125	0.54	4.10	1.71	3.0	0.0%
173	0.05	0.90	4.10	1.06	3.0	0.0%
174	0.15	0.35	4.10	1.55	3.0	0.0%
175	0.2	0.85	4.10	2.25	3.0	0.0%
176	0.05	0.56	4.10	2.19	3.0	0.0%
177	0.05	0.42	4.10	2.62	3.0	0.0%
178	0.125	1.19	4.10	2.27	3.0	0.0%
179	0.2	1.13	4.10	2.05	3.0	0.0%
180	0.15	0.74	4.10	0.47	3.0	0.0%
181	0.125	0.46	4.10	1.73	3.0	0.0%
182	0.1	0.84	4.10	2.55	3.0	0.0%
183	0.15	0.44	4.10	1.31	3.0	0.0%
184	0.1	0.92	4.10	1.20	3.0	0.0%
185	0.075	1.02	4.10	0.68	3.0	0.0%
186	0.1	0.69	4.10	0.44	3.0	0.0%
187	0.15	1.06	4.10	2.52	3.0	0.0%
188	0.175	1.07	4.10	1.97	0.5	1.3%
189	0.175	0.41	4.10	0.75	0.4	0.0%
190	0.075	1.13	4.10	0.47	3.0	0.0%
191	0.2	1.17	4.10	2.06	3.0	0.0%
192	0.05	0.32	4.10	0.81	3.0	0.0%
193	0.15	0.95	4.10	1.01	3.0	0.0%
194	0.175	0.74	4.10	2.62	3.0	0.0%
195	0.05	0.43	4.10	1.45	3.0	0.0%
196	0.1	0.88	4.10	0.57	3.0	0.0%
197	0.1	0.58	4.10	2.57	3.0	0.0%
198	0.2	1.13	4.10	0.34	0.1	0.0%
199	0.15	0.61	4.10	0.31	3.0	0.0%
200	0.05	0.91	4.10	0.38	3.0	0.0%
201	0.05	0.33	4.10	2.62	3.0	0.0%
202	0.1	1.04	4.10	0.76	3.0	0.0%

Table C.3 (cont.)

203	0.075	1.16	4.10	2.44	3.0	0.0%
204	0.05	1.10	4.10	1.35	3.0	0.0%
205	0.05	0.70	4.10	2.27	3.0	0.0%
206	0.05	0.54	4.10	2.66	3.0	0.0%
207	0.175	1.10	4.10	0.58	2.4	0.0%
208	0.15	1.02	4.10	2.26	3.0	0.0%
209	0.175	0.97	4.10	0.71	3.0	0.0%
210	0.175	0.45	4.10	1.07	3.0	0.0%
211	0.075	0.57	4.10	0.54	3.0	0.0%
212	0.075	0.99	4.10	1.14	3.0	0.0%
213	0.125	0.46	4.10	1.01	1.5	0.0%
214	0.1	0.36	4.10	0.80	3.0	0.0%
215	0.05	1.19	4.10	0.98	3.0	0.0%
216	0.05	0.45	4.10	0.92	3.0	0.0%
217	0.2	0.32	4.10	1.31	3.0	0.0%
218	0.075	0.80	4.10	0.56	3.0	0.0%
219	0.05	1.03	4.10	2.66	3.0	0.0%
220	0.15	0.38	4.10	2.51	3.0	0.0%
221	0.1	1.18	4.10	2.10	3.0	0.0%
222	0.075	0.92	4.10	0.37	3.0	0.0%
223	0.05	1.11	4.10	1.47	3.0	0.0%
224	0.1	0.66	4.10	1.38	3.0	0.0%
225	0.075	0.86	4.10	1.23	3.0	0.0%
226	0.05	0.90	4.10	0.94	3.0	0.0%
227	0.15	0.97	4.10	2.60	3.0	0.0%
228	0.175	1.04	4.10	0.95	3.0	0.0%
229	0.075	0.44	4.10	2.34	3.0	0.0%
230	0.125	0.99	4.10	1.53	3.0	0.0%
231	0.125	0.48	4.10	2.55	3.0	0.0%
232	0.125	0.48	4.10	1.42	3.0	0.0%
233	0.15	1.14	4.10	1.10	3.0	0.0%
234	0.075	0.60	4.10	1.47	0.1	0.0%
235	0.125	0.58	4.10	1.88	3.0	0.0%
236	0.125	0.88	4.10	0.69	3.0	0.0%
237	0.05	1.10	4.10	1.00	3.0	0.0%
238	0.2	0.37	4.10	2.15	3.0	0.0%
239	0.125	0.39	4.10	2.22	3.0	0.0%
240	0.075	0.32	4.10	0.76	3.0	0.0%
241	0.125	0.49	4.10	1.23	3.0	0.0%
242	0.075	1.17	4.10	0.73	3.0	0.0%
243	0.05	1.13	4.10	1.00	3.0	0.0%

Table C.3 (cont.)

244	0.075	0.88	4.10	1.12	3.0	0.0%
245	0.2	0.78	4.10	1.34	3.0	0.0%
246	0.05	0.53	4.10	2.00	3.0	0.0%
247	0.1	1.15	4.10	2.17	3.0	0.0%
248	0.1	0.61	4.10	1.87	3.0	0.0%
249	0.05	1.03	4.10	2.11	3.0	0.0%
250	0.05	0.84	4.10	0.56	3.0	0.0%
251	0.1	0.49	4.10	0.56	3.0	0.0%
252	0.075	0.98	4.10	0.71	3.0	0.0%
253	0.05	0.73	4.10	1.34	3.0	0.0%
254	0.125	1.16	4.10	2.26	3.0	0.0%
255	0.225	0.39	4.10	2.48	0.9	0.0%
256	0.05	1.12	4.10	2.22	0.2	0.0%
257	0.15	0.90	4.10	0.54	3.0	0.0%
258	0.1	0.42	4.10	1.92	3.0	0.0%
259	0.1	0.89	4.10	1.54	3.0	0.0%
260	0.1	0.31	4.10	1.46	3.0	0.0%
261	0.075	0.53	4.10	0.64	3.0	0.0%
262	0.15	0.41	4.10	2.33	3.0	0.0%
263	0.05	0.75	4.10	0.65	3.0	0.0%
264	0.1	0.37	4.10	2.65	3.0	0.0%
265	0.2	0.90	4.10	0.97	3.0	0.0%
266	0.15	0.47	4.10	1.26	3.0	0.0%
267	0.1	1.18	4.10	0.65	3.0	0.0%
268	0.15	1.20	4.10	1.64	3.0	0.0%
269	0.05	0.77	4.10	0.97	3.0	0.0%
270	0.125	0.44	4.10	1.00	3.0	0.0%
271	0.125	0.95	4.10	1.22	3.0	0.0%
272	0.1	0.77	4.10	0.64	3.0	0.0%
273	0.05	0.55	4.10	1.62	3.0	0.0%
274	0.05	0.42	4.10	1.48	3.0	0.0%
275	0.15	0.92	4.10	1.28	3.0	0.0%
276	0.15	0.51	4.10	0.84	3.0	0.0%
277	0.05	0.80	4.10	1.31	3.0	0.0%
278	0.05	0.54	4.10	1.72	3.0	0.0%
279	0.05	0.63	4.10	1.67	3.0	0.0%
280	0.075	0.77	4.10	1.20	3.0	0.0%
281	0.075	0.51	4.10	1.57	3.0	0.0%
282	0.15	0.86	4.10	1.39	3.0	0.0%
283	0.125	1.20	4.10	2.13	0.2	0.0%
284	0.05	0.96	4.10	0.84	3.0	0.0%

Table C.3 (cont.)

285	0.125	0.73	4.10	0.85	3.0	0.0%
286	0.075	0.36	4.10	0.91	3.0	0.0%
287	0.05	0.48	4.10	0.84	3.0	0.0%
288	0.175	0.33	4.10	1.23	2.4	0.0%

Appendix D

Particle Injection Parameter Values for the Design of Simulation Experiments

Particles were injected from a 1.5 µm by 3.0 µm (x-axis and z-axis, respectively) pressure inlet which is located at a y-value of 4.1 µm in a tortuous pore geometry. The particles injected into the system for the design of experiments are shown in Table D.1.

Table D.1 - Particle Injection Parameters

Particle Number	Particle Diameter [um]	Injection Location [um]			Filtration Time [hr]
		X	Y	Z	
1	0.125	0.47	4.10	0.50	0.0
2	0.125	0.63	4.10	2.15	0.0
3	0.150	0.36	4.10	1.61	0.0
4	0.200	0.90	4.10	0.71	1.5
5	0.125	0.37	4.10	0.91	1.5
6	0.125	1.02	4.10	1.37	1.5
7	0.125	0.68	4.10	2.25	1.5
8	0.125	0.33	4.10	0.35	1.5
9	0.200	0.96	4.10	0.62	3.1
10	0.125	0.80	4.10	0.86	3.1
11	0.125	0.65	4.10	1.55	3.1

Table D.1 (cont.)

12	0.125	1.05	4.10	2.47	3.1
13	0.125	0.58	4.10	1.93	3.1
14	0.150	0.52	4.10	1.53	3.1
15	0.125	0.88	4.10	1.07	3.1
16	0.125	0.85	4.10	0.46	3.1
17	0.125	0.69	4.10	2.68	3.1
18	0.125	0.55	4.10	2.21	3.1
19	0.125	0.59	4.10	2.39	3.1
20	0.125	0.89	4.10	0.91	3.1
21	0.125	0.47	4.10	0.85	3.1
22	0.200	1.14	4.10	1.24	4.6
23	0.200	0.38	4.10	1.04	6.1
24	0.125	0.31	4.10	1.80	6.1
25	0.125	0.53	4.10	2.33	6.1
26	0.125	0.69	4.10	1.80	6.1
27	0.125	0.63	4.10	2.26	6.1
28	0.125	0.54	4.10	1.21	6.1
29	0.125	0.39	4.10	1.65	6.1
30	0.150	1.00	4.10	2.09	6.2
31	0.125	0.69	4.10	0.93	6.2
32	0.125	1.05	4.10	1.35	6.2
33	0.125	0.85	4.10	0.92	6.2
34	0.125	0.37	4.10	1.97	6.2
35	0.200	1.13	4.10	0.71	7.7
36	0.200	0.94	4.10	1.79	9.2
37	0.125	0.78	4.10	1.30	9.2
38	0.150	0.34	4.10	2.34	9.2
39	0.125	0.90	4.10	1.31	9.2
40	0.125	0.51	4.10	1.42	9.2
41	0.150	1.19	4.10	1.17	9.3
42	0.200	0.79	4.10	2.00	10.8
43	0.150	0.31	4.10	2.43	10.8
44	0.150	1.20	4.10	2.50	10.8
45	0.150	0.80	4.10	1.14	10.8
46	0.150	1.08	4.10	0.68	10.9
47	0.125	0.32	4.10	2.19	10.9
48	0.125	1.14	4.10	0.58	10.9
49	0.150	0.44	4.10	2.35	10.9
50	0.125	0.83	4.10	1.96	10.9
51	0.125	0.66	4.10	0.71	10.9
52	0.125	0.52	4.10	2.42	10.9

Table D.1 (cont.)

53	0.150	0.68	4.10	0.88	10.9
54	0.150	0.51	4.10	0.44	10.9
55	0.200	0.58	4.10	0.38	12.4
56	0.125	0.30	4.10	1.29	12.4
57	0.200	0.85	4.10	1.61	14.0
58	0.150	0.65	4.10	1.32	14.0
59	0.125	1.09	4.10	1.85	14.0
60	0.125	0.80	4.10	0.90	14.0
61	0.125	1.07	4.10	2.65	14.0
62	0.125	1.17	4.10	1.21	14.0
63	0.200	0.68	4.10	0.77	15.5
64	0.125	0.32	4.10	1.37	15.5
65	0.150	0.95	4.10	2.30	15.5
66	0.125	0.98	4.10	0.88	15.5
67	0.125	0.44	4.10	2.69	15.5
68	0.125	0.64	4.10	1.42	15.5
69	0.125	0.81	4.10	1.44	15.5
70	0.125	0.58	4.10	2.47	15.5
71	0.200	0.66	4.10	1.18	17.1
72	0.200	1.17	4.10	2.63	18.6
73	0.200	0.43	4.10	0.39	20.1
74	0.125	0.73	4.10	1.49	20.1
75	0.200	1.19	4.10	1.80	21.6
76	0.200	0.42	4.10	1.12	23.1
77	0.125	1.18	4.10	0.69	23.1
78	0.150	0.67	4.10	2.07	23.1
79	0.125	1.08	4.10	2.61	23.1
80	0.125	0.90	4.10	2.61	23.1
81	0.150	0.70	4.10	1.90	23.2
82	0.125	1.07	4.10	1.94	23.2
83	0.125	0.50	4.10	0.33	23.2
84	0.125	0.71	4.10	2.62	23.2
85	0.125	1.06	4.10	1.73	23.2
86	0.125	0.53	4.10	1.64	23.2
87	0.200	0.54	4.10	1.07	24.7
88	0.200	0.37	4.10	2.06	26.2
89	0.200	1.04	4.10	2.49	27.7
90	0.200	0.96	4.10	0.47	29.2
91	0.200	1.06	4.10	1.09	30.8
92	0.200	0.81	4.10	2.27	32.3
93	0.125	0.92	4.10	2.15	32.3

Table D.1 (cont.)

94	0.150	1.19	4.10	2.61	32.3
95	0.125	1.01	4.10	0.47	32.3
96	0.150	0.88	4.10	1.62	32.3
97	0.150	1.10	4.10	1.90	32.3
98	0.125	0.49	4.10	2.28	32.3
99	0.125	0.56	4.10	2.13	32.3
100	0.200	0.89	4.10	1.04	33.9
101	0.125	1.02	4.10	1.97	33.9
102	0.125	0.98	4.10	1.17	33.9
103	0.125	1.19	4.10	2.45	33.9
104	0.150	0.81	4.10	1.41	33.9
105	0.125	1.12	4.10	0.60	33.9
106	0.125	1.16	4.10	1.74	33.9
107	0.150	0.78	4.10	0.92	33.9
108	0.200	0.39	4.10	1.19	35.4
109	0.125	0.52	4.10	0.65	35.4
110	0.200	0.50	4.10	1.22	36.9
111	0.125	0.58	4.10	1.84	36.9
112	0.200	1.00	4.10	2.42	38.5
113	0.125	0.74	4.10	2.23	38.5
114	0.150	1.15	4.10	1.90	38.5
115	0.200	0.91	4.10	1.65	40.0
116	0.200	1.11	4.10	2.64	41.5
117	0.200	0.69	4.10	0.96	43.0
118	0.125	0.48	4.10	1.82	43.0
119	0.125	0.85	4.10	0.74	43.0
120	0.125	1.11	4.10	1.75	43.0
121	0.150	0.83	4.10	1.03	43.1
122	0.200	0.41	4.10	1.08	44.6
123	0.125	0.95	4.10	0.61	44.6
124	0.200	0.65	4.10	1.84	46.1
125	0.125	0.39	4.10	1.34	46.1
126	0.125	0.53	4.10	2.24	46.1
127	0.125	0.83	4.10	0.33	46.1
128	0.150	0.69	4.10	2.31	46.1
129	0.125	0.55	4.10	1.11	46.1
130	0.125	0.99	4.10	1.51	46.1
131	0.125	0.91	4.10	1.35	46.1
132	0.125	0.81	4.10	0.88	46.1
133	0.150	0.65	4.10	2.59	46.1
134	0.125	0.65	4.10	2.48	46.1

Table D.1 (cont.)

135	0.125	1.17	4.10	0.87	46.2
136	0.125	1.15	4.10	2.57	46.2
137	0.150	0.60	4.10	1.01	46.2
138	0.125	0.49	4.10	1.19	46.2
139	0.150	0.75	4.10	1.57	46.2
140	0.150	1.14	4.10	1.09	46.2
141	0.125	0.90	4.10	1.31	46.2
142	0.125	0.81	4.10	0.43	46.2
143	0.125	0.89	4.10	2.64	46.2
144	0.200	1.05	4.10	2.23	47.7
145	0.125	1.15	4.10	1.97	47.7
146	0.150	0.97	4.10	1.71	47.8
147	0.125	0.40	4.10	1.24	47.8
148	0.125	0.59	4.10	0.93	47.8
149	0.125	0.83	4.10	1.60	47.8
150	0.125	0.85	4.10	1.80	47.8
151	0.200	0.72	4.10	2.45	49.3
152	0.125	0.64	4.10	2.35	49.3
153	0.150	0.47	4.10	1.27	49.3
154	0.125	0.76	4.10	2.31	49.3
155	0.125	0.71	4.10	0.88	49.3
156	0.125	0.33	4.10	0.81	49.3
157	0.125	0.46	4.10	1.16	49.3
158	0.125	0.57	4.10	2.33	49.3
159	0.150	0.57	4.10	1.54	49.3
160	0.125	0.57	4.10	1.32	49.3
161	0.125	1.16	4.10	1.40	49.3
162	0.125	0.43	4.10	1.46	49.3
163	0.200	0.70	4.10	1.41	50.9
164	0.150	0.33	4.10	0.87	50.9
165	0.125	0.41	4.10	2.16	50.9
166	0.150	1.16	4.10	0.69	50.9
167	0.150	0.59	4.10	2.22	50.9
168	0.200	0.38	4.10	1.61	52.4
169	0.200	0.37	4.10	0.51	54.0
170	0.125	0.97	4.10	2.08	54.0
171	0.200	0.95	4.10	1.40	55.5
172	0.125	0.75	4.10	0.75	55.5
173	0.125	0.64	4.10	2.37	55.5
174	0.200	1.01	4.10	1.76	57.0
175	0.125	1.06	4.10	2.22	57.0

Table D.1 (cont.)

176	0.200	0.89	4.10	1.65	58.5
177	0.125	1.16	4.10	2.22	58.5
178	0.125	0.39	4.10	0.33	58.5
179	0.125	0.35	4.10	1.99	58.5
180	0.125	0.97	4.10	1.68	58.5
181	0.125	1.10	4.10	0.90	58.5
182	0.125	0.59	4.10	1.52	58.5
183	0.400	0.71	4.10	0.87	63.1

Appendix E

Particle Injection Data

Each particle injected has an associated penetration depth and caused a percent loss in system flux. The tables in this Appendix show the data for each respective simulation experiment.

Table E.1 - Particle Injection Data for Simulation Experiments 1, 2, and 3

	Simulation Experiment 1		Simulation Experiment 2		Simulation Experiment 3	
Particle Number	Penetration Depth [um]	% Loss in Flux [-]	Penetration Depth [um]	% Loss in Flux [-]	Penetration Depth [um]	% Loss in Flux [-]
1	3.0	0.0%	3.0	0.0%	2.7	0.1%
2	3.0	0.0%	3.0	0.0%	3.0	0.0%
3	3.0	0.0%	3.0	0.0%	0.4	0.0%
4	2.6	2.2%	2.6	2.4%	1.1	0.0%
5	0.6	0.0%	0.7	0.0%	0.4	0.0%
6	3.0	0.0%	3.0	0.0%	2.5	0.0%
7	2.3	0.0%	3.0	0.0%	3.0	0.0%
8	3.0	0.0%	3.0	0.0%	0.3	0.0%
9	2.6	2.9%	2.5	0.9%	0.5	0.0%
10	3.0	0.0%	3.0	0.0%	2.9	0.0%
11	3.0	0.0%	3.0	0.0%	3.0	0.0%
12	2.6	0.5%	3.0	0.0%	2.3	0.0%
13	3.0	0.0%	3.0	0.0%	3.0	0.0%
14	3.0	0.0%	3.0	0.0%	3.0	0.0%
15	3.0	0.0%	3.0	0.0%	2.4	0.0%
16	2.8	0.0%	3.0	0.0%	2.6	0.6%
17	3.0	0.0%	3.0	0.0%	2.9	0.0%

Table E.1 (cont.)

18	3.0	0.0%	2.3	0.0%	2.7	0.0%
19	3.0	0.0%	2.3	0.0%	3.0	0.0%
20	3.0	0.0%	3.0	0.0%	0.0	0.0%
21	3.0	0.0%	3.0	0.0%	1.2	0.0%
22	1.1	0.0%	1.1	0.0%	1.0	0.0%
23	2.5	2.1%	2.6	2.6%	-0.9	0.0%
24	3.0	0.0%	3.0	0.0%	0.5	0.0%
25	3.0	0.0%	3.0	0.0%	2.6	0.7%
26	3.0	0.0%	3.0	0.0%	3.0	0.0%
27	3.0	0.0%	3.0	0.0%	3.0	0.0%
28	3.0	0.0%	3.0	0.0%	3.0	0.0%
29	3.0	0.0%	3.0	0.0%	0.5	0.0%
30	3.0	0.0%	3.0	0.0%	3.0	0.0%
31	3.0	0.0%	3.0	0.0%	2.7	0.0%
32	3.0	0.0%	3.0	0.0%	2.6	0.3%
33	3.0	0.0%	3.0	0.0%	0.6	0.0%
34	3.0	0.0%	3.0	0.0%	0.8	0.0%
35	3.0	0.0%	3.0	0.0%	-0.7	0.0%
36	3.0	0.0%	3.0	0.0%	3.0	0.0%
37	3.0	0.0%	3.0	0.0%	3.0	0.0%
38	2.6	0.9%	3.0	0.0%	0.6	0.0%
39	3.0	0.0%	3.0	0.0%	2.4	0.0%
40	3.0	0.0%	3.0	0.0%	3.0	0.0%
41	3.0	0.0%	3.0	0.0%	0.8	0.0%
42	3.0	0.0%	3.0	0.0%	2.9	0.0%
43	3.0	0.0%	2.6	0.8%	0.7	0.0%
44	3.0	0.0%	3.0	0.0%	3.0	0.0%
45	3.0	0.0%	3.0	0.0%	3.0	0.0%
46	3.0	0.0%	3.0	0.0%	0.8	0.0%
47	3.0	0.0%	3.0	0.0%	3.0	0.0%
48	3.0	0.0%	3.0	0.0%	0.8	0.0%
49	3.0	0.0%	3.0	0.0%	2.6	0.6%
50	3.0	0.0%	3.0	0.0%	3.0	0.0%
51	3.0	0.0%	3.0	0.0%	2.9	0.0%
52	2.5	0.0%	2.6	0.8%	3.0	0.0%
53	1.3	0.0%	3.0	0.0%	2.4	0.0%
54	3.0	0.0%	3.0	0.0%	-0.1	0.0%
55	0.7	0.0%	0.5	0.0%	-1.0	0.0%
56	3.0	0.0%	2.6	0.9%	-0.2	0.0%
57	3.0	0.0%	3.0	0.0%	2.1	0.0%
58	3.0	0.0%	3.0	0.0%	3.0	0.0%

Table E.1 (cont.)

59	3.0	0.0%	3.0	0.0%	1.0	0.0%
60	3.0	0.0%	3.0	0.0%	0.9	0.0%
61	3.0	0.0%	3.0	0.0%	2.5	0.0%
62	1.6	0.0%	3.0	0.0%	2.3	0.0%
63	3.0	0.0%	2.6	2.2%	2.6	1.9%
64	3.0	0.0%	3.0	0.0%	-0.1	0.0%
65	3.0	0.0%	3.0	0.0%	1.9	0.0%
66	3.0	0.0%	3.0	0.0%	0.0	0.0%
67	3.0	0.0%	3.0	0.0%	0.1	0.0%
68	3.0	0.0%	3.0	0.0%	3.0	0.0%
69	3.0	0.0%	3.0	0.0%	3.0	0.0%
70	3.0	0.0%	3.0	0.0%	3.0	0.0%
71	3.0	0.0%	3.0	0.0%	0.2	0.0%
72	2.3	0.0%	2.3	0.0%	-0.9	0.0%
73	0.6	0.0%	0.4	0.0%	-1.0	0.0%
74	3.0	0.0%	3.0	0.0%	3.0	0.0%
75	3.0	0.0%	2.8	0.0%	0.3	0.0%
76	3.0	0.0%	3.0	0.0%	-0.2	0.0%
77	3.0	0.0%	3.0	0.0%	0.9	0.0%
78	3.0	0.0%	1.4	0.0%	3.0	0.0%
79	3.0	0.0%	2.0	0.0%	2.9	0.0%
80	3.0	0.0%	2.5	0.0%	2.4	0.0%
81	3.0	0.0%	3.0	0.0%	3.0	0.0%
82	3.0	0.0%	3.0	0.0%	3.0	0.0%
83	0.5	0.0%	3.0	0.0%	-0.1	0.0%
84	3.0	0.0%	3.0	0.0%	3.0	0.0%
85	3.0	0.0%	3.0	0.0%	2.9	0.0%
86	3.0	0.0%	3.0	0.0%	3.0	0.0%
87	3.0	0.0%	1.5	0.0%	0.0	0.0%
88	3.0	0.0%	3.0	0.0%	-0.3	0.0%
89	2.3	0.0%	3.0	0.0%	0.7	0.0%
90	3.0	0.0%	3.0	0.0%	-0.9	0.0%
91	1.0	0.0%	0.6	0.0%	-0.9	0.0%
92	2.0	0.0%	3.0	0.0%	2.3	0.0%
93	3.0	0.0%	3.0	0.0%	3.0	0.0%
94	1.8	0.0%	2.1	0.0%	0.4	0.0%
95	3.0	0.0%	3.0	0.0%	2.8	0.0%
96	3.0	0.0%	3.0	0.0%	3.0	0.0%
97	0.8	0.0%	3.0	0.0%	0.3	0.0%
98	3.0	0.0%	3.0	0.0%	3.0	0.0%
99	3.0	0.0%	3.0	0.0%	3.0	0.0%

Table E.1 (cont.)

100	0.6	0.0%	3.0	0.0%	0.7	0.0%
101	3.0	0.0%	3.0	0.0%	3.0	0.0%
102	3.0	0.0%	3.0	0.0%	3.0	0.0%
103	2.1	0.0%	2.0	0.0%	3.0	0.0%
104	3.0	0.0%	3.0	0.0%	3.0	0.0%
105	3.0	0.0%	3.0	0.0%	1.1	0.0%
106	3.0	0.0%	3.0	0.0%	1.0	0.0%
107	0.5	0.0%	3.0	0.0%	0.8	0.0%
108	3.0	0.0%	3.0	0.0%	-0.1	0.0%
109	3.0	0.0%	2.5	0.2%	2.5	0.0%
110	3.0	0.0%	3.0	0.0%	0.1	0.0%
111	3.0	0.0%	3.0	0.0%	3.0	0.0%
112	2.1	0.0%	2.0	0.0%	2.3	0.0%
113	3.0	0.0%	3.0	0.0%	2.4	0.0%
114	3.0	0.0%	3.0	0.0%	0.9	0.0%
115	3.0	0.0%	1.3	0.0%	2.7	0.0%
116	2.2	0.0%	1.7	0.0%	-1.0	0.0%
117	0.4	0.0%	3.0	0.0%	-0.8	0.0%
118	3.0	0.0%	3.0	0.0%	3.0	0.0%
119	3.0	0.0%	3.0	0.0%	3.0	0.0%
120	3.0	0.0%	3.0	0.0%	1.1	0.0%
121	3.0	0.0%	0.0	0.0%	0.3	0.0%
122	3.0	0.0%	3.0	0.0%	0.0	0.0%
123	3.0	0.0%	3.0	0.0%	2.8	0.0%
124	3.0	0.0%	3.0	0.0%	2.3	0.0%
125	3.0	0.0%	3.0	0.0%	0.4	0.0%
126	3.0	0.0%	3.0	0.0%	3.0	0.0%
127	3.0	0.0%	2.6	0.4%	-0.2	0.0%
128	3.0	0.0%	3.0	0.0%	3.0	0.0%
129	3.0	0.0%	3.0	0.0%	3.0	0.0%
130	3.0	0.0%	3.0	0.0%	2.9	0.0%
131	3.0	0.0%	3.0	0.0%	1.2	0.0%
132	3.0	0.0%	3.0	0.0%	3.0	0.0%
133	2.4	0.0%	2.1	0.0%	3.0	0.0%
134	3.0	0.0%	3.0	0.0%	2.3	0.0%
135	3.0	0.0%	3.0	0.0%	0.7	0.0%
136	2.0	0.0%	2.4	0.0%	2.5	0.0%
137	3.0	0.0%	0.5	0.0%	0.7	0.0%
138	3.0	0.0%	3.0	0.0%	3.0	0.0%
139	3.0	0.0%	3.0	0.0%	3.0	0.0%
140	1.0	0.0%	3.0	0.0%	0.2	0.0%

Table E.1 (cont.)

141	3.0	0.0%	1.2	0.0%	3.0	0.0%
142	3.0	0.0%	3.0	0.0%	0.1	0.0%
143	2.1	0.0%	2.2	0.0%	0.3	0.0%
144	3.0	0.0%	1.8	0.0%	1.0	0.0%
145	3.0	0.0%	3.0	0.0%	2.2	0.0%
146	3.0	0.0%	3.0	0.0%	2.1	0.0%
147	3.0	0.0%	3.0	0.0%	0.4	0.0%
148	0.6	0.0%	0.5	0.0%	-0.5	0.0%
149	3.0	0.0%	3.0	0.0%	3.0	0.0%
150	3.0	0.0%	3.0	0.0%	3.0	0.0%
151	1.8	0.0%	1.8	0.0%	3.0	0.0%
152	3.0	0.0%	2.0	0.0%	3.0	0.0%
153	3.0	0.0%	3.0	0.0%	0.4	0.0%
154	3.0	0.0%	3.0	0.0%	3.0	0.0%
155	0.1	0.0%	3.0	0.0%	1.4	0.0%
156	0.5	0.0%	0.6	0.0%	0.4	0.0%
157	3.0	0.0%	3.0	0.0%	2.6	0.5%
158	3.0	0.0%	3.0	0.0%	3.0	0.0%
159	3.0	0.0%	3.0	0.0%	3.0	0.0%
160	3.0	0.0%	3.0	0.0%	0.9	0.0%
161	3.0	0.0%	3.0	0.0%	0.9	0.0%
162	3.0	0.0%	3.0	0.0%	0.6	0.0%
163	3.0	0.0%	3.0	0.0%	3.0	0.0%
164	0.6	0.0%	0.5	0.0%	0.1	0.0%
165	3.0	0.0%	3.0	0.0%	3.0	0.0%
166	3.0	0.0%	3.0	0.0%	0.7	0.0%
167	3.0	0.0%	3.0	0.0%	3.0	0.0%
168	3.0	0.0%	3.0	0.0%	-0.8	0.0%
169	0.8	0.0%	2.0	0.0%	3.0	0.0%
170	3.0	0.0%	3.0	0.0%	2.2	0.0%
171	3.0	0.0%	1.2	0.0%	3.0	0.0%
172	3.0	0.0%	3.0	0.0%	3.0	0.0%
173	3.0	0.0%	3.0	0.0%	1.9	0.0%
174	3.0	0.0%	2.4	0.0%	2.1	0.0%
175	3.0	0.0%	3.0	0.0%	3.0	0.0%
176	3.0	0.0%	3.0	0.0%	2.5	0.0%
177	1.7	0.0%	3.0	0.0%	2.3	0.0%
178	0.6	0.0%	3.0	0.0%	-0.3	0.0%
179	2.7	0.0%	3.0	0.0%	0.7	0.0%
180	3.0	0.0%	3.0	0.0%	3.0	0.0%
181	3.0	0.0%	3.0	0.0%	-0.1	0.0%

Table E.1 (cont.)

182	3.0	0.0%	3.0	0.0%	3.0	0.0%
183	-0.1	0.0%	0.1	0.0%	0.0	0.0%

Table E.2 - Particle Injection Data for Simulation Experiments 4, 5, and 6

	Simulation Experiment 4		Simulation Experiment 5		Simulation Experiment 6	
Particle Number	Penetration Depth [um]	% Loss in Flux [-]	Penetration Depth [um]	% Loss in Flux [-]	Penetration Depth [um]	% Loss in Flux [-]
1	1.7	0.0%	3.0	0.0%	3.0	0.0%
2	3.0	0.0%	3.0	0.0%	3.0	0.0%
3	0.1	0.0%	3.0	0.0%	3.0	0.0%
4	0.7	0.0%	2.4	0.0%	2.5	0.0%
5	0.4	0.0%	0.7	0.0%	0.6	0.0%
6	2.7	0.0%	3.0	0.0%	3.0	0.0%
7	3.0	0.0%	3.0	0.0%	3.0	0.0%
8	-0.1	0.0%	3.0	0.0%	3.0	0.0%
9	-0.6	0.0%	3.0	0.0%	2.5	1.3%
10	0.3	0.0%	3.0	0.0%	3.0	0.0%
11	3.0	0.0%	3.0	0.0%	3.0	0.0%
12	2.1	0.0%	2.5	0.0%	3.0	0.0%
13	3.0	0.0%	3.0	0.0%	3.0	0.0%
14	2.7	0.4%	3.0	0.0%	3.0	0.0%
15	2.9	0.0%	3.0	0.0%	3.0	0.0%
16	2.9	0.0%	3.0	0.0%	3.0	0.0%
17	0.5	0.0%	3.0	0.0%	3.0	0.0%
18	3.0	0.0%	3.0	0.0%	2.3	0.0%
19	1.6	0.0%	2.3	0.0%	2.6	0.8%
20	1.0	0.0%	3.0	0.0%	0.6	0.0%
21	0.7	0.0%	3.0	0.0%	0.6	0.0%
22	1.0	0.0%	1.1	0.0%	1.2	0.0%
23	0.4	0.0%	2.5	2.0%	2.5	0.0%
24	0.5	0.0%	3.0	0.0%	3.0	0.0%
25	2.3	0.0%	3.0	0.0%	2.3	0.0%
26	3.0	0.0%	3.0	0.0%	3.0	0.0%
27	1.6	0.0%	3.0	0.0%	2.6	0.3%
28	3.0	0.0%	3.0	0.0%	3.0	0.0%
29	3.0	0.0%	3.0	0.0%	3.0	0.0%

Table E.2 (cont.)

30	1.7	0.0%	3.0	0.0%	3.0	0.0%
31	3.0	0.0%	3.0	0.0%	1.2	0.0%
32	3.0	0.0%	3.0	0.0%	3.0	0.0%
33	2.8	0.0%	3.0	0.0%	0.7	0.0%
34	3.0	0.0%	3.0	0.0%	3.0	0.0%
35	-0.2	0.0%	3.0	0.0%	3.0	0.0%
36	1.6	0.0%	3.0	0.0%	3.0	0.0%
37	3.0	0.0%	3.0	0.0%	3.0	0.0%
38	1.0	0.0%	3.0	0.0%	3.0	0.0%
39	2.4	0.0%	3.0	0.0%	3.0	0.0%
40	3.0	0.0%	3.0	0.0%	3.0	0.0%
41	3.0	0.0%	3.0	0.0%	3.0	0.0%
42	2.0	0.0%	3.0	0.0%	3.0	0.0%
43	0.7	0.0%	3.0	0.0%	1.8	0.0%
44	1.7	0.0%	3.0	0.0%	3.0	0.0%
45	2.8	0.0%	3.0	0.0%	1.0	0.0%
46	0.9	0.0%	3.0	0.0%	3.0	0.0%
47	0.7	0.0%	3.0	0.0%	3.0	0.0%
48	3.0	0.0%	3.0	0.0%	3.0	0.0%
49	1.5	0.0%	3.0	0.0%	3.0	0.0%
50	3.0	0.0%	3.0	0.0%	3.0	0.0%
51	2.6	1.0%	3.0	0.0%	3.0	0.0%
52	2.6	0.8%	2.6	0.5%	3.0	0.0%
53	2.8	0.0%	3.0	0.0%	1.2	0.0%
54	0.1	0.0%	3.0	0.0%	3.0	0.0%
55	-0.2	0.0%	3.0	0.0%	2.0	0.0%
56	0.2	0.0%	3.0	0.0%	3.0	0.0%
57	3.0	0.0%	3.0	0.0%	3.0	0.0%
58	3.0	0.0%	3.0	0.0%	3.0	0.0%
59	1.4	0.0%	3.0	0.0%	2.1	0.0%
60	1.2	0.0%	3.0	0.0%	0.5	0.0%
61	1.8	0.0%	3.0	0.0%	1.8	0.0%
62	3.0	0.0%	3.0	0.0%	3.0	0.0%
63	0.5	0.0%	3.0	0.0%	3.0	0.0%
64	0.4	0.0%	3.0	0.0%	3.0	0.0%
65	1.4	0.0%	3.0	0.0%	3.0	0.0%
66	0.8	0.0%	3.0	0.0%	3.0	0.0%
67	3.0	0.0%	3.0	0.0%	3.0	0.0%
68	3.0	0.0%	3.0	0.0%	3.0	0.0%
69	2.5	0.0%	3.0	0.0%	3.0	0.0%
70	3.0	0.0%	3.0	0.0%	2.2	0.0%

Table E.2 (cont.)

71	0.7	0.0%	3.0	0.0%	3.0	0.0%
72	-0.3	0.0%	2.3	0.0%	2.3	0.0%
73	-0.3	0.0%	0.6	0.0%	3.0	0.0%
74	3.0	0.0%	3.0	0.0%	3.0	0.0%
75	0.7	0.0%	3.0	0.0%	3.0	0.0%
76	3.0	0.0%	3.0	0.0%	3.0	0.0%
77	1.1	0.0%	3.0	0.0%	3.0	0.0%
78	3.0	0.0%	3.0	0.0%	3.0	0.0%
79	3.0	0.0%	2.1	0.0%	2.2	0.0%
80	2.5	0.0%	3.0	0.0%	2.4	0.0%
81	3.0	0.0%	3.0	0.0%	3.0	0.0%
82	2.0	0.0%	3.0	0.0%	3.0	0.0%
83	0.2	0.0%	3.0	0.0%	3.0	0.0%
84	2.4	0.0%	2.3	0.0%	2.4	0.0%
85	1.5	0.0%	3.0	0.0%	3.0	0.0%
86	3.0	0.0%	3.0	0.0%	3.0	0.0%
87	0.0	0.0%	3.0	0.0%	3.0	0.0%
88	1.4	0.0%	3.0	0.0%	2.3	0.0%
89	2.0	0.0%	2.0	0.0%	1.7	0.0%
90	0.2	0.0%	3.0	0.0%	3.0	0.0%
91	1.7	0.0%	0.6	0.0%	-0.1	0.0%
92	1.3	0.0%	1.5	0.0%	1.4	0.0%
93	3.0	0.0%	3.0	0.0%	1.6	0.0%
94	1.4	0.0%	1.8	0.0%	0.8	0.0%
95	2.7	0.2%	3.0	0.0%	2.5	0.0%
96	1.6	0.0%	3.0	0.0%	1.2	0.0%
97	1.1	0.0%	3.0	0.0%	3.0	0.0%
98	3.0	0.0%	3.0	0.0%	1.4	0.0%
99	3.0	0.0%	3.0	0.0%	3.0	0.0%
100	0.7	0.0%	3.0	0.0%	3.0	0.0%
101	1.6	0.0%	1.4	0.0%	3.0	0.0%
102	3.0	0.0%	3.0	0.0%	0.3	0.0%
103	3.0	0.0%	2.0	0.0%	3.0	0.0%
104	1.4	0.0%	3.0	0.0%	3.0	0.0%
105	1.1	0.0%	3.0	0.0%	3.0	0.0%
106	2.6	0.6%	3.0	0.0%	3.0	0.0%
107	3.0	0.0%	3.0	0.0%	2.0	0.0%
108	0.1	0.0%	3.0	0.0%	1.0	0.0%
109	3.0	0.0%	3.0	0.0%	3.0	0.0%
110	2.6	3.0%	3.0	0.0%	1.7	0.0%
111	3.0	0.0%	3.0	0.0%	3.0	0.0%

Table E.2 (cont.)

112	1.7	0.0%	2.1	0.0%	1.7	0.0%
113	3.0	0.0%	1.4	0.0%	3.0	0.0%
114	1.6	0.0%	3.0	0.0%	3.0	0.0%
115	2.9	0.0%	3.0	0.0%	0.9	0.0%
116	0.6	0.0%	1.6	0.0%	0.9	0.0%
117	0.1	0.0%	3.0	0.0%	3.0	0.0%
118	3.0	0.0%	3.0	0.0%	3.0	0.0%
119	3.0	0.0%	3.0	0.0%	3.0	0.0%
120	1.4	0.0%	3.0	0.0%	3.0	0.0%
121	0.4	0.0%	3.0	0.0%	3.0	0.0%
122	1.2	0.0%	3.0	0.0%	0.2	0.0%
123	3.0	0.0%	3.0	0.0%	3.0	0.0%
124	3.0	0.0%	3.0	0.0%	3.0	0.0%
125	0.1	0.0%	3.0	0.0%	2.2	0.0%
126	3.0	0.0%	3.0	0.0%	3.0	0.0%
127	0.4	0.0%	3.0	0.0%	3.0	0.0%
128	3.0	0.0%	3.0	0.0%	3.0	0.0%
129	2.1	0.0%	3.0	0.0%	0.1	0.0%
130	2.2	0.0%	3.0	0.0%	3.0	0.0%
131	2.7	0.0%	3.0	0.0%	0.8	0.0%
132	3.0	0.0%	3.0	0.0%	3.0	0.0%
133	2.5	0.0%	2.6	1.4%	1.7	0.0%
134	3.0	0.0%	3.0	0.0%	1.4	0.0%
135	0.3	0.0%	3.0	0.0%	3.0	0.0%
136	1.6	0.0%	2.2	0.0%	0.7	0.0%
137	0.0	0.0%	0.6	0.0%	0.1	0.0%
138	2.3	0.0%	3.0	0.0%	0.4	0.0%
139	1.3	0.0%	3.0	0.0%	3.0	0.0%
140	0.1	0.0%	3.0	0.0%	3.0	0.0%
141	3.0	0.0%	3.0	0.0%	0.4	0.0%
142	3.0	0.0%	3.0	0.0%	3.0	0.0%
143	3.0	0.0%	2.3	0.0%	0.9	0.0%
144	1.2	0.0%	1.7	0.0%	3.0	0.0%
145	2.6	0.9%	3.0	0.0%	3.0	0.0%
146	3.0	0.0%	3.0	0.0%	1.6	0.0%
147	3.0	0.0%	3.0	0.0%	1.1	0.0%
148	0.7	0.0%	3.0	0.0%	3.0	0.0%
149	3.0	0.0%	3.0	0.0%	1.6	0.0%
150	3.0	0.0%	3.0	0.0%	3.0	0.0%
151	2.3	0.0%	1.4	0.0%	1.2	0.0%
152	3.0	0.0%	1.4	0.0%	1.6	0.0%

Table E.2 (cont.)

153	0.6	0.0%	3.0	0.0%	0.2	0.0%
154	3.0	0.0%	3.0	0.0%	1.6	0.0%
155	3.0	0.0%	3.0	0.0%	3.0	0.0%
156	0.3	0.0%	3.0	0.0%	1.1	0.0%
157	3.0	0.0%	3.0	0.0%	0.0	0.0%
158	3.0	0.0%	3.0	0.0%	1.4	0.0%
159	3.0	0.0%	3.0	0.0%	2.0	0.0%
160	3.0	0.0%	3.0	0.0%	0.7	0.0%
161	3.0	0.0%	3.0	0.0%	1.0	0.0%
162	3.0	0.0%	3.0	0.0%	1.0	0.0%
163	1.0	0.0%	3.0	0.0%	0.9	0.0%
164	0.4	0.0%	0.6	0.0%	-0.1	0.0%
165	3.0	0.0%	3.0	0.0%	3.0	0.0%
166	1.0	0.0%	3.0	0.0%	2.4	0.0%
167	3.0	0.0%	3.0	0.0%	1.3	0.0%
168	1.2	0.0%	1.6	0.0%	1.1	0.0%
169	0.2	0.0%	3.0	0.0%	0.7	0.0%
170	3.0	0.0%	3.0	0.0%	3.0	0.0%
171	0.9	0.0%	0.9	0.0%	0.2	0.0%
172	3.0	0.0%	3.0	0.0%	3.0	0.0%
173	1.4	0.0%	1.4	0.0%	0.6	1.6%
174	2.5	0.0%	2.2	0.0%	2.2	0.0%
175	1.2	0.0%	1.7	0.0%	1.7	0.0%
176	2.9	0.0%	3.0	0.0%	3.0	0.0%
177	2.5	0.0%	3.0	0.0%	3.0	0.0%
178	2.4	0.0%	3.0	0.0%	3.0	0.0%
179	3.0	0.0%	3.0	0.0%	3.0	0.0%
180	3.0	0.0%	1.2	0.0%	1.2	0.0%
181	0.6	0.0%	3.0	0.0%	3.0	0.0%
182	3.0	0.0%	3.0	0.0%	3.0	0.0%
183	0.0	0.0%	0.1	3.0%	0.1	3.0%

Table E.3 - Particle Injection Data for Simulation Experiments 7, 8, and 9

	Simulation Experiment 7		Simulation Experiment 8		Simulation Experiment 9	
Particle Number	Penetration Depth [um]	% Loss in Flux [-]	Penetration Depth [um]	% Loss in Flux [-]	Penetration Depth [um]	% Loss in Flux [-]
1	3.0	0.0%	3.0	0.0%	3.0	0.0%
2	2.6	0.9%	2.6	0.9%	2.4	0.0%
3	0.4	0.0%	0.4	0.0%	3.0	0.0%
4	0.4	0.0%	0.3	0.0%	3.0	0.0%
5	0.5	0.0%	0.4	0.0%	3.0	0.0%
6	1.7	0.0%	1.7	0.0%	3.0	0.0%
7	1.5	0.0%	3.0	0.0%	3.0	0.0%
8	0.0	0.0%	0.4	0.0%	3.0	0.0%
9	2.9	0.0%	2.6	1.3%	3.0	0.0%
10	1.2	0.0%	1.1	0.0%	3.0	0.0%
11	3.0	0.0%	3.0	0.0%	3.0	0.0%
12	2.3	0.0%	2.5	0.0%	2.5	0.1%
13	3.0	0.0%	3.0	0.0%	3.0	0.0%
14	3.0	0.0%	3.0	0.0%	3.0	0.0%
15	1.1	0.0%	0.7	0.0%	3.0	0.0%
16	2.6	0.7%	2.5	0.0%	3.0	0.0%
17	0.2	0.0%	0.5	0.0%	3.0	0.0%
18	2.3	0.0%	3.0	0.0%	3.0	0.0%
19	3.0	0.0%	3.0	0.0%	3.0	0.0%
20	0.9	0.0%	-0.3	0.0%	3.0	0.0%
21	2.4	0.0%	1.9	0.0%	3.0	0.0%
22	0.6	0.0%	1.4	0.0%	3.0	0.0%
23	0.4	0.0%	0.2	0.0%	3.0	0.0%
24	0.5	0.0%	0.6	0.0%	3.0	0.0%
25	2.0	0.0%	2.5	0.0%	3.0	0.0%
26	3.0	0.0%	3.0	0.0%	3.0	0.0%
27	3.0	0.0%	2.2	0.0%	3.0	0.0%
28	3.0	0.0%	1.8	0.0%	3.0	0.0%
29	3.0	0.0%	2.6	0.5%	3.0	0.0%
30	1.5	0.0%	1.8	0.0%	3.0	0.0%
31	2.7	0.3%	0.8	0.0%	1.3	0.0%
32	2.5	0.0%	2.4	0.0%	3.0	0.0%
33	2.5	0.1%	0.2	0.0%	3.0	0.0%
34	3.0	0.0%	2.3	0.0%	3.0	0.0%
35	0.1	0.0%	-0.1	0.0%	3.0	0.0%
36	2.5	1.1%	1.7	0.0%	3.0	0.0%
37	3.0	0.0%	0.8	0.0%	3.0	0.0%
38	0.6	0.0%	0.9	0.0%	2.5	0.5%

Table E.3 (cont.)

39	0.7	0.0%	0.7	0.0%	3.0	0.0%
40	3.0	0.0%	2.9	0.0%	3.0	0.0%
41	0.2	0.0%	0.3	0.0%	3.0	0.0%
42	2.3	0.0%	1.7	0.0%	3.0	0.0%
43	0.5	0.0%	1.0	0.0%	1.2	0.0%
44	0.6	0.0%	1.8	0.0%	3.0	0.0%
45	1.3	0.0%	3.0	0.0%	3.0	0.0%
46	0.7	0.0%	1.0	0.0%	3.0	0.0%
47	0.9	0.0%	0.7	0.0%	3.0	0.0%
48	1.0	0.0%	1.3	0.0%	3.0	0.0%
49	0.8	0.0%	1.7	0.0%	3.0	0.0%
50	2.0	0.0%	3.0	0.0%	3.0	0.0%
51	2.9	0.0%	3.0	0.0%	3.0	0.0%
52	3.0	0.0%	1.6	0.0%	3.0	0.0%
53	0.2	0.0%	0.5	0.0%	0.7	0.0%
54	0.5	0.0%	0.3	0.0%	3.0	0.0%
55	-0.2	0.0%	0.4	0.0%	2.5	1.0%
56	0.2	0.0%	0.3	0.0%	3.0	0.0%
57	3.0	0.0%	3.0	0.0%	3.0	0.0%
58	2.4	0.0%	2.2	0.0%	3.0	0.0%
59	2.0	0.0%	3.0	0.0%	3.0	0.0%
60	0.0	0.0%	-0.7	0.0%	0.6	0.0%
61	0.3	0.0%	0.5	0.0%	3.0	0.0%
62	0.1	0.0%	1.3	0.0%	3.0	0.0%
63	0.5	0.0%	0.3	0.0%	3.0	0.0%
64	0.4	0.0%	0.5	0.0%	3.0	0.0%
65	0.7	0.0%	1.6	0.0%	3.0	0.0%
66	-0.1	0.0%	0.9	0.0%	3.0	0.0%
67	0.1	0.0%	0.3	0.0%	3.0	0.0%
68	0.8	0.0%	3.0	0.0%	3.0	0.0%
69	3.0	0.0%	3.0	0.0%	3.0	0.0%
70	2.2	0.0%	2.7	0.0%	3.0	0.0%
71	0.2	0.0%	0.4	0.0%	3.0	0.0%
72	-0.2	0.0%	3.0	0.0%	2.3	0.0%
73	0.0	0.0%	-0.1	0.0%	0.8	0.0%
74	3.0	0.0%	0.9	0.0%	1.6	0.0%
75	0.4	0.0%	0.8	0.0%	3.0	0.0%
76	0.5	0.0%	2.1	0.0%	3.0	0.0%
77	1.0	0.0%	0.2	0.0%	3.0	0.0%
78	2.5	0.0%	3.0	0.0%	3.0	0.0%
79	0.5	0.0%	0.6	0.0%	2.3	0.0%

Table E.3 (cont.)

80	2.2	0.0%	3.0	0.0%	2.0	0.0%
81	3.0	0.0%	2.8	0.0%	3.0	0.0%
82	0.5	0.0%	2.5	0.0%	3.0	0.0%
83	0.2	0.0%	0.1	0.0%	3.0	0.0%
84	0.5	0.0%	1.8	0.0%	3.0	0.0%
85	2.4	0.0%	3.0	0.0%	3.0	0.0%
86	3.0	0.0%	3.0	0.0%	3.0	0.0%
87	0.2	0.0%	0.2	0.0%	3.0	0.0%
88	0.2	0.0%	0.1	0.0%	3.0	0.0%
89	-0.3	0.0%	3.0	0.0%	1.9	0.0%
90	0.3	0.0%	0.0	0.0%	3.0	0.0%
91	0.1	0.0%	0.1	0.0%	1.1	0.0%
92	2.1	0.0%	2.4	0.0%	2.1	0.0%
93	2.5	0.0%	1.7	0.0%	3.0	0.0%
94	0.0	0.0%	0.0	0.0%	2.4	0.0%
95	1.1	0.0%	3.0	0.0%	3.0	0.0%
96	3.0	0.0%	1.9	0.0%	3.0	0.0%
97	3.0	0.0%	2.7	0.0%	3.0	0.0%
98	3.0	0.0%	2.2	0.0%	3.0	0.0%
99	3.0	0.0%	3.0	0.0%	3.0	0.0%
100	0.0	0.0%	0.1	0.0%	1.6	0.0%
101	0.4	0.0%	2.6	0.7%	3.0	0.0%
102	0.8	0.0%	1.6	0.0%	3.0	0.0%
103	0.9	0.0%	0.0	0.0%	2.1	0.0%
104	3.0	0.0%	3.0	0.0%	3.0	0.0%
105	1.0	0.0%	1.0	0.0%	3.0	0.0%
106	0.8	0.0%	1.2	0.0%	3.0	0.0%
107	0.0	0.0%	-0.1	0.0%	3.0	0.0%
108	-1.0	0.0%	2.1	0.0%	3.0	0.0%
109	2.4	0.0%	3.0	0.0%	3.0	0.0%
110	-0.4	0.0%	0.2	0.0%	3.0	0.0%
111	3.0	0.0%	3.0	0.0%	3.0	0.0%
112	0.2	0.0%	2.1	0.0%	2.2	0.0%
113	3.0	0.0%	3.0	0.0%	3.0	0.0%
114	0.6	0.0%	1.3	0.0%	3.0	0.0%
115	1.5	0.0%	1.3	0.0%	3.0	0.0%
116	-0.5	0.0%	1.3	0.0%	2.1	0.0%
117	-0.1	0.0%	-0.1	0.0%	0.5	0.0%
118	3.0	0.0%	3.0	0.0%	3.0	0.0%
119	3.0	0.0%	3.0	0.0%	3.0	0.0%
120	1.1	0.0%	1.6	0.0%	3.0	0.0%

Table E.3 (cont.)

121	-0.3	0.0%	-0.1	0.0%	0.2	0.0%
122	-0.5	0.0%	0.1	0.0%	1.5	0.0%
123	3.0	0.0%	1.2	0.0%	3.0	0.0%
124	2.2	0.0%	3.0	0.0%	3.0	0.0%
125	3.0	0.0%	3.0	0.0%	3.0	0.0%
126	3.0	0.0%	3.0	0.0%	3.0	0.0%
127	0.0	0.0%	2.8	0.0%	3.0	0.0%
128	2.2	0.0%	1.4	0.0%	1.8	0.0%
129	3.0	0.0%	0.3	0.0%	3.0	0.0%
130	0.2	0.0%	1.7	0.0%	3.0	0.0%
131	-0.4	0.0%	1.4	0.0%	3.0	0.0%
132	1.1	0.0%	2.6	0.8%	3.0	0.0%
133	1.7	-0.8%	0.0	0.0%	2.4	0.0%
134	1.4	0.0%	3.0	0.0%	2.2	0.0%
135	3.0	0.0%	0.7	0.0%	3.0	0.0%
136	0.7	0.0%	0.8	0.0%	2.2	0.0%
137	0.1	0.0%	0.2	0.0%	0.6	0.0%
138	0.4	0.0%	3.0	0.0%	3.0	0.0%
139	3.0	0.0%	2.7	0.0%	1.2	0.0%
140	3.0	0.0%	-0.1	0.0%	3.0	0.0%
141	0.4	0.0%	0.5	0.0%	3.0	0.0%
142	3.0	0.0%	3.0	0.0%	3.0	0.0%
143	0.9	0.0%	3.0	0.0%	2.3	0.0%
144	3.0	0.0%	3.0	0.0%	2.0	0.0%
145	3.0	0.0%	3.0	0.0%	3.0	0.0%
146	1.6	0.0%	3.0	0.0%	3.0	0.0%
147	1.1	0.0%	3.0	0.0%	3.0	0.0%
148	3.0	0.0%	0.1	0.0%	0.5	0.0%
149	1.6	0.0%	3.0	0.0%	3.0	0.0%
150	3.0	0.0%	1.3	0.0%	3.0	0.0%
151	1.2	0.0%	1.4	0.0%	2.3	0.0%
152	1.6	0.0%	2.9	0.0%	1.9	0.0%
153	0.2	0.0%	3.0	0.0%	3.0	0.0%
154	1.6	0.0%	1.4	0.0%	2.0	0.0%
155	3.0	0.0%	1.6	0.0%	3.0	0.0%
156	1.1	0.0%	0.1	0.0%	0.5	0.0%
157	0.0	0.0%	0.6	0.0%	3.0	0.0%
158	1.4	0.0%	1.3	0.0%	3.0	0.0%
159	2.0	0.0%	3.0	0.0%	3.0	0.0%
160	0.7	0.0%	3.0	0.0%	3.0	0.0%
161	1.0	0.0%	0.9	0.0%	3.0	0.0%

Table E.3 (cont.)

162	1.0	0.0%	3.0	0.0%	3.0	0.0%
163	0.9	0.0%	3.0	0.0%	3.0	0.0%
164	-0.1	0.0%	0.2	0.0%	0.5	0.0%
165	3.0	0.0%	3.0	0.0%	3.0	0.0%
166	2.4	0.0%	0.1	0.0%	3.0	0.0%
167	1.3	0.0%	3.0	0.0%	3.0	0.0%
168	1.1	0.0%	0.2	0.0%	3.0	0.0%
169	0.7	0.0%	0.0	0.0%	0.5	0.0%
170	3.0	0.0%	1.7	0.0%	3.0	0.0%
171	0.2	0.0%	1.6	0.0%	0.9	0.0%
172	3.0	0.0%	3.0	0.0%	3.0	0.0%
173	0.6	1.6%	3.0	0.0%	3.0	0.0%
174	2.2	0.0%	1.4	0.0%	3.0	0.0%
175	1.7	0.0%	1.3	0.0%	2.6	0.9%
176	3.0	0.0%	0.6	0.0%	3.0	0.0%
177	3.0	0.0%	0.8	0.0%	3.0	0.0%
178	3.0	0.0%	3.0	0.0%	0.4	0.0%
179	3.0	0.0%	0.6	0.0%	3.0	0.0%
180	1.2	0.0%	3.0	0.0%	3.0	0.0%
181	3.0	0.0%	0.9	0.0%	3.0	0.0%
182	3.0	0.0%	0.8	0.0%	3.0	0.0%
183	0.1	3.0%	0.8	0.0%	-0.2	0.0%

Table E.4 - Particle Injection Data for Simulation Experiments 10, 11, and 12

	Simulation Experiment 10		Simulation Experiment 11		Simulation Experiment 12	
Particle Number	Penetration Depth [um]	% Loss in Flux [-]	Penetration Depth [um]	% Loss in Flux [-]	Penetration Depth [um]	% Loss in Flux [-]
1	3.0	0.0%	3.0	0.0%	1.6	0.0%
2	3.0	0.0%	3.0	0.0%	1.6	0.0%
3	3.0	0.0%	3.0	0.0%	0.7	0.0%
4	3.0	0.0%	1.1	0.0%	2.9	0.0%
5	0.6	0.0%	1.6	0.0%	0.4	0.0%
6	3.0	0.0%	3.0	0.0%	2.8	0.0%
7	3.0	0.0%	2.3	0.0%	3.0	0.0%
8	3.0	0.0%	2.5	0.0%	-0.2	0.0%
9	2.6	2.3%	2.7	1.2%	0.5	0.0%

Table E.4 (cont.)

10	2.6	0.9%	0.2	0.0%	1.2	0.0%
11	3.0	0.0%	3.0	0.0%	3.0	0.0%
12	2.5	0.0%	3.0	0.0%	2.6	1.3%
13	3.0	0.0%	3.0	0.0%	3.0	0.0%
14	3.0	0.0%	3.0	0.0%	2.6	1.1%
15	3.0	0.0%	3.0	0.0%	0.6	0.0%
16	3.0	0.0%	2.6	0.7%	3.0	0.0%
17	3.0	0.0%	3.0	0.0%	0.7	0.0%
18	3.0	0.0%	2.4	0.0%	3.0	0.0%
19	2.3	0.0%	2.3	0.0%	2.5	0.2%
20	3.0	0.0%	0.1	0.0%	1.0	0.0%
21	3.0	0.0%	0.8	0.0%	1.1	0.0%
22	1.1	0.0%	1.5	0.0%	0.8	0.0%
23	3.0	0.0%	1.5	0.0%	0.1	0.0%
24	3.0	0.0%	3.0	0.0%	0.6	0.0%
25	3.0	0.0%	2.2	0.0%	3.0	0.0%
26	3.0	0.0%	3.0	0.0%	3.0	0.0%
27	3.0	0.0%	1.4	0.0%	3.0	0.0%
28	3.0	0.0%	3.0	0.0%	3.0	0.0%
29	3.0	0.0%	3.0	0.0%	3.0	0.0%
30	3.0	0.0%	3.0	0.0%	3.0	0.0%
31	3.0	0.0%	0.4	0.0%	0.6	0.0%
32	3.0	0.0%	3.0	0.0%	3.0	0.0%
33	3.0	0.0%	0.4	0.0%	3.0	0.0%
34	3.0	0.0%	3.0	0.0%	2.5	0.0%
35	3.0	0.0%	0.9	0.0%	-0.9	0.0%
36	3.0	0.0%	3.0	0.0%	1.0	0.0%
37	3.0	0.0%	3.0	0.0%	3.0	0.0%
38	3.0	0.0%	3.0	0.0%	0.8	0.0%
39	3.0	0.0%	3.0	0.0%	3.0	0.0%
40	3.0	0.0%	3.0	0.0%	3.0	0.0%
41	3.0	0.0%	1.4	0.0%	2.4	0.0%
42	3.0	0.0%	3.0	0.0%	2.9	0.0%
43	2.5	0.8%	3.0	0.0%	0.6	0.0%
44	3.0	0.0%	3.0	0.0%	1.4	0.0%
45	3.0	0.0%	3.0	0.0%	2.5	0.0%
46	3.0	0.0%	3.0	0.0%	0.9	0.0%
47	3.0	0.0%	3.0	0.0%	0.7	0.0%
48	3.0	0.0%	3.0	0.0%	1.0	0.0%
49	1.5	0.0%	3.0	0.0%	0.9	0.0%
50	3.0	0.0%	3.0	0.0%	3.0	0.0%

Table E.4 (cont.)

51	3.0	0.0%	-0.2	0.0%	0.5	0.0%
52	3.0	0.0%	2.2	0.0%	2.5	0.3%
53	3.0	0.0%	0.2	0.0%	1.2	0.0%
54	3.0	0.0%	2.8	0.0%	1.2	0.0%
55	2.0	0.0%	0.7	0.0%	0.2	0.0%
56	3.0	0.0%	3.0	0.0%	0.4	0.0%
57	3.0	0.0%	3.0	0.0%	1.1	0.0%
58	3.0	0.0%	3.0	0.0%	2.9	0.0%
59	3.0	0.0%	2.1	0.0%	3.0	0.0%
60	3.0	0.0%	1.2	0.0%	2.4	0.0%
61	3.0	0.0%	1.3	0.0%	0.6	0.0%
62	3.0	0.0%	3.0	0.0%	0.8	0.0%
63	3.0	0.0%	0.3	0.0%	2.4	0.0%
64	3.0	0.0%	3.0	0.0%	0.5	0.0%
65	3.0	0.0%	3.0	0.0%	3.0	0.0%
66	3.0	0.0%	0.0	0.0%	1.2	0.0%
67	3.0	0.0%	0.8	0.0%	0.4	0.0%
68	3.0	0.0%	3.0	0.0%	1.8	0.0%
69	3.0	0.0%	3.0	0.0%	2.2	0.0%
70	3.0	0.0%	3.0	0.0%	2.5	0.0%
71	3.0	0.0%	3.0	0.0%	0.3	0.0%
72	2.3	0.0%	2.3	0.0%	-0.2	0.0%
73	3.0	0.0%	0.5	0.0%	3.0	0.0%
74	3.0	0.0%	3.0	0.0%	1.5	0.0%
75	3.0	0.0%	3.0	0.0%	0.0	0.0%
76	3.0	0.0%	3.0	0.0%	0.2	0.0%
77	3.0	0.0%	3.0	0.0%	-0.3	0.0%
78	3.0	0.0%	3.0	0.0%	1.6	0.0%
79	2.1	0.0%	1.3	0.0%	3.0	0.0%
80	3.0	0.0%	3.0	0.0%	3.0	0.0%
81	3.0	0.0%	3.0	0.0%	3.0	0.0%
82	3.0	0.0%	3.0	0.0%	3.0	0.0%
83	3.0	0.0%	1.5	0.0%	-0.1	0.0%
84	2.3	0.0%	2.6	0.4%	3.0	0.0%
85	3.0	0.0%	3.0	0.0%	2.1	0.0%
86	3.0	0.0%	3.0	0.0%	3.0	0.0%
87	3.0	0.0%	3.0	0.0%	-0.6	0.0%
88	3.0	0.0%	3.0	0.0%	-0.4	0.0%
89	3.0	0.0%	3.0	0.0%	1.8	0.0%
90	3.0	0.0%	0.7	0.0%	-0.8	0.0%
91	1.1	0.0%	1.1	0.0%	0.5	0.0%

Table E.4 (cont.)

92	1.5	0.0%	1.9	0.0%	2.7	0.7%
93	3.0	0.0%	1.4	0.0%	3.0	0.0%
94	1.7	0.0%	1.6	0.0%	-0.1	0.0%
95	3.0	0.0%	3.0	0.0%	3.0	0.0%
96	3.0	0.0%	3.0	0.0%	3.0	0.0%
97	3.0	0.0%	3.0	0.0%	2.3	0.0%
98	3.0	0.0%	2.0	0.0%	2.5	0.1%
99	3.0	0.0%	3.0	0.0%	2.4	0.0%
100	0.6	0.0%	2.5	0.0%	0.9	0.0%
101	3.0	0.0%	3.0	0.0%	3.0	0.0%
102	3.0	0.0%	3.0	0.0%	0.8	0.0%
103	2.3	0.0%	1.5	0.0%	2.4	0.0%
104	3.0	0.0%	3.0	0.0%	1.7	0.0%
105	1.0	0.0%	1.4	0.0%	1.4	0.0%
106	3.0	0.0%	2.5	0.0%	1.4	0.0%
107	3.0	0.0%	0.3	0.0%	0.8	0.0%
108	2.6	2.6%	0.9	0.0%	0.7	0.0%
109	3.0	0.0%	-0.2	0.0%	3.0	0.0%
110	3.0	0.0%	1.3	0.0%	0.7	0.0%
111	3.0	0.0%	3.0	0.0%	3.0	0.0%
112	3.0	0.0%	2.5	1.6%	2.2	0.0%
113	3.0	0.0%	3.0	0.0%	2.4	0.0%
114	3.0	0.0%	2.4	0.0%	0.9	0.0%
115	3.0	0.0%	2.5	1.7%	3.0	0.0%
116	1.5	0.0%	1.8	0.0%	1.1	0.0%
117	0.5	0.0%	-0.4	0.0%	-0.2	0.0%
118	3.0	0.0%	3.0	0.0%	2.4	0.0%
119	3.0	0.0%	-0.3	0.0%	2.7	0.1%
120	3.0	0.0%	0.7	0.0%	3.0	0.0%
121	3.0	0.0%	-0.3	0.0%	0.4	0.0%
122	3.0	0.0%	-0.5	0.0%	0.1	0.0%
123	3.0	0.0%	-0.3	0.0%	3.0	0.0%
124	3.0	0.0%	2.4	0.0%	1.2	0.0%
125	3.0	0.0%	0.0	0.0%	3.0	0.0%
126	3.0	0.0%	1.6	0.0%	3.0	0.0%
127	3.0	0.0%	0.5	0.0%	0.2	0.0%
128	3.0	0.0%	2.9	0.0%	3.0	0.0%
129	3.0	0.0%	-0.6	0.0%	2.1	0.0%
130	3.0	0.0%	0.5	0.0%	3.0	0.0%
131	3.0	0.0%	-0.1	0.0%	3.0	0.0%
132	3.0	0.0%	-0.6	0.0%	1.5	0.0%

Table E.4 (cont.)

133	3.0	0.0%	1.2	0.0%	3.0	0.0%
134	3.0	0.0%	1.4	0.0%	3.0	0.0%
135	3.0	0.0%	-0.4	0.0%	0.0	0.0%
136	2.4	0.0%	0.8	0.0%	0.8	0.0%
137	0.6	0.0%	-0.7	0.0%	0.4	0.0%
138	3.0	0.0%	-0.6	0.0%	3.0	0.0%
139	3.0	0.0%	0.9	0.0%	0.9	0.0%
140	3.0	0.0%	-0.3	0.0%	-0.5	0.0%
141	3.0	0.0%	-0.3	0.0%	3.0	0.0%
142	3.0	0.0%	0.3	0.0%	3.0	0.0%
143	3.0	0.0%	0.4	0.0%	2.4	0.0%
144	3.0	0.0%	2.5	0.0%	1.7	0.0%
145	3.0	0.0%	0.8	0.0%	0.7	0.0%
146	3.0	0.0%	0.5	0.0%	1.6	0.0%
147	3.0	0.0%	-0.6	0.0%	1.9	0.0%
148	0.6	0.0%	-0.8	0.0%	3.0	0.0%
149	3.0	0.0%	0.6	0.0%	2.4	0.0%
150	3.0	0.0%	1.9	0.0%	3.0	0.0%
151	3.0	0.0%	2.2	0.0%	1.7	0.0%
152	3.0	0.0%	1.5	0.0%	3.0	0.0%
153	3.0	0.0%	-0.7	0.0%	0.4	0.0%
154	3.0	0.0%	1.4	0.0%	3.0	0.0%
155	3.0	0.0%	-0.7	0.0%	3.0	0.0%
156	0.6	0.0%	-0.7	0.0%	3.0	0.0%
157	3.0	0.0%	-0.9	0.0%	0.1	0.0%
158	3.0	0.0%	1.3	0.0%	3.0	0.0%
159	3.0	0.0%	0.4	0.0%	3.0	0.0%
160	3.0	0.0%	-0.4	0.0%	2.9	0.0%
161	3.0	0.0%	-0.2	0.0%	3.0	0.0%
162	3.0	0.0%	-0.2	0.0%	0.8	0.0%
163	3.0	0.0%	-0.5	0.0%	2.2	0.0%
164	0.5	0.0%	-0.9	0.0%	0.5	0.0%
165	3.0	0.0%	1.6	0.0%	1.6	0.0%
166	2.7	0.0%	-0.3	0.0%	-0.8	0.0%
167	3.0	0.0%	2.1	0.0%	3.0	0.0%
168	3.0	0.0%	-0.1	0.0%	0.1	0.0%
169	0.5	0.0%	-0.5	0.0%	-1.0	0.0%
170	3.0	0.0%	2.2	0.0%	1.4	0.0%
171	3.0	0.0%	-0.5	0.0%	0.6	0.0%
172	3.0	0.0%	-0.6	0.0%	2.7	0.1%
173	3.0	0.0%	1.7	0.0%	3.0	0.0%

Table E.4 (cont.)

174	3.0	0.0%	0.2	0.0%	3.0	0.0%
175	3.0	0.0%	3.0	0.0%	3.0	0.0%
176	3.0	0.0%	3.0	0.0%	3.0	0.0%
177	1.9	0.0%	3.0	0.0%	3.0	0.0%
178	1.9	0.0%	3.0	0.0%	3.0	0.0%
179	3.0	0.0%	3.0	0.0%	3.0	0.0%
180	3.0	0.0%	3.0	0.0%	3.0	0.0%
181	3.0	0.0%	3.0	0.0%	3.0	0.0%
182	3.0	0.0%	3.0	0.0%	3.0	0.0%
183	-0.2	0.0%	3.0	0.0%	3.0	0.0%

Table E.5 - Particle Injection Data for Simulation Experiments 13, 14, and 15

	Simulation Experiment 13		Simulation Experiment 14		Simulation Experiment 15	
Particle Number	Penetration Depth [um]	% Loss in Flux [-]	Penetration Depth [um]	% Loss in Flux [-]	Penetration Depth [um]	% Loss in Flux [-]
1	3.0	0.0%	1.6	0.0%	3.0	0.0%
2	2.6	1.0%	1.6	0.0%	3.0	0.0%
3	0.5	0.0%	0.7	0.0%	0.3	0.0%
4	1.4	0.0%	2.9	0.0%	0.4	0.0%
5	0.4	0.0%	0.4	0.0%	0.3	0.0%
6	2.8	0.0%	2.8	0.0%	1.7	0.0%
7	3.0	0.0%	3.0	0.0%	2.4	0.0%
8	0.3	0.0%	-0.2	0.0%	0.1	0.0%
9	1.0	0.0%	0.8	0.0%	0.1	0.0%
10	1.2	0.0%	2.7	0.2%	1.5	0.0%
11	3.0	0.0%	3.0	0.0%	2.9	0.0%
12	2.8	0.0%	2.6	0.4%	2.7	0.0%
13	3.0	0.0%	3.0	0.0%	3.0	0.0%
14	2.7	0.0%	2.9	0.0%	2.9	0.0%
15	3.0	0.0%	-0.9	0.0%	3.0	0.0%
16	1.4	0.0%	1.6	0.0%	2.6	0.6%
17	2.6	0.2%	0.3	0.0%	0.7	0.0%
18	2.3	0.0%	3.0	0.0%	2.1	0.0%
19	3.0	0.0%	3.0	0.0%	2.6	1.0%
20	0.8	0.0%	0.9	0.0%	0.7	0.0%
21	0.7	0.0%	2.5	0.0%	2.9	0.0%
22	2.5	0.0%	0.7	0.0%	0.3	0.0%

Table E.5 (cont.)

23	-0.6	0.0%	-0.9	0.0%	0.1	0.0%
24	0.5	0.0%	0.5	0.0%	3.0	0.0%
25	2.6	0.8%	2.6	0.4%	2.1	0.0%
26	3.0	0.0%	3.0	0.0%	3.0	0.0%
27	2.8	0.0%	2.6	0.4%	3.0	0.0%
28	3.0	0.0%	2.4	0.0%	2.6	0.4%
29	3.0	0.0%	2.9	0.0%	3.0	0.0%
30	2.2	0.0%	3.0	0.0%	2.5	0.0%
31	3.0	0.0%	2.7	0.0%	2.8	0.0%
32	2.6	1.2%	3.0	0.0%	2.7	0.1%
33	2.7	0.0%	0.2	0.0%	0.9	0.0%
34	3.0	0.0%	3.0	0.0%	2.3	0.0%
35	-1.0	0.0%	-0.5	0.0%	-0.1	0.0%
36	2.3	0.0%	2.1	0.0%	2.9	0.0%
37	3.0	0.0%	3.0	0.0%	2.4	0.0%
38	0.7	0.0%	0.7	0.0%	0.5	0.0%
39	3.0	0.0%	1.6	0.0%	0.3	0.0%
40	3.0	0.0%	3.0	0.0%	3.0	0.0%
41	1.0	0.0%	3.0	0.0%	0.6	0.0%
42	2.9	0.0%	2.5	0.1%	1.9	0.0%
43	0.3	0.0%	0.3	0.0%	0.3	0.0%
44	1.4	0.0%	2.0	0.0%	1.4	0.0%
45	2.7	0.5%	1.6	0.0%	3.0	0.0%
46	1.0	0.0%	1.1	0.0%	1.1	0.0%
47	0.7	0.0%	0.6	0.0%	0.9	0.0%
48	0.9	0.0%	1.1	0.0%	1.1	0.0%
49	0.7	0.0%	0.9	0.0%	1.3	0.0%
50	3.0	0.0%	3.0	0.0%	3.0	0.0%
51	3.0	0.0%	3.0	0.0%	3.0	0.0%
52	2.5	0.0%	2.6	0.8%	2.1	0.0%
53	0.7	0.0%	0.1	0.0%	2.8	0.0%
54	0.0	0.0%	0.4	0.0%	0.2	0.0%
55	3.0	0.0%	0.5	0.0%	-0.2	0.0%
56	0.2	0.0%	0.0	0.0%	0.5	0.0%
57	-0.5	0.0%	3.0	0.0%	1.1	0.0%
58	1.7	0.0%	3.0	0.0%	2.5	0.0%
59	2.5	0.0%	2.6	0.7%	2.6	0.3%
60	0.0	0.0%	0.5	0.0%	3.0	0.0%
61	0.5	0.0%	0.4	0.0%	3.0	0.0%
62	3.0	0.0%	3.0	0.0%	0.7	0.0%
63	-0.1	0.0%	0.1	0.0%	-0.2	0.0%

Table E.5 (cont.)

64	0.4	0.0%	0.5	0.0%	0.3	0.0%
65	1.6	0.0%	3.0	0.0%	2.7	0.0%
66	2.9	0.0%	1.0	0.0%	1.2	0.0%
67	0.3	0.0%	0.1	0.0%	0.2	0.0%
68	3.0	0.0%	3.0	0.0%	3.0	0.0%
69	2.4	0.0%	2.4	0.0%	2.2	0.0%
70	3.0	0.0%	1.9	0.0%	3.0	0.0%
71	0.4	0.0%	0.6	0.0%	0.6	0.0%
72	-0.9	0.0%	0.2	0.0%	0.2	0.0%
73	-0.7	0.0%	-0.5	0.0%	-1.0	0.0%
74	1.2	0.0%	1.9	0.0%	2.2	0.0%
75	0.3	0.0%	0.5	0.0%	-0.2	0.0%
76	3.0	0.0%	3.0	0.0%	-0.4	0.0%
77	2.6	0.3%	1.0	0.0%	0.9	0.0%
78	1.5	0.0%	3.0	0.0%	3.0	0.0%
79	1.1	0.0%	3.0	0.0%	3.0	0.0%
80	3.0	0.0%	3.0	0.0%	3.0	0.0%
81	3.0	0.0%	3.0	0.0%	3.0	0.0%
82	1.7	0.0%	3.0	0.0%	3.0	0.0%
83	0.3	0.0%	-0.1	0.0%	-0.1	0.0%
84	2.9	0.0%	2.4	0.0%	3.0	0.0%
85	3.0	0.0%	1.2	0.0%	3.0	0.0%
86	3.0	0.0%	3.0	0.0%	3.0	0.0%
87	0.5	0.0%	0.0	0.0%	2.3	0.0%
88	-0.3	0.0%	0.0	0.0%	0.0	0.0%
89	2.8	0.0%	1.9	0.0%	2.6	2.2%
90	-0.3	0.0%	3.0	0.0%	3.0	0.0%
91	-0.1	0.0%	0.3	0.0%	0.2	0.0%
92	2.3	0.0%	2.3	0.0%	2.2	0.0%
93	3.0	0.0%	3.0	0.0%	2.6	0.9%
94	1.4	0.0%	0.4	0.0%	0.2	0.0%
95	3.0	0.0%	2.5	0.0%	3.0	0.0%
96	2.8	0.0%	2.5	0.0%	3.0	0.0%
97	2.3	0.0%	2.9	0.0%	3.0	0.0%
98	2.5	0.0%	3.0	0.0%	3.0	0.0%
99	3.0	0.0%	3.0	0.0%	3.0	0.0%
100	0.0	0.0%	2.5	1.5%	0.2	0.0%
101	3.0	0.0%	1.1	0.0%	2.2	0.0%
102	2.1	0.0%	2.3	0.0%	0.0	0.0%
103	1.3	0.0%	2.2	0.0%	2.3	0.0%
104	1.5	0.0%	3.0	0.0%	1.1	0.0%

Table E.5 (cont.)

105	1.2	0.0%	1.1	0.0%	1.3	0.0%
106	2.6	1.0%	1.9	0.0%	1.9	0.0%
107	3.0	0.0%	0.0	0.0%	2.2	0.0%
108	0.2	0.0%	-0.1	0.0%	-0.1	0.0%
109	1.7	0.0%	3.0	0.0%	3.0	0.0%
110	0.7	0.0%	0.3	0.0%	0.1	0.0%
111	3.0	0.0%	3.0	0.0%	3.0	0.0%
112	1.7	0.0%	1.6	0.0%	2.4	0.0%
113	3.0	0.0%	3.0	0.0%	2.3	0.0%
114	0.9	0.0%	3.0	0.0%	0.7	0.0%
115	1.4	0.0%	0.8	0.0%	-0.1	0.0%
116	-0.3	0.0%	0.4	0.0%	0.2	0.0%
117	2.5	0.1%	0.1	0.0%	-0.4	0.0%
118	3.0	0.0%	2.4	0.0%	3.0	0.0%
119	3.0	0.0%	2.6	0.7%	3.0	0.0%
120	1.4	0.0%	1.0	0.0%	3.0	0.0%
121	1.3	0.0%	0.1	0.0%	0.4	0.0%
122	0.4	0.0%	-0.1	0.0%	0.3	0.0%
123	3.0	0.0%	3.0	0.0%	0.8	0.0%
124	2.4	0.0%	2.7	0.0%	2.3	0.0%
125	1.4	0.0%	0.4	0.0%	0.4	0.0%
126	1.6	0.0%	3.0	0.0%	3.0	0.0%
127	-0.1	0.0%	0.0	0.0%	0.1	0.0%
128	1.6	0.0%	2.1	0.0%	2.2	0.0%
129	1.8	0.0%	0.3	0.0%	3.0	0.0%
130	3.0	0.0%	1.5	0.0%	0.7	0.0%
131	2.7	0.0%	0.9	0.0%	0.3	0.0%
132	3.0	0.0%	3.0	0.0%	2.5	0.2%
133	1.7	0.0%	1.7	0.0%	3.0	0.0%
134	1.5	0.0%	2.3	0.0%	2.0	0.0%
135	0.0	0.0%	0.2	0.0%	-0.1	0.0%
136	1.5	0.0%	3.0	0.0%	2.6	0.5%
137	0.7	0.0%	0.9	0.0%	0.4	0.0%
138	2.1	0.0%	3.0	0.0%	3.0	0.0%
139	3.0	0.0%	3.0	0.0%	1.5	0.0%
140	0.8	0.0%	-0.3	0.0%	0.0	0.0%
141	3.0	0.0%	1.0	0.0%	3.0	0.0%
142	0.6	0.0%	2.8	0.0%	0.2	0.0%
143	1.3	0.0%	2.5	0.0%	2.4	0.0%
144	1.4	0.0%	1.7	0.0%	2.0	0.0%
145	1.4	0.0%	1.1	0.0%	0.9	0.0%

Table E.5 (cont.)

146	3.0	0.0%	3.0	0.0%	0.6	0.0%
147	0.7	0.0%	0.5	0.0%	0.3	0.0%
148	0.4	0.0%	1.1	0.0%	1.0	0.0%
149	1.9	0.0%	3.0	0.0%	2.4	0.0%
150	3.0	0.0%	3.0	0.0%	2.3	0.0%
151	1.7	0.0%	1.7	0.0%	3.0	0.0%
152	2.3	0.0%	2.3	0.0%	3.0	0.0%
153	0.6	0.0%	0.6	0.0%	0.5	0.0%
154	2.7	0.0%	3.0	0.0%	2.3	0.0%
155	3.0	0.0%	-0.1	0.0%	2.7	0.0%
156	-0.1	0.0%	1.1	0.0%	0.2	0.0%
157	3.0	0.0%	0.6	0.0%	3.0	0.0%
158	3.0	0.0%	3.0	0.0%	1.0	0.0%
159	0.9	0.0%	3.0	0.0%	3.0	0.0%
160	3.0	0.0%	3.0	0.0%	3.0	0.0%
161	3.0	0.0%	0.4	0.0%	3.0	0.0%
162	3.0	0.0%	3.0	0.0%	3.0	0.0%
163	1.4	0.0%	2.6	2.3%	3.0	0.0%
164	0.3	0.0%	0.3	0.0%	3.0	0.0%
165	2.1	0.0%	3.0	0.0%	3.0	0.0%
166	-0.1	0.0%	-0.1	0.0%	3.0	0.0%
167	1.4	0.0%	3.0	0.0%	3.0	0.0%
168	0.0	0.0%	-0.1	0.0%	3.0	0.0%
169	-0.1	0.0%	-0.8	0.0%	3.0	0.0%
170	1.0	0.0%	1.7	0.0%	3.0	0.0%
171	0.8	0.0%	1.7	0.0%	3.0	0.0%
172	3.0	0.0%	1.4	0.0%	3.0	0.0%
173	1.7	0.0%	3.0	0.0%	3.0	0.0%
174	1.0	0.0%	0.6	0.0%	3.0	0.0%
175	3.0	0.0%	2.4	0.0%	3.0	0.0%
176	3.0	0.0%	1.6	0.0%	3.0	0.0%
177	3.0	0.0%	1.2	0.0%	3.0	0.0%
178	3.0	0.0%	-0.1	0.0%	3.0	0.0%
179	3.0	0.0%	2.4	0.0%	3.0	0.0%
180	3.0	0.0%	1.4	0.0%	3.0	0.0%
181	3.0	0.0%	1.0	0.0%	3.0	0.0%
182	3.0	0.0%	1.2	0.0%	3.0	0.0%
183	3.0	0.0%	-0.1	0.0%	3.0	0.0%

Author's Biography

Bingyi Yu was born 1986 in Tianjin, China. His family came to the United States, settled in Detroit, Michigan, and now permanently resides in Rochester, Minnesota, where Bingyi graduated with honors from Mayo High School. He finished his Bachelor of Science in Mechanical Engineering from the University of Wisconsin-Madison in 2008 and then advised commercial and industrial facilities for energy efficiency at a Midwest consulting firm in La Crosse, Wisconsin.

He matriculated Fall 2009 at the University of Illinois at Urbana-Champaign to obtain his Master of Science in Mechanical Engineering under the research guidance of Professor Shiv Kapoor and Professor Richard DeVor in the topic of sustainability engineering. His graduate work involved enhancing a three-dimensional computational fluid dynamic model of a microfilter and creating a knowledge base of efficacy and sustainability improvements for the microfiltration of semi-synthetic metalworking fluids. This work brought forth two conferences papers, two conference presentations, a poster session, and two journal papers.

Bingyi will be furthering his education with an MBA at the Tepper School of Business at Carnegie Mellon. He intends to utilize his two Masters degrees to develop strategies in domestic and Sino-US business development for energy and sustainability technologies.